Crustal thickness beneath Mt. Merapi and Mt. Merbabu, Central Java, Indonesia, inferred from receiver function analysis.

S. K. Suhardja[1], S. Widiyantoro[2,3], J.-P. Métaxian[4], N. Rawlinson[5], M. Ramdhan[6] and Agus Budi-Santoso[7]

[1]University of Pertamina, Jl. Teuku Nyak Arief, Simprug, Kebayoran Lama, Jakarta 12220, Indonesia

[2]Global Geophysics Research Group, Faculty of Mining and Petroleum Engineering Institute of Technology Bandung, Jalan Ganesa No. 10, Bandung 40132, Indonesia

[3]Research Center for Disaster Mitigation, Institute of Technology Bandung, Jalan Ganesa No. 10, Bandung 40132, Indonesia

[4]ISTerre, IRD R219, CNRS, Université de Savoie Mont Blanc, Le Bourget-du-Lac, France

[5]Department of Earth Sciences – Bullard Labs, University of Cambridge, Cambridge CB30EZ, United Kingdom

[6]Agency for Meteorology, Climatology and Geophysics, Jalan Angkasa I, No. 2, Kemayoran, Jakarta, Indonesia

[7]Center for Volcanology and Geological Hazard Mitigation, Geological Agency, Jalan Diponegoro No. 57, Bandung, 40122, Indonesia

SUMMARY

In this study, we analysed 2708 receiver functions (RFs) using data recorded by 53 seismographic stations that surround- Mt. Merapi and Mt. Merbabu – two volcanos in Central Java - to map the boundary between Earth's crust and upper mantle. We observe that a number of RFs from this new dataset have complex signals and do not exhibit typical RF characteristics; in particular, where the converted Ps signal from the Moho discontinuity is the clearest and strongest amplitude arrival following the P onset. This effect may be related to complex shallow velocity structure due to the presence of magmatic rocks and sediments. Further analysis of the RF results using the H-κ method suggests that Moho depth varies between 27 to 32 km beneath the array, with no apparent correlation between crustal thickness and surface topography, as one might expect from Airy isostacy. For instance, the Moho is quite shallow beneath Mt. Merapi (up to 27 km depth), despite its elevation of nearly 3 km. This may be a consequence of dynamic support from an active upper mantle coupled with erosion and/or weakening of the lower crust due to the active volcanic plumbing system. To the north of Mt. Merapi, the Moho is deeper (30-31 km depth) below Mt. Merbabu. Vp/Vs ratio estimates from the H-κ method are relatively high (~1.9) beneath the Mt. Merapi and Kendeng Basin area, which may indicate the presence of a zone of hydrous and active partial melting in the underlying crust. Lower Vp/Vs ratios (~1.7) are found beneath Mt. Merbabu, which may be due to its relative lack of volcanic activity compared to Mt. Merapi.

Key words: Receiver Function, Mt. Merapi, Crustal Thickness, Indonesia

INTRODUCTION

The island of Java is located at the southwestern edge of the Eurasian continent where the Australian plate subducts beneath Sundaland. The tectonic setting of this area is dominated by the Sunda Arc, which gives rise to frequent megathrust earthquakes and a large number of active volcanoes. At present, the convergence rate between Australia and Indonesia is 67 mm per year (Simons *et al.* 2007) and the dip angle of the slab increases from near-horizontal inboard of the trench to very steep (70^{o}-80^{o}) from a depth of 50 km to the north of Java (Koulakov *et al*. 2007). We estimate, based on the distribution of earthquakes in global catalogues (Weston *et al.* 2019), that the depth of the slab beneath our study area is at about

100-120 km. Muller *et al.* (1997) estimated the age of the subducted plate beneath central Java to be about 80-100 Ma.

The arc magmatism and volcanic activity that characterises central Java are largely dictated by the subduction setting. Overall there are two main volcanic arcs, the Southern Mountain Arc (SMA) and Modern Volcanic Arc (MVA). Smyth *et al.* (2008) proposed that from the middle Eocene (about 45 to 20 Ma), a volcanic arc formed in the southern coastal region of the Island, which became what is now known as SMA. Clements *et al.* (2009) postulated that subduction in this area ceased in the Cretaceous but then resumed in the late Miocene and created the MVA, which is located about 50 km north of SMA. To the north of the MVA, a large basin was formed on the edge of Sundaland and is named the Kendeng zone (Fig. 1). The Merapi and Merbabu volcanoes, which are part of the MVA, are the focus of this study.

Mt. Merapi is one of the most active volcanos in the world, with an eruption frequency of between two to six years (Ratdomopurbo & Poupinet 2000). Eruptions from this volcano are dominated by pyroclastic flows caused by lava dome collapse (Hidayati *et al.* 2008). Surono *et al.* (2012) determined that a different eruption type, which is more explosive and of higher magnitude like the 2010 eruption, occurs less frequently at 50-100 year intervals.

Camus *et al.* (2000) estimated that volcanism began at Mt. Merapi about 40,000 years ago. The available radiocarbon data indicate almost continuous volcanic activity at Merapi during the last 2000 years, during which it only experienced two periods of decreased activity between 600–700 and 1200–1300 years B.P. (Gertisser & Keller 2003). Ratdomopurbo & Poupinet (2000) studied seismicity in the vicinity of Merapi volcano and discovered an aseismic zone within the cone of the volcano. They suggested that two magma reservoirs may be present: A shallow reservoir at 1–2 km depth below the summit which may have a high-hazard potential; and a larger and deeper one, most likely the main reservoir located below 5 km depth. Beauducel & Cornet (1999) used GPS and tilt data to conclude that the main magma reservoir is located between 6 km and 9 km below the summit. More recently, high-resolution gravity models show evidence of high-density bodies beneath the volcanic summits of Merapi, Merbabu and Telemoyo, which can be interpreted as magma reservoirs (Tiede *et al.* 2005).

A study by Widiyantoro *et al.* (2018) using local earthquake tomography with data from the same network used in this study found three active areas with high Vp/Vs: the first is a shallow zone interpreted to represent a region of intense fluid percolation, directly below the summit of the volcano; the second is thought to be a pre-eruptive magma reservoir at 10 to 20 km depth below MSL that is several orders of magnitude larger than known erupted magma volumes; and the third is a deep magma reservoir at 30 km depth which supplies the main reservoir.

To date, there have been numerous geophysical studies that have undertaken seismic velocity imaging in Central Java, including Mt. Merapi. Local earthquake tomography models (Koulakov et al. 2007) exhibit high Vp/Vs ratios inside the Merapi Lawu Anomaly (MLA) region, located to the north of Mt. Merapi, that may be related to the presence of elevated fluids and partial melts. Wagner *et al.* (2007) also applied local earthquake tomography in this region and found a very pronounced low velocity anomaly in the back-arc crust north of the active volcano. They also found a low velocity anomaly in the upper mantle which they interpret as the pathway of fluids and partially molten material.

Bohm *et al.* (2013) employed seismic attenuation tomography in central Java and discovered a prominent zone of increased attenuation directly beneath and north of the modern volcanic arc at depths down to 15 km. Their model also showed increased attenuation outside the Kendeng Basin just beneath Mt. Merapi that goes down to a depth of 35 km with a southward dip. Elevated temperatures with possible partial melts and a magma chamber beneath the Merapi volcano were proposed as part of the interpretation.

Zulfakriza *et al.* (2014) carried out seismic ambient noise tomography using the MERAMEX~~eramex~~ data set in central Java and found a band of low velocities centred between Mt Merapi and Mt Lawu that are located in the mid-crust at ~15 km depth and also concentrated in the upper 5 km of the crust. However, they found it difficult to interpret whether the low velocity zones relate to the presence of fluids and partial melt or sediments which fill the Kendeng zone.

The work that is most relevant to this study are the crustal imaging results from the MERAMEX network by Wölbern (2016). By extracting receiver functions, similar to what is done in this study, they encountered a high degree of waveform complexity and reported an average crustal thickness of 34 km in central Java. Moreover, a shallower Moho at 30 km depth is seen beneath the Kendeng zone, which reflects the presence of ophiolitic basement in the center of the island related to the Meratus suture zone. A deeper Moho at 39 km depth is also seen to the north and west of the Kendeng zone, and is thought to be present due to crustal thickening by overthrusting and compressional deformation from a previous collision zone. Note that although part of the MERAMEX network spanned our study area, the DOMERAPI network has a much denser station coverage.

DATA AND METHOD

Illumination of lithospheric structure using seismic methods can provide important information for understanding regional tectonics; for example, if we can determine crustal thickness in a zone of extension, then we can place constraints on the amount of extension that has occurred. Crustal imaging can also provide insight into mantle properties by comparing predicted and observed topography for a known crustal thickness. In the case of

P-wave receiver functions, when a teleseismic P wave encounters a boundary, mode conversion to SV waves will occur, which will be recorded on the radial component of the seismogram. These mode conversions can be exploited to determine the depth of interfaces and the S-wave velocity of layers. When there is a velocity increase with depth across a boundary, a positive RF pulse is produced, whereas a negative pulse is produced by a decrease in S velocity with depth across a boundary. The vertical and radial components of the early part of a teleseismic waveform (prior to direct S arrivals) are a function of the source time function and P-wave arrivals; however, P-SV conversions should primarily appear on the radial component. To isolate such signal, the RF is calculated by removing or deconvolving the recorded vertical component on a seismogram from the radial component. Typical RF responses show a strong pulse at the P wave arrival, with the next strongest pulse likely being the Moho signal followed by its reverberations or multiples. Further details on the computation of RFs can be found in Langston (1977), Owen *et al.* (1984) and Suhardja *et al.* (2013).

Data

In this study we use data recorded by the DOMERAPI temporary seismic network installed in the neighbourhood of Merapi volcano. A total 53 broad-band seismometers, most of them Guralp CMG-40Ts, were installed from October 2013 to mid-April 2015, with an average inter-station distance of ~4 km. This has provided by far the densest coverage of seismograph stations ever used on Merapi (Fig. 2). The goal of the seismic experiment was to image the subsurface beneath Merapi in order to illuminate the deep magma source and associated magmatic processes. This study is a collaborative effort between Universitas Pertamina, Institut Teknologi Bandung, Institut de Recherche pour le Développement (IRD), France, and the Agency for Meteorology, Climatology and Geophysics (BMKG).

The first step in RF data processing is to obtain an event catalog from the International Seismological Centre (ISC) for earthquakes that occurred during the station deployment. For this study, we obtain more than 150 earthquakes with magnitude > 5.5 and epicentral distances between 30 to 100 degrees. The locations of the hypocenters and stations are shown in Fig. 3. Most of the good quality data come from events in Japan, Papua New Guinea and New Zealand. Next, we cut the waveforms at 20 s before and 60 s after the direct P arrival to ensure that all converted phases to a depth of 100 km are included. After that, using calculated back-azimuth information, horizontal component data were then rotated to radial and tangential components, where the radial direction is parallel to the great circle from the event to the station. Next, the vertical and radial components are rotated into P-SV components using incidence angle information estimated from the ak135 velocity model (Kennett *et al.* 1995). A rotation into P-SV components will theoretically increase the amplitude of the Ps wave on the SV component. However, this depends on how accurately we know the angle of incidence which in turn depends on how well we know the near surface velocities. This procedure should also minimize the direct P wave amplitude on the SV component, although in practice, we still see strong amplitudes on the P onset.

To improve the quality of the waveform, a signal-to-noise ratio check was carried out by comparing the power in the seismic traces 20s before and after the predicted arrival time of the P wave. We only used seismograms with signal-to-noise ratios higher than two for both the P and SV components to ensure that only high-quality data are used in the deconvolution. Although we initially collected seismograms with high magnitude events, some seismograms don't show high quality data and the signal-to-noise ratio criteria removed 30–40% of all seismograms we initially considered. For example, at station ME29, from 150 events collected, 48 were removed due to high noise levels. An incoming P wave can have a very complicated shape due to the source time function, near surface reverberations at the source, multipathing along the propagation path as well as P wave multiples near the receiver. Each Ps converted wave should also have the same shape as the incoming P wave. Thus, to isolate the Ps waves and convert them to simple pulses, the P component is deconvolved from the SV component. We performed the deconvolution process in the frequency domain by using the water-level stabilization method and a low-pass Gaussian filter to remove high-frequency noise (Langston 1977). The RF H(ω) is calculated using the following:

$$H(\omega) = \frac{R(\omega)Z^{*}(\omega)}{\max\{Z(\omega)Z^{*}(\omega), c\max\{Z(\omega)Z^{*}\}\}}G(\omega) \qquad \text{....(eq. 1)}$$

$$G(\omega) = \exp\left(\frac{-\omega^{2}}{4\alpha^{2}}\right)$$

where ω is angular frequency, Z(ω) is the Fourier transform of the P component waveform, R(ω) is the transform of the SV component, and Z*(ω) is the complex conjugate of Z(ω). G(ω) is a Gaussian filter that has zero phase distortion and a lack of sidelobes. The values of α and c were chosen by trial and error, where we tried to make the RF as sharp as possible but also tried to minimize noise. All RFs were computed using a water-level parameter c of 0.001 and a Gaussian smoothing parameter α of 3.5. A final visual check was also performed. Good RFs are identified by having a sharp P wave signal with little energy arriving earlier. Low-quality RFs tend to have anomalously high-amplitude signals at later times or very wide sidelobes. We eliminated these data before further data processing. An example of RFs for station ME29, plotted as a function of ray parameter, is shown in Fig. 4. Note that each RF is stacked into each bin. Most of the RFs have similar signals with a peak at 0 s (the P wave) followed by negative side lobes and several positive signals; the third positive signal (at 3.6 sec) appears to be much stronger, and we interpret it as a conversion from the Moho.

We also performed a stack of all the ME29 RFs in the depth domain. Starting with a 1-D velocity model from seismic tomography (Ramdhan et al. 2019) and horizontal slowness information, each RF can be interpolated into the depth domain to correct for moveout and then stacked. Fig. 5 shows a stacked RF in the depth domain with high amplitude at 0 km followed by a strong positive amplitude at 30 km depth interpreted as an arrival from the Moho. Strong signals are also seen at 12 s and 15 s in the time domain, which are likely PpPs and PsPs/PpSs multiples from the Moho but could also be conversions from deeper mantle discontinuities. As an additional stacking analysis, we also performed Nth-root stacking (Muirhead 1968) with N set to 2; this causes the final stack to have slightly spikier positive signal and suppresses some of the noise especially at later times (Fig. 5).

Station ME29 is located near Mt. Merapi, where a strong negative signal occurs between two positive signals. A detailed forward waveform model or RF inversion may be needed to better understand the cause of this feature. However, these signals might be related to the presence of low velocity layers at shallow and deeper crustal depths associated with magma chambers.

Complex RF signal

Fig. 6 shows a collection of stacked RFs from stations to the north, east, south and west of Mt. Merapi, as well as one station located on the volcano itself. Typically, a stacked Receiver Function would show a strong positive and clear P wave signal, followed by the second strongest positive signal corresponding to a Ps conversion at the Moho. However, some stations show a much more complex pattern with a mix of positive and negative signals shortly after the incoming P wave, as seen on Figure 6. For example, station ME19 to the west and ME43 to the south show a strong positive signal after the P wave onset followed by a negative side lobe and a slightly stronger positive pulse (marked with a star) that we think is the Moho signal. High amplitude signal shortly after the P wave arrival may represent reverberations from boundaries at shallow depths (e.g. sedimentary or volcanic rock layering), which may mask later arriving signal that we may wish to exploit. Another unusual observation is that some stations do not have the Moho conversion as the strongest signal after the P wave arrival. Note that RFs from the MERAMEX study of Wölbern & Rümpker (2016) also feature high levels of waveform complexity, which may be attributed to complexity of local structures. Suhardja *et al.* (2015) performed RFs near the subduction zone in southwestern Mexico and found that the converted wave from the Moho could essentially become undetectable as a result of dehydration process from the down-going slab, and serpentinization reducing the velocity contrast and hence decreasing the amplitude of the converted wave. However, the depth of the slab beneath our study area is estimated to be about 120 km (Koulakov *et al*. 2007), which is deeper than the slab beneath Cascadia and southwestern Mexico (~60-70 km depth). Nevertheless, both slab dehydration and serpentinization of the uppermost mantle and strong shallow velocity anomalies may be responsible for the complex RFs observed in our study area. Further insight into these complexities could be achieved through receiver function inversion, which is the subject of a future study.

Delayed P wave arrival

Typically, the direct P wave, which is shown as the first positive spike in most RFs, arrives at a similar time to ak135 predictions, although lateral heterogeneity in the crust and mantle, and errors in earthquake origin time, contribute to the observed differences. However, we noticed that the P-arrivals at some stations in the northern and eastern part of the study area have a significantly delayed onset observed on the vertical component before deconvolution. For example, station ME01, which is located in the northern part of the study area, has a P onset that arrives almost one second after the predicted time. A similar late arrival can also be observed at station ME 27 in the eastern part of the study area. Previous tomography results

(Koulakov *et al.* 2007; Wagner *et al.* 2007) have found a very low velocity anomaly in this region, with a maximum amplitude of -30% at 5 km depth. This has been interpreted to be the result of thick lava and sedimentary deposits in the Kendeng zone. In addition, tomography studies reveal the presence of a low velocity zone extending all the way to the mantle, yet without any active volcanism in the Kendeng zone. These observations lead them to propose a cooling process which produced a rigid matrix filled with pockets of molten materials.

The delayed teleseismic P wave arrivals we have found are located at the most eastern and northern regions of our study area and are coincident with the location of Kendeng Basin. It is therefore likely that they are also caused by the same phenomena that produced the low velocity zones in the previous studies i.e. sedimentary deposits and recent magmatic intrusions. Teleseismic tomography may be able to provide further insight into these large delay times, which will be the subject of a future study.

H-κ method

Typical RFs exhibit a series of pulses that can be attributed to P to S converted waves from interfaces in the subsurface beneath a seismic station. To convert these pulses to interface depth beneath a station requires knowledge of the P and S velocities above the interface. Zhu & Kanamori (2000) introduced a method (the H-κ method) that can minimize the ambiguity due to the trade-off between depth and velocity in a flat and uniform layer. In most applications, it involves a grid search across a range of crustal thicknesses and Vp/Vs ratios to obtain theoretical arrival times of the Ps converted wave and its multiple. The method will then sum all RFs at the times corresponding to the Ps arrival time as well as the arrival times for the multiples for various choices of layer thickness (H) and Vp/Vs ratio. When the correct depths and velocities are used, the summation amplitude should be large because it would correspond to the superposition of RF peaks associated with the converted direct arrival and its multiples. The summation can be written as:

$$S(H,K) = \sum_{j=1}^{N} w_1 r_j(t_1) + w_2 r_j(t_2) + w_3 r_j(t_3) \ldots\ldots\ldots eq.(2)$$

where H is crustal thickness, K is Vp/Vs ratio, and $r_j(t_i)$ is the j^{th} RF at times t_1, t_2, and t_3 which are the predicted times for T_{Ps}, T_{PpPs} and $T_{psSs+PsPs}$ respectively. The equation will sum all N RFs traces collected from one station. During the stacking process, the weighting w_i was set as 0.5, 0.3, and 0.2. for w_1, w_2, and w_3 respectively. Higher weighting is applied to the Ps arrival which generally has the largest signal, and less weight is put on the multiples. We tried a number of different weighting schemes and found that the best results were achieved with the above weights. Fig. 7 illustrates the different moveouts of the multiples relative to the primary Ps arrival as a function of ray parameter. The summation with the largest overall amplitude (summed over time for the primary and multiple waves) should correspond to the correct Moho depth and Vp/Vs ratio.

Crustal thickness and Vp/Vs ratio of the crust beneath Merapi and Merbabu volcano were analysed using the H-κ stacking method described above. The grid search range was set to 25 -40 km for Moho depth and 1.65 - 2.00 for Vp/Vs ratio. We used prior information from previous geophysical studies on crustal structure to constrain the upper and lower bounds (see Wölbern, 2016). Fig. 7 illustrates the results for station ME11 which has 52 high-quality RFs. We contoured the value of the stacked RFs as a function of Moho depth and Vp/Vs ratio with the highest value corresponding to the optimum parameters. The contour plot shows a clear maximum with a realistic number for crustal thickness (28.1 km) and crustal Vp/Vs ratio (1.80). The predicted Moho Ps arrival times agree with the RF signals which show a strong positive converted wave at 3.3 s. Note that predicted times for the multiples are also plotted in Fig. 7.

The H-κ method has several benefits such as fast computation time and no requirement to pick arrival times. However, the main weakness of the method is that the theoretical arrival times for the converted waves assumes a single crustal layer with a flat Moho. As such, the method may fail to produce meaningful results in a range of cases, such as a dipping Moho in a subduction zone or when multiple layers featuring strong velocity contrasts across interfaces are present e.g. when sedimentary basins are present. We observed that some RFs in our study area do not show a strong Ps converted wave and instead feature a complex waveform. As noted earlier, this may be due to multiple layers of sediment and volcanics that have large impedance contrasts with the basement, such that the multiple reflections interfere with the Moho signal. We have 11 stations out of a total of 51 which failed to constrain realistic numbers for Moho depth and Vp/Vs ratio. In cases where Moho depth cannot be derived from the H-κ method, we estimate Moho depth directly from the stacked RF, which is migrated using the velocity model obtained from seismic tomography by Ramdhan *et al.* (2018), by picking the peak corresponding to the Ps phase. This method likely has greater uncertainty in the depth. We estimated the depth uncertainty from this method around ± 2-3 km based on a bootstrap method explained below.

RESULTS AND DISCUSSION

The H-κ stacking method– was applied to all data collected by the DOMERAPI array. Altogether, 40 reliable Vp/Vs ratio measurements and 51 reliable crustal thickness measurements were obtained. The results of the RF analysis are shown in Figs. 9 and 10 as interpolated crustal thickness and Vp/Vs ratio maps respectively (see supplementary section for the contoured plots of S(H,K) and receiver functions from all available stations). The Zhu and Kanamori method (2000) provides a simple means of calculating uncertainties by measuring the flatness of the peak in the plot of S(H,K). For stations where the H-κ method does not work, we use the depth of the Moho Ps conversion obtained by using Vp/Vs ratios of 1.75 and 1.85, which provides a bound on the range of plausible values. We also performed a bootstrapping method (Efron and Tibshirani, 1991) to separately estimate uncertainty for each station. We generated 100 random populations of receiver functions from the total pool available for each station and computed the standard deviation (σ) of the depth variations between the populations. The results of the RF analysis are listed in Table 1 and 2 along with the 2σ errors.

Fig. 9 shows a map of crustal thickness estimated from stacked RFs and the H-κ method. The average crustal thickness is 29.4 km and ranges from 26.7 to 32.5 km. Crustal thickness varies from about 32 km in the southern part of the study area, then gets thinner near Mt. Merapi before thickening again beneath Mt. Merbabu (see Figure 9). Further north, it thins to about 29 km thick. The other regions do not show a very distinct change, averaging around 29-30 km thick. Fig. 10 illustrates stacked RFs using a velocity model obtained from a prior tomography study from southwest to northeast across Mt. Merapi. Most stacked RFs show waveform complexity such that the Ps converted wave from the Moho is not the strongest positive signal that follows the incoming P wave. This may be due to a number of factors, such as a gradational or suppressed Moho, which in this case may be due to the existence of a sizable magma reservoir at Moho depths, which was identified in a recent local earthquake tomography study (Widiyantoro et al., 2018).

The average Vp/Vs ratio of the crust in this study is 1.80 (Fig. 11), which is slightly higher than the global average of 1.78 (Christensen 1996; Chevrot & van der Hilst 2000). However, there is a large range in values, from 1.70 to 1.99, with two regions having abnormally high crustal Vp/Vs ratios. One of these regions is located close to the active

Merapi volcano, where four stations located at the southwestern edge have Vp/Vs ratios of 1.85 or greater. To the north of these stations, near the Merbabu volcano, the Vp/Vs ratio is closer to average. The second region, located to the northeast of the network, shows a band of high Vp/Vs ratios ranging from 1.85 to 1.87.

Average crustal Vp/Vs can be used to constrain the petrology and physical state of the crust. Christensen (1996) showed from laboratory experiments that Vp/Vs ratio does not significantly vary as a function of reasonable crustal temperatures (0-400^{o} C) and pressure changes greater than 100-200 Mpa. The primary factors that control the Vp/Vs ratio in the crust are the presence of melt or fluids and changes in mineralogy. The relative abundance of quartz and plagioclase feldspar has a strong effect on Vp/Vs (Christensen, 1996): for felsic quartz-rich rocks such as granite, Vp/Vs is 1.71; intermediate rocks have a Vp/Vs ratio of near 1.78 and mafic plagioclase-rich rocks such as gabbro have a Vp/Vs ratio near 1.87. The average composition for continental crust is close to andesite or diorite (Anderson, 1989) and laboratory measurements by Carmichael (1982) confirmed that Vp/Vs for diorite at crustal pressures ranges from 1.75 to 1.79. In the case of partial melt, Hammond and Humphreys (2000) show that 2% partial melting can increase Vp/Vs ratio by as much as 10% in the uppermost mantle.

The high Vp/Vs ratio regions could indicate a very mafic crust or the presence of high pore pressure fluids or partial melt. Thus, we suggest that the high Vp/Vs ratios we observe near Mt. Merapi are due to partial melt or high fluid content within the crust, although some mafic underplating of the crust could also contribute

To better understand the crust beneath Mt. Merapi and Mt. Merbabu, we plot cross-sections which show elevation, crustal depth and Vp/Vs ratio along a line from south to north (see Figure 12). The location of the cross-section is marked on Fig. 9. Interestingly, Mt Merapi has thinner crust (by about 3 km) compared to Mt. Merbabu and a higher Vp/Vs ratio

(1.9 vs 1.73). Recent local earthquake tomography results (Widiyantoro *et al*, 2018) which exploited data from the same network used in this study found three active areas with high Vp/Vs: the first is a shallow zone interpreted to represent a region of intense fluid percolation, directly below the summit of the volcano; the second is thought to be a pre-eruptive magma reservoir at 10 to 20 km depth below MSL that is several orders of magnitude larger than known erupted magma volumes; and the third is a deep magma reservoir at 30 km depth which supplies the main reservoir. We suggest that the zone of partial melting, magma reservoir and volcanic sediments may be responsible for the higher Vp/Vs ratio observed in this study. These results appear to support the observation that Mt. Merbabu is much less volcanically active than Mt. Merapi.

In Fig. 13, we plot station elevation as a function of crustal thickness derived from our analysisοn a map of topography. In the case of Airy isostacy, the thickness of a crustal root has a linear relationship with excess topography, so a deeper Moho should be compensated with greater elevation.

In our case, the scatterplot in Figure 13 appears to reveal no obvious correlation between elevation and crustal thickness. In attempt to quantify a trend, we compute the correlation coefficient, and find that r^2=0.1292. This implies a lack of correlation between crustal thickness and topography, and hence an Airy isostacy model is not applicable for our study area. However, given the footprint of the volcanic edifices (a few 10s of km), this is perhaps unsurprising since the flexural strength of the lithosphere should be more than sufficient to support narrowly distributed loads of this sort. Isostatic equilibrium is instead maintained over distances of 100s of km (see Watts, 2001), which means that locally one should not expect a correlation between crustal thickness and elevation. .

CONCLUSIONS

We have calculated the crustal thickness and bulk crustal Vp/Vs ratio beneath Mt. Merapi and Mt. Merbabu. RFs that feature a complex signal are likely influenced by near surface sedimentary layering and the presence of volcanic rocks. Crustal thickness does not vary strongly beneath the study region, but a shallower Moho is found beneath Mt. Merapi, along with a higher Vp/Vs ratio (~1.86) which points to a more active volcano with partial melting and a hydrous zone. These results agree with recent tomographic models that shows a low velocity zone and multiple zones of higher Vp/Vs ratio beneath Mt. Merapi that extend from the near surface to the base of the crust. The northern part of our study area also shows higher Vp/Vs ratio that may be related to the Kendeng Basin. Future work will involve the inversion of receiver functions for depth dependent shear wave velocity beneath individual stations, which has the potential to better recover the true complexity of subsurface seismic structure beneath the two volcanoes. Further insight can also be gained from the strong variations in teleseismic arrival time residuals that have been observed across the network.

ACKNOWLEDGEMENTS

We are grateful to the French National Research Agency and Institut de recherche pour le développemen for funding the DOMERAPI project. We would also like to express our gratitude to PVMBG as the main partner of the DOMERAPI project in Indonesia. This study was supported in part by Direktorat Perguruan Tinggi (DIKTI), the Republic of Indonesia, through a WCU research grant 2017/2018, and a 2018 research grant from Institut Teknologi Bandung (ITB) awarded to SW. We used the Generic Mapping Tools (Wessel & Smith, 1998) to create figures presented in this study.

References

Anderson, D. L., 1989. Theory of the Earth. Blackwell Scientific Publications, Boston, p. 366

Beauducel, F. & Cornet, F.H., 1999. Collection and three-dimensional modeling of GPS and tilt data at Merapi volcano, Java, *J. Geophys. Res*., **104**(B1), 725–736.

Bohm, M., Haberland, C. & Asch, G., 2013. Imaging fluid-related subduction processes beneath Central Java (Indonesia) using seismic attenuation tomography, *Tectonophysics,* **590**, 175–188. http://dx.doi.org/10.1016/j.tecto.2013.01.021.

Bostock, M. G., Hyndman, D. R., Rondenay, S. & Peacock, M. S., 2002. An inverted continental Moho and serpentinization of the forearcmantle, *Nature*, **417**, 536–539.

Carmichel, R. S., 1982. Magnetic properties of rocks and minerals, in Carmichael, R. S. (Ed.): Handbook of Physical Properties of Rocks, Vol. II, CRC Press, Boca Raton, 345 p.

Camus, G., Gourgaud, A., Mossand-Berthommier, P.-C. & Vincent, P. M., 2000. Merapi (Central Java, Indonesia): an outline of the struc-tural and magmatological evolution, with a special emphasis to the major pyroclastic events, *J. Volcanol. Geotherm. Res*., **100**, 139–163.

Chevrot, S. & van der Hilst, R. D., 2000. The Poisson's ratio of the Australian crust: geological and geophysical implications, *Earth Planet. Sci. Lett*., **183**, 121–132.

Christensen, N. I., 1996. Poisson's ratio and crustal seismology, *J. Geophys.Res*., **101**(B2), 3139–3156.

Clements, B., Hall, R., Smyth, H. R. & Cottam, M. A., 2009. Thrusting of a volcanic arc: a new structural model for Java, *Petrol. Geosci.,* **15**, 159–174. http://dx.doi.org/10.1144/1354-079309-831.

Efron, B., and R. Tibshirani (1991), Statistical data analysis in the computer age, Science, 253, 390–395.

Gertisser, R. & Keller, J., 2003. Temporal variations in magma composition at Merapi Volcano (Central Java, Indonesia): Magmatic cycles during the past 2000 years of explosive activity, *J. Volcanol. Geotherm. Res*., 1-23. 10.1016/S0377-0273(03)00025-8.

Hidayati, S., Ishihara, K., Iguchi, M. & Ratdomopurbo, 2008. Focal mechanism of volcano-tectonic earthquake at Merapi volcano, Indonesia, *Indonesian J. Phys*., **19**(2), 75 - 82.

International Seismological Centre, 2019. ISC-EHB dataset https://doi.org/10.31905/PY08W6S3

Kennett, B.L.N. Engdahl, E.R. & Buland R., 1995. Constraints on seismic velocities in the Earth from travel times, *Geophys J Int*, **122**, 108-124

Koulakov, I., Bohm, M., Asch, G., Lühr, B.-G., Manzanares, A., Brotopuspito, K. S., Fauzi, P., Purbawinata, M. A., Puspito, N. T., Ratdomopurbo, A., Kopp, H., Rabbel, W. & Shevkunova, E., 2007. P and S velocity structure of the crust and the upper mantle beneath central Java from local tomography inversion, *J. Geophys. Res*., **112**, B08310, http://dx.doi.org/10.1029/2006JB004712.

Langston, C. A., 1977. Corvallis, Oregon, Crustal and upper mantle structure from teleseismic P and S waves, *Bull. Seismol. Soc. Am*., **67**, 713–724.

Muirhead, K .J., 1968. Eliminating false alarms when detecting seismic events automatically, *Nature*, **217**, 533-534.

Owens, T. J., 1984. Determination of crustal and upper mantle structure from analysis of broadband teleseismic P-waveforms, Ph.D. thesis, Department of Geology and Geophysics, The University of Utah.

Ramdhan, M., Widiyantoro, S. Nugraha, A. D., Métaxian, J.-P., Rawlinson, N., Saepuloh, A., Kristyawan, S., Sembiring, A. S., Budi-Santoso, A., Laurin, A. & Fahmi, A. A., 2019. Detailed seismic imaging of Merapi volcano, Indonesia, from local earthquake travel-time tomography, *J. Asian Earth Sci.* Vol 177, p134-135.

Ratdomopurbo, A. & Poupinet, G., 2000. An overview of the seismicity of Merapi volcano (Java, Indonesia), 1983–1994, *J. Volcanol. Geotherm. Res.,* **100**, 193–214. https://doi.org/10.1016/S0377-0273(00)00137-2.

Simons, W. J. F., Socquet, A., Vigny, C., Ambrosius, B. A. C., Haji Abu, S., Chaiwat Promthong, Subarya, C., Sarsito, D. A., Matheussen, S., Morgan, P. & Spakman, W., 2007. A decade of GPS in Southeast Asia: Resolving Sundaland motion and boundaries, *J. Geophys. Res*., **112**, doi:10.1029/2005JB003868.

Smyth, H. R., Hall, R. & Nichols, G. J., 2008. Cenozoic volcanic arc history of east Java, Indonesia: the stratigraphic record of eruptions on an active continental margin, In: Draut, A. E., Clift, P. D., Scholl, D. W. (Eds.), Formation and Applications of the Sedimentary Record in Arc Collision Zones, *Geol. Soc. Am. Spec.,* Paper 436, pp. 199–222. http://dx.doi.org/10.1130/2008.2436(10).

Suhardja, S. K., 2013. Mapping the Rivera and Cocos subduction zone, Ph.D. thesis, Department of Geological Science, The University of Texas at Austin.

Suhardja, S. K., Grand, S. P., Wilson, D., Guzman-Speziale, M., Gomez-Gonzalez, J. M., Dominguez-Reyes, T. & Ni, J., 2015. Crust and subduction zone structure of

Southwestern Mexico. *J. Geophys. Res. Solid Earth*, 120: 1020–1035, doi: 10.1002/2014JB011573.

Surono, Jousset, P., Pallister, J., Boichu, M., Buongiorno, M.F., Budisantoso, A., Costa, F., Andreastuti, S., Prata, F., Schneider, D., Clarisse, L., Humaida, H., Sumarti, S., Bignami, C., Griswold, J., Carn, S., Oppenheimer, C. & Lavigne, F., 2012. The 2010 explosive eruption of Java's Merapi volcano—A "100-year" event, *J. Volcanol. Geotherm. Res.* **241–242**, 121–135, https://doi.org/10.1016/j.jvolgeores.2012.06.018.

Tiede, C., Camacho, A. G., Gerstenecker, C., Fernández, J. & Suyanto, I., 2005. Modeling the density at Merapi volcano area, Indonesia, via the inverse gravimetric problem, *Geochem. Geophys. Geosyst*., **6**, Q09011, doi:10.1029/2005GC000986.

Untung, M. & Sato, Y., 1978. Gravity and Geological Studies in Java, Indonesia, *Spec. Publ.* **6**, 207 pp., Geol. Surv. of Indonesia, Bandung.

Wagner, D., Koulakov, I., Rabbel, W., Luehr, B.-G., Wittwer, A., Kopp, H., Bohm, M., Asch, G. & MERAMEX Scientists, 2007. Joint inversion of active and passive seismic data in Central Java, *Geophys. J. Int.,* **170**, 923–932. http://dx.doi.org/10.1111/j.1365-246X.2007.03435.x.

Wessel, P., Smith, W.H.F., 1998. New, improved version of Generic Mapping Tools Released, *EOS Trans*., *AGU* **79**, 579, doi: 10.1029/98EO00426.

Weston, J., Engdahl, E. R., harris, J., Di Giacomo, D., Stochak, D. A. 2019. ISC-EHB: reconstruction of a robust earthquake data set. Geophysical Journal International, 124, 474-484

Widiyantoro, S., Ramdhan, M., Metaxian, J. P., Cummins, P. R., Martel, C., Erdmann, S., Nugraha, A.D., Budi-Santoso, A., Laurin, A. & Fahmi, A.A., 2018. Seismic imaging and petrology explain highly explosive eruptions of Merapi Volcano, Indonesia, *Sci. Rep.*, **8**(1), 13656, https://doi.org/10.1038/s41598-018-31293-w.

Wölbern, I. & Rümpker, G., 2016. Crustal thickness beneath Central and East Java (Indonesia) inferred from P receiver functions, *J. Asian Earth Sci.,* **115**, 69–79, DOI: http://doi.org/10.1016/j.jseaes.2015.09.001.

Zhu, L. & Kanamori, H., 2000. Moho depth variation in southern California from teleseismic receiver functions, *J. Geophys. Res*., **105**(B2), 2969–2980.

Zulfakriza, Z., Saygin, E., Cummins, P.R., Widiyantoro, S., Nugraha, A.D., Lühr, B.-G. & Bodin, T., 2014. Upper crustal structure of central Java, Indonesia, from transdimensional seismic ambient noise tomography, *Geophys. J. Int.*, **197**, 630-635, doi: 10.1093/gji/ggu016.

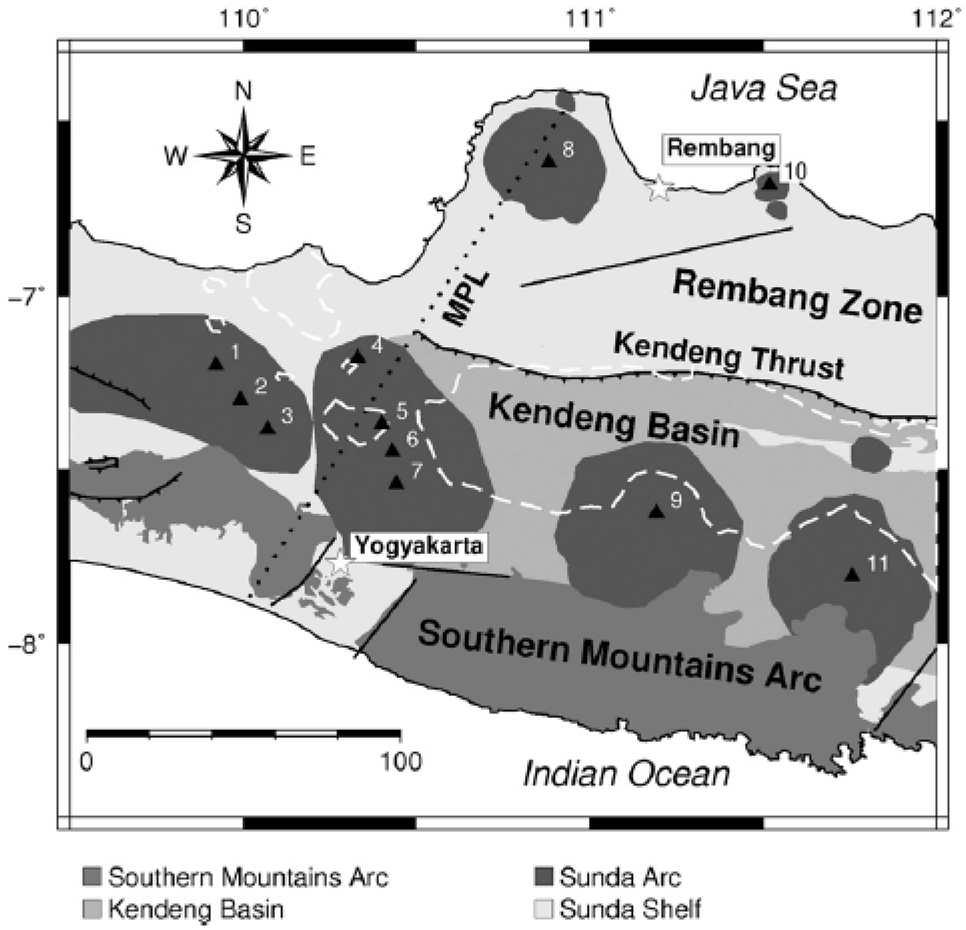

Figure 1. Simplified geological map of the study region from Smyth *et al*. (2008). The modern magmatic arc (Sunda Arc) is indicated by the darkest shading with young volcanoes numbered as, 1: Dieng volcanic complex; 2: Mt. Sundoro; 3: Mt. Sumbing; 4: Mt. Ungaran; 5: Mt. Telomoyo; 6: Mt. Merbabu; 7: Mt. Merapi; 8: Mt. Muria; 9: Mt. Lawu; 10: Mt. Lasem; 11: Mt. Wilis. The dotted line is the Muria-Progo lineament (Smyth *et al*. 2008); the white dashed line indicates the 0 mGal contour of the negative Bouguer gravity anomaly (min. −58 mGal) which is located in the thickest part of the Kendeng Basin.

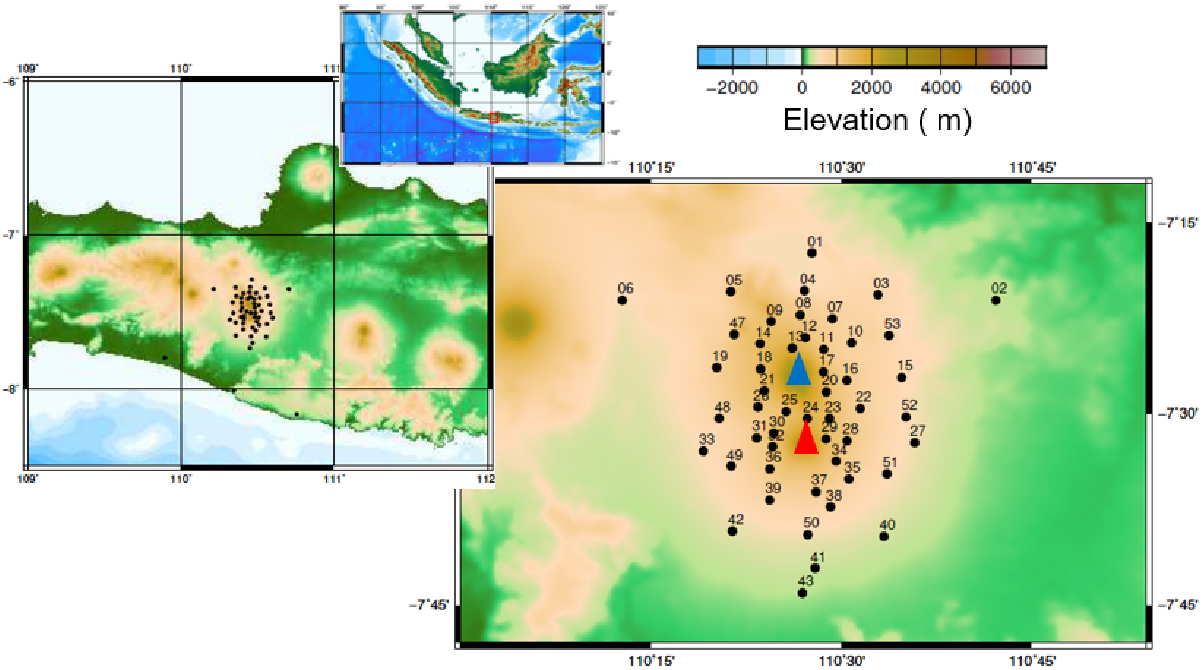

Figure 2. Location of seismometers installed in the vicinity of Mt. Merapi (red triangle) and Mt. Merbabu (blue triangle) as part of the DOMERAPI experiment. The small inset shows the location of the study area relative to southeast Asia.

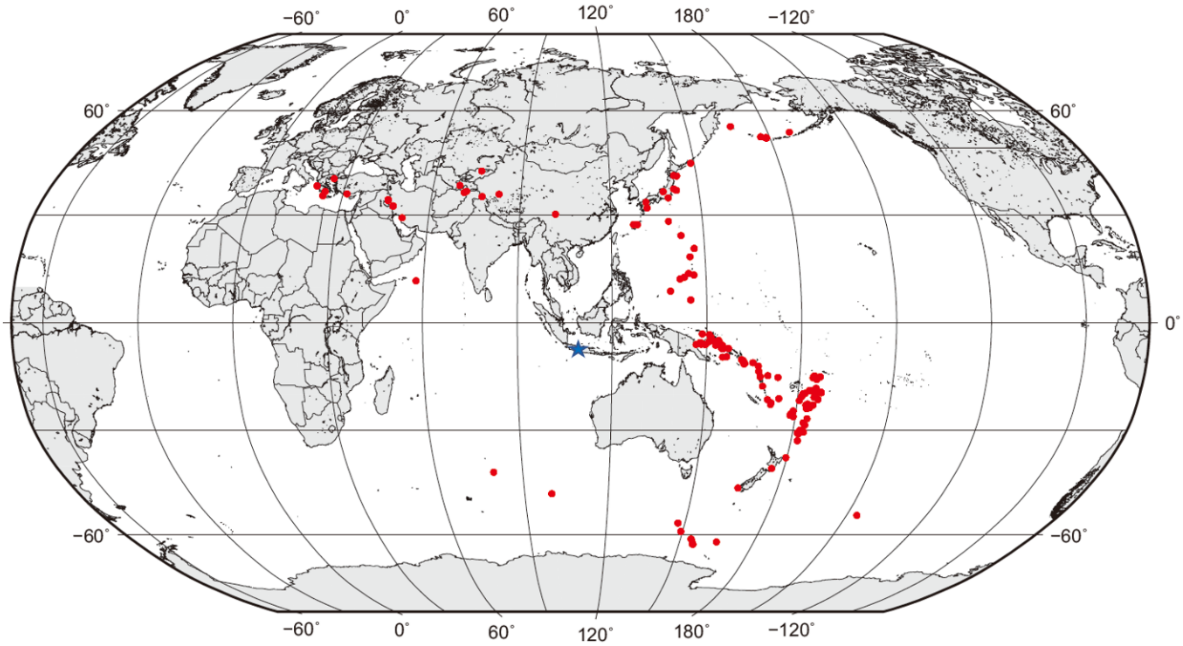

Figure 3. Teleseismic events used in this study. The DOMERAPI network is located in the centre of the projection.

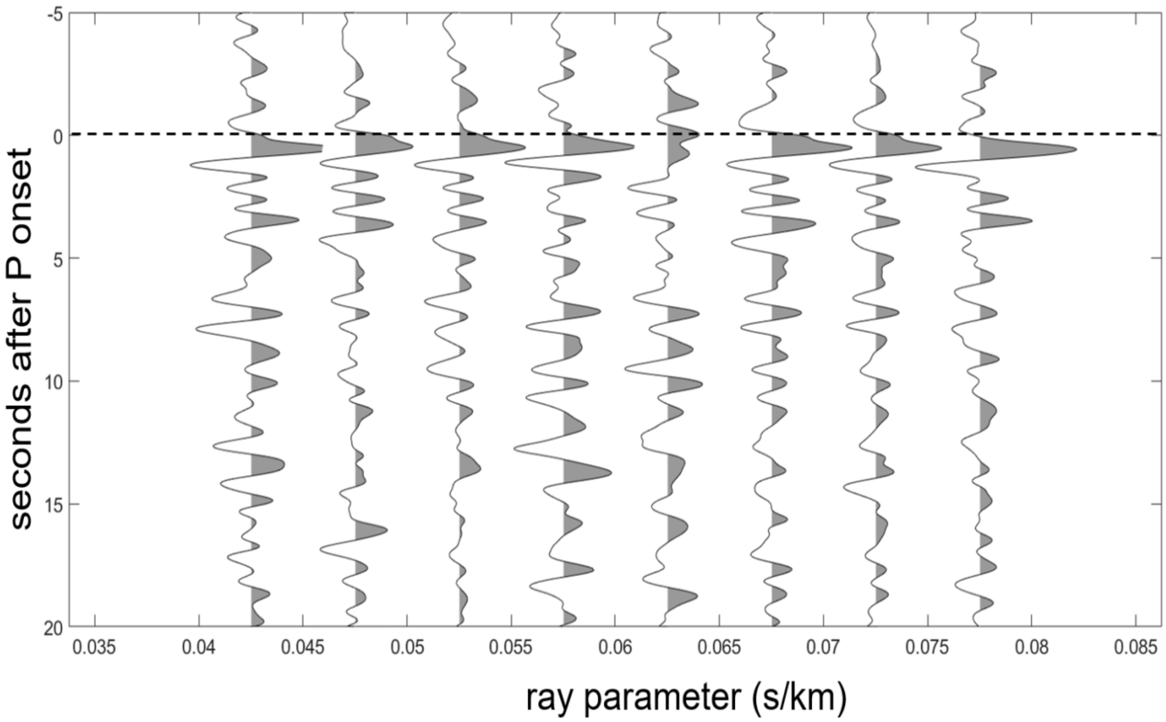

Figure 4. An example of stacked RFs for station ME29 as a function of ray parameter. High amplitude pulses at 0 sec represent the direct P arrival. The vertical axis represents seconds after the P onset.

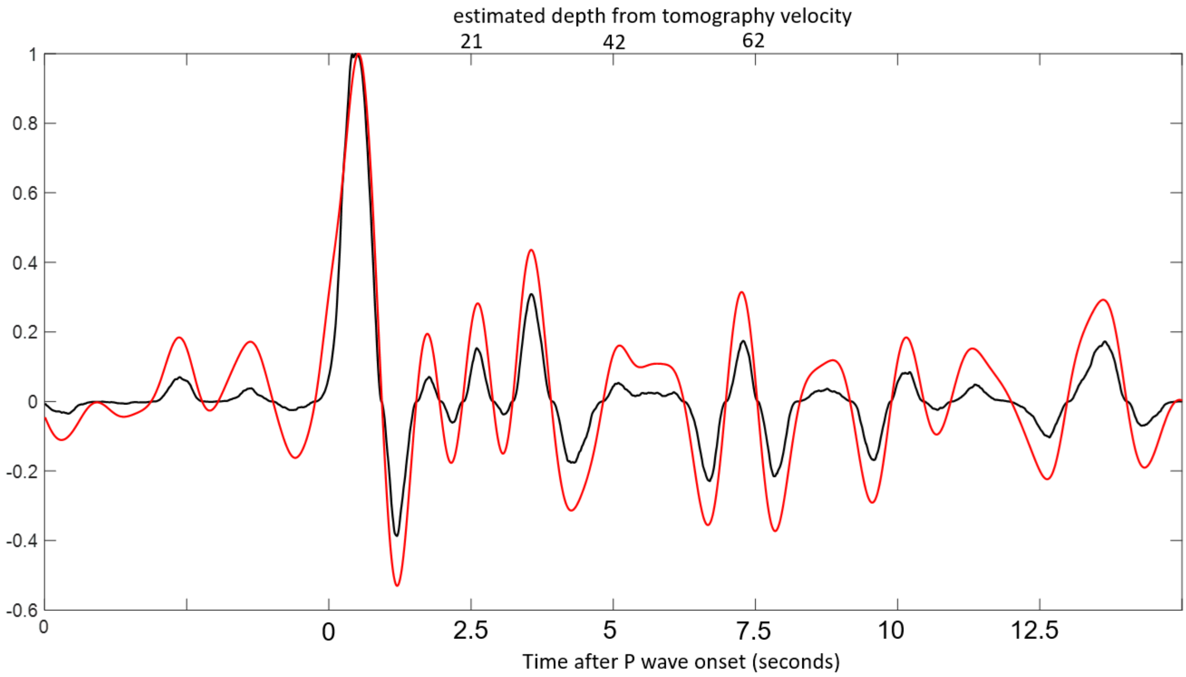

Figure 5. RF stack for all events at station ME29. The black line is the 2nd root stack used to improve the signal to noise ratio. The red line represents the original linear stack.

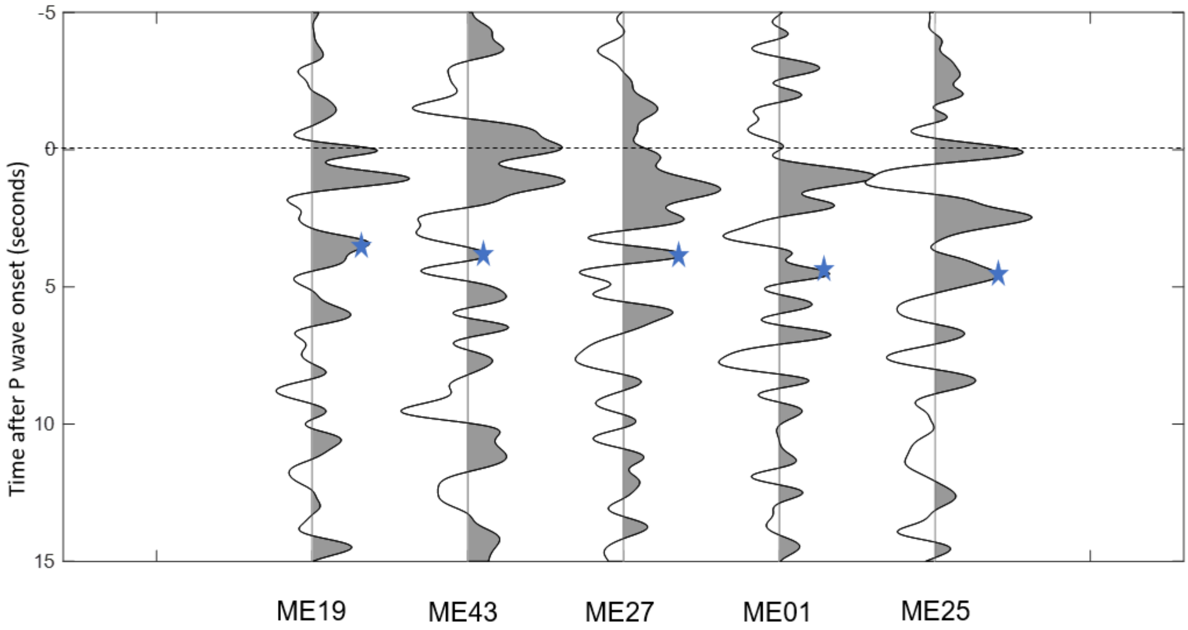

Figure 6. Stacked RFs at stations to the west (ME19), south (ME43), east (ME27), north (ME01) and on Mt. Merapi (ME25). Blue star denotes pick of the Ps conversion.

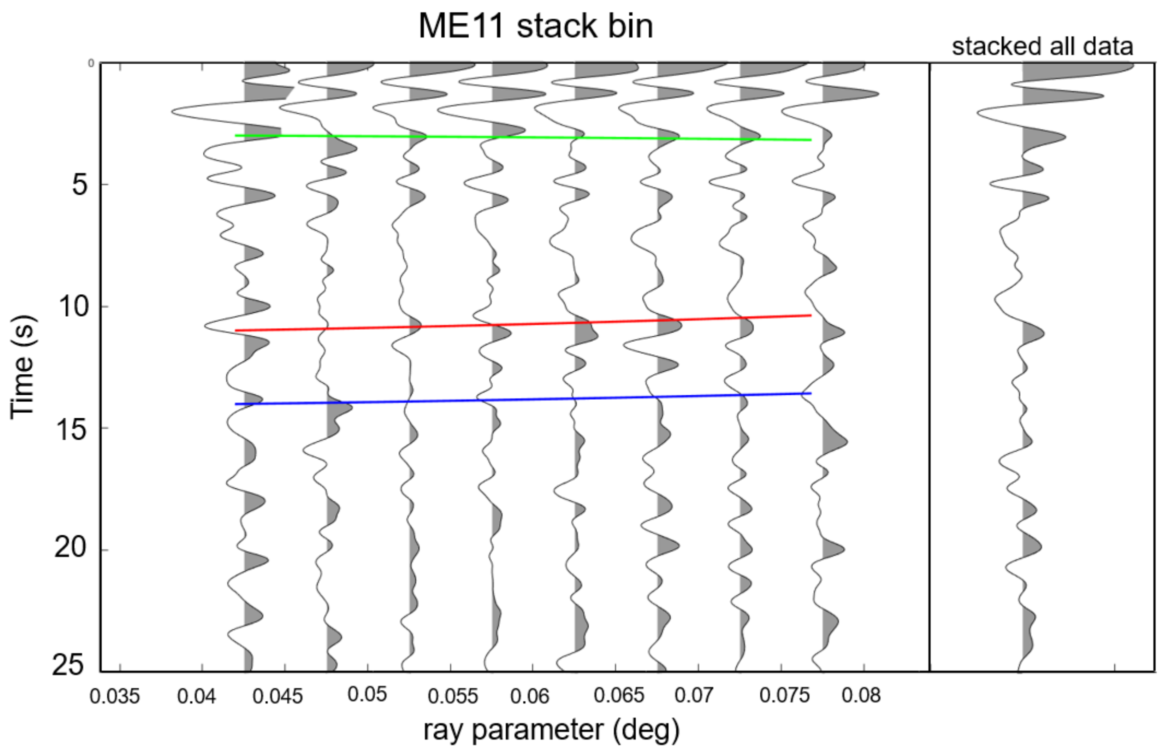

Figure 7. RF traces that have been binned with respect to ray parameter at station ME11. The predicted Ps, PpPs, and PpSs arrivals are represented using green, red and blue lines respectively. Note the relative change in times between the three arrivals as a function of ray parameter. The green line is the predicted Ps time assuming a crustal thickness of 28.1 km and a Vp/Vs ratio of 1.80. The red line is the predicted time for PpPs and the blue line is the predicted time for PpSs using the same crustal model. The right figure shows a stack of all available traces.

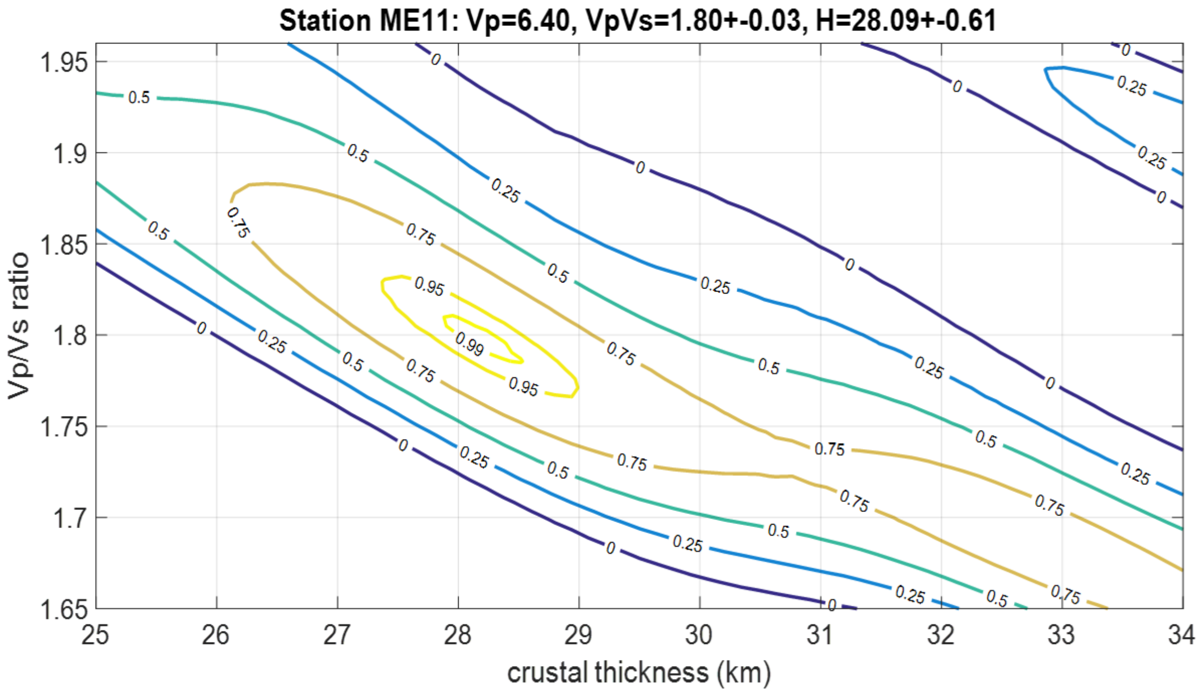

Figure 8. Contours of stack amplitudes for station ME11 as a function of crustal thickness H and Vp/Vs ratio. The grid search calculates the stack amplitude of all available RFs for a range of possible crustal thicknesses (25-40 km) and Vp/Vs ratios (1.65-2.0). The final result is taken by choosing the highest amplitude from the contour, and uncertainty is calculated by measuring the flatness of the contour peak.

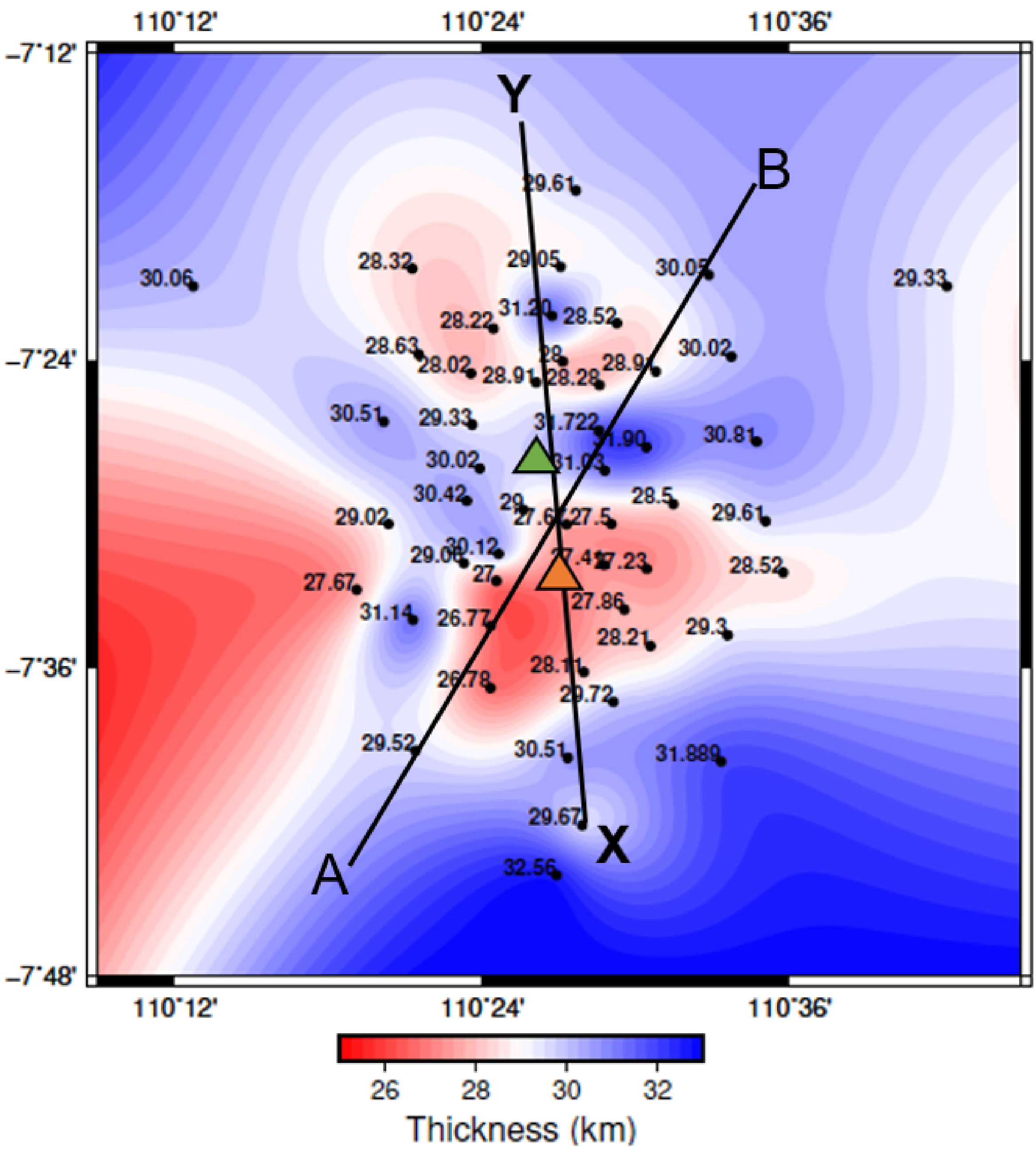

Figure 9. An interpolation of crustal thickness measurements using the H-κ method. The measured crustal thickness beneath individual stations is also given with units of km. Thinner crust is seen near Mt Merapi. The X-Y line denotes the location of the cross section shown in Fig. 11. The A-B line shows the location of the cross section shown in Figure 10~~9a~~. Mt. Merapi is denoted by the amber triangle and Mt. Merbabu by the green triangle.

.

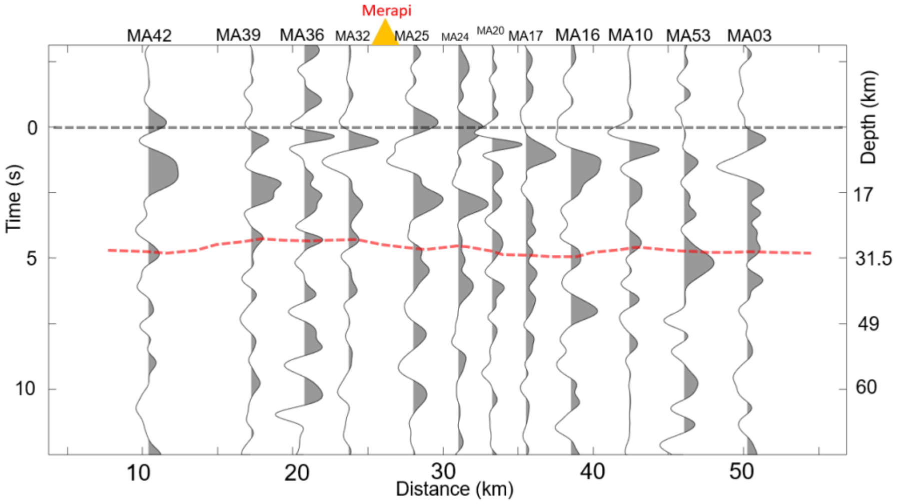

Figure 10. Plot of stacked RFs from south west to north east (line A-B at Fig 9). Horizontal axis is distance in km, vertical axis on the left is time (s), and vertical axis on the right is the estimated depth. Orange triangle shows the location of Mt Merapi. Red dashed line shows interpolated crustal thickness from this study.

Commented [1]: I still wonder why the initial P-phase is not aligned at zero for all traces.

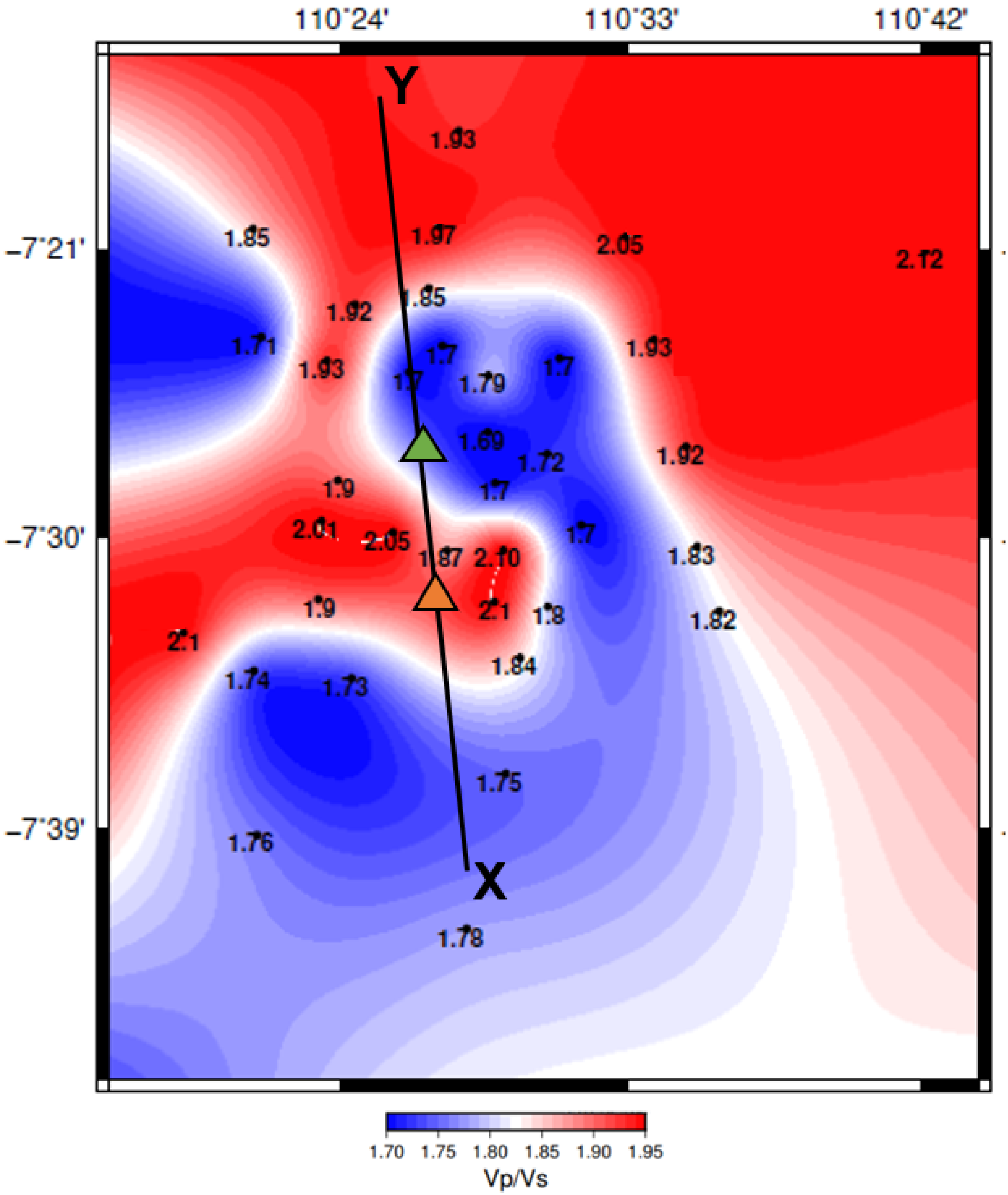

Figure 11. Individual measurements of the bulk crustal Vp/Vs ratio along with an interpolated map made using splines under tension. Mt. Merapi is denoted by the amber triangle and Mt. Merbabu by the green triangle.

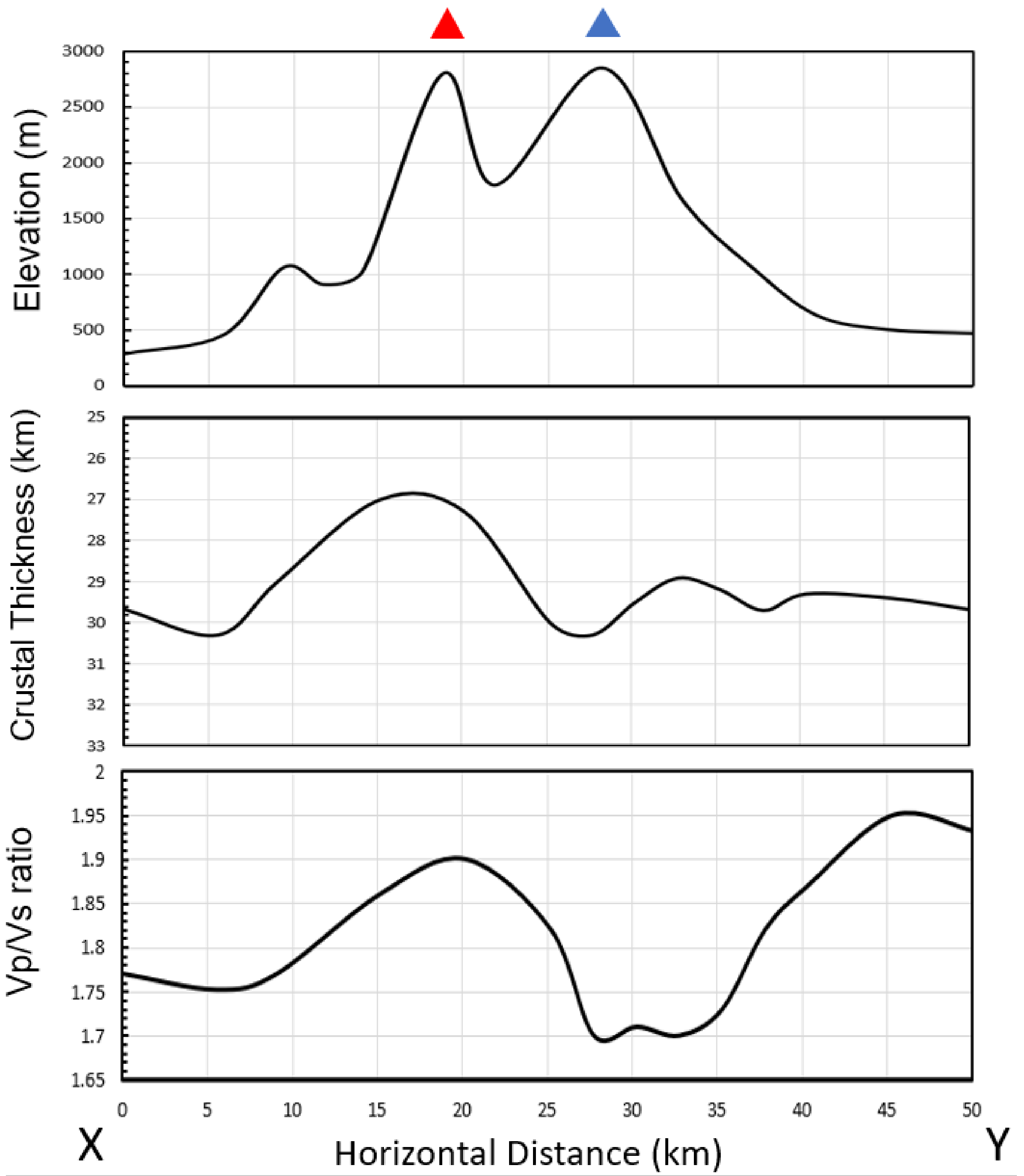

Figure 12. Top panel: Elevation cross section from south to north across Mt. Merapi (red triangle) and Mt. Merbabu (blue triangle) – see Figure 9 for the location of the X-Y section. Middle panel: Interpolated crustal thickness estimate along the same line. Bottom panel: Interpolated Vp/Vs ratio from H-K stacking.

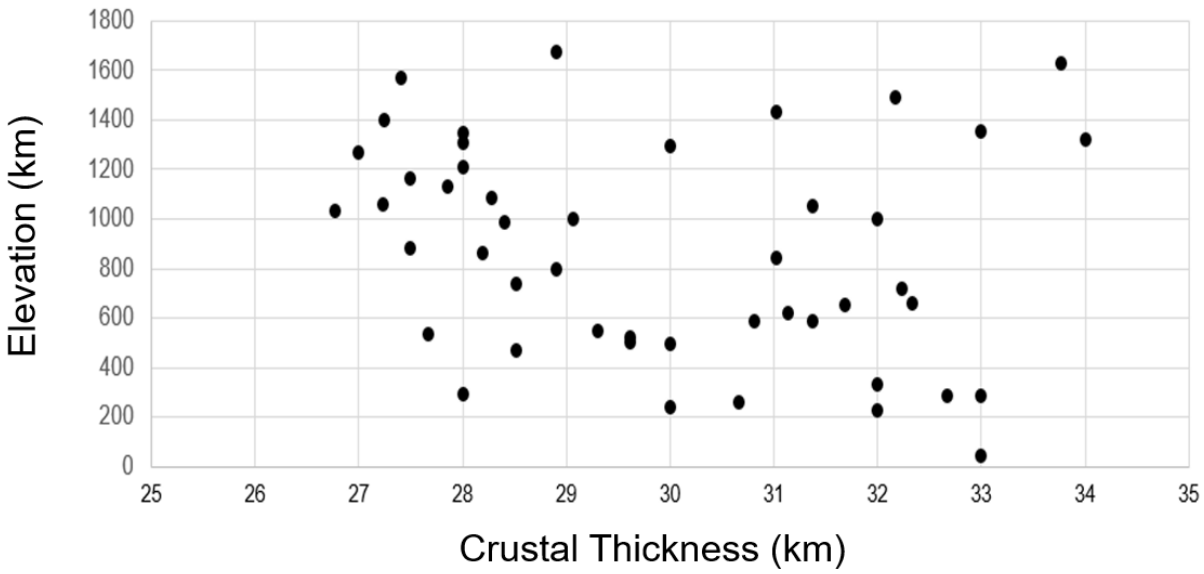

Figure 13. Crustal thickness measurement vs elevation. Elevation data were taken from the National Oceanic and Atmospheric Administration website (www.noaa.gov).

Station name	Area name	Latitude (°)	Longitude(°)	Elevation (m)	Number of RFs	Thickness (km)		Uncertainty (km)	Vp/Vs ratio		Uncertainty (km)
ME01	"Daren"	-7.29	110.4609	504	41	29.61	±	1.5	1.93	±	0.07
ME02	"Wates Barat"	-7.3523	110.7024	291	28	29.33	±	2.1	2.12	±	0.15
ME03	"Brangkongan"	-7.3449	110.5475	653	33	30.05	±	1.7	1.72	±	0.06
ME04	"Kebrok"	-7.3396	110.451	589	26	29.05	±	2.3	1.93	±	0.07
ME05	"Ngrancah"	-7.3407	110.3544	865	51	28.32	±	1.1	1.89	±	0.04
ME08	"Bumiayu"	-7.3714	110.4454	1052	47	31.2	±	1.9	1.85	±	0.04
ME09	"Bangongan"	-7.3798	110.4073	1311	45	28.22	±	0.8	1.92	±	0.08
ME10	"Nganggrung"	-7.4077	110.513	799	53	28.91	±	2.1	1.7	±	0.09
ME11	"Kumpulrejo"	-7.4165	110.4763	1083	52	28.28	±	1.3	1.79	±	0.05
ME12	"Kulian"	-7.4011	110.4524	1211	38	28	±	2.3	1.7	±	0.08
ME13	"Ngeyo"	-7.4148	110.4351	1674	47	28.91	±	3.2	1.7	±	0.12
ME14	"Banaran"	-7.4089	110.3927	1350	33	28	±	2.8	1.9	±	0.05
ME15	"Dawung"	-7.4532	110.5786	586	45	30.81	±	2.3	1.92	±	0.08
ME16	"Kembang"	-7.4569	110.5068	997	29	31.9	±	1.7	1.72	±	0.04
ME17	"Glagah"	-7.4459	110.476	1492	30	31.72	±	1.9	1.7	±	0.09
ME20	"Gunungsari"	-7.4721	110.4797	1434	47	31.03	±	1.8	1.7	±	0.11
ME21	"Sobleman"	-7.4707	110.3983	1400	49	30.02	±	2.1	1.9	±	0.07
ME22	"Tumangsari"	-7.4938	110.5243	842	52	28.5	±	1.5	1.7	±	0.08
ME23	"Genting"	-7.5068	110.484	1355	49	27.5	±	3.2	1.77	±	0.04
ME24	"Plalangan"	-7.5069	110.4548	1628	51	27.67	±	4.3	1.86	±	0.06
ME25	"Kajor"	-7.4976	110.4269	1321	44	29	±	4.7	1.79	±	0.05
ME26	"Wonolelo"	-7.4917	110.3899	1163	45	30.42	±	3.2	1.7	±	0.07
ME27	"Pulisen"	-7.5383	110.5958	467	49	28.52	±	1.8	1.82	±	0.07
ME28	"Pusung"	-7.536	110.5071	1062	54	27.23	±	2.1	1.8	±	0.05
ME29	"Lendong"	-7.5335	110.4793	1567	47	27.41	±	2.5	1.78	±	0.06
ME31	"Tempel"	-7.5322	110.3882	1000	19	29.06	±	1.2	1.9	±	0.12
ME33	"Garonan"	-7.5494	110.3183	534	18	27.67	±	2.1	1.7	±	0.09
ME34	"Candi"	-7.5624	110.4926	1132	45	27.86	±	2.2	1.84	±	0.03
ME36	"Kaliurang"	-7.5729	110.4055	1034	22	26.77	±	3.1	1.73	±	0.04
ME37	"Balerante"	-7.6029	110.4662	887	19	27.87	±	2.9	1.74	±	0.05
ME38	"Karangkendal"	-7.6223	110.4853	662	47	29.72	±	3.5	1.75	±	0.02
ME39	"Kemiri Kebo"	-7.6134	110.4054	717	22	27	±	2.9	1.75	±	0.08
ME40	"Randulanang"	-7.661	110.5555	331	22	32	±	2.6	1.83	±	0.06
ME41	"Purwobinangun"	-7.7024	110.465	287	45	29.67	±	3.4	1.78	±	0.05
ME42	"Bangunharjo"	-7.65405	110.35652	287	47	29.52	±	2.7	1.76	±	0.04
ME43	"Salakan"	-7.7349	110.4484	228	24	32	±	3.1	1.74	±	0.06
ME47	"Gunung Andong"	-7.39663	110.35875	989	24	28.63	±	2.1	1.71	±	0.07
ME49	"Tegal Randu"	-7.56907	110.3549	623	8	31.14	±	3.1	1.74	±	0.05
ME52	"Penggung"	-7.50483	110.58432	524	11	29.61	±	2.6	1.83	±	0.05
ME53	"Kenteng"	-7.39794	110.56211	0	13	30	±	1.4	1.93	±	0.08

Station name	Latitude	Longitude	Elevation (m)	Thickness (km)			Vp/Vs ratio		
ME01	-7.29	110.4609	504	29.61	±	1.5	1.93	±	0.07
ME02	-7.3523	110.7024	291	29.33	±	2.1	2.12	±	0.15
ME03	-7.3449	110.5475	653	30.05	±	1.7	1.72	±	0.06
ME04	-7.3396	110.451	589	29.05	±	2.3	1.93	±	0.07
ME05	-7.3407	110.3544	865	28.32	±	1.1	1.89	±	0.04
ME08	-7.3714	110.4454	1052	31.2	±	1.9	1.85	±	0.04
ME09	-7.3798	110.4073	1311	28.22	±	0.8	1.92	±	0.08
ME10	-7.4077	110.513	799	28.91	±	2.1	1.7	±	0.09
ME11	-7.4165	110.4763	1083	28.28	±	1.3	1.79	±	0.05
ME12	-7.4011	110.4524	1211	28	±	2.3	1.7	±	0.08
ME13	-7.4148	110.4351	1674	28.91	±	3.2	1.7	±	0.12
ME14	-7.4089	110.3927	1350	28	±	2.8	1.9	±	0.05
ME15	-7.4532	110.5786	586	30.81	±	2.3	1.92	±	0.08
ME16	-7.4569	110.5068	997	31.9	±	1.7	1.72	±	0.04
ME17	-7.4459	110.476	1492	31.72	±	1.9	1.7	±	0.09
ME20	-7.4721	110.4797	1434	31.03	±	1.8	1.7	±	0.11
ME21	-7.4707	110.3983	1400	30.02	±	2.1	1.9	±	0.07
ME22	-7.4938	110.5243	842	28.5	±	1.5	1.7	±	0.08
ME23	-7.5068	110.484	1355	27.5	±	3.2	1.77	±	0.04
ME24	-7.5069	110.4548	1628	27.67	±	4.3	1.86	±	0.06
ME25	-7.4976	110.4269	1321	29	±	4.7	1.79	±	0.05
ME26	-7.4917	110.3899	1163	30.42	±	3.2	1.7	±	0.07
ME27	-7.5383	110.5958	467	28.52	±	1.8	1.82	±	0.07
ME28	-7.536	110.5071	1062	27.23	±	2.1	1.8	±	0.05
ME29	-7.5335	110.4793	1567	27.41	±	2.5	1.78	±	0.06
ME31	-7.5322	110.3882	1000	29.06	±	1.2	1.9	±	0.12
ME33	-7.5494	110.3183	534	27.67	±	2.1	1.7	±	0.09
ME34	-7.5624	110.4926	1132	27.86	±	2.2	1.84	±	0.03
ME36	-7.5729	110.4055	1034	26.77	±	3.1	1.73	±	0.04
ME38	-7.6223	110.4853	662	29.72	±	3.5	1.75	±	0.02
ME41	-7.7024	110.465	287	29.67	±	3.4	1.78	±	0.05
ME42	-7.65405	110.3565	287	29.52	±	2.7	1.76	±	0.04
ME47	-7.39663	110.3588	989	28.63	±	2.1	1.71	±	0.07
ME49	-7.56907	110.3549	623	31.14	±	3.1	1.74	±	0.05
ME52	-7.50483	110.5843	524	29.61	±	2.6	1.83	±	0.05
ME53	-7.39794	110.5621	0	30	±	1.4	1.93	±	0.08

Table 1. Crustal Thickness and Vp/Vs Ratio calculated from the H-κ method with 2σ uncertainty from a bootstrap method.

Station Name	Area name	Latitude (°)	Longitude (°)	Elevation (m)	Number of RFs	Thickness (km)	Uncertainty (km)
ME06	"Gandokan"	-7.3522	110.2119	496	13	30	2.4
ME07	"Randuacir"	-7.3763	110.4877	738	26	28.52	2.1
ME18	"Kragilan"	-7.44217	110.39342	1382	27	29.33	3.5
ME19	"Warangan"	-7.4402	110.3359	882	31	30.51	2.6
ME30	"Pos Babadan"	-7.5261	110.4107	1295	44	30.1	2.1
ME32	"Pos Gemer"	-7.5437	110.4093	1266	27	27.2	2.7
ME35	"Wonorejo"	-7.586	110.5095	788	19	28.21	1.5
ME44	"Candi"	-7.797	109.8938	45	12	33	3.7
ME45	"Watugajah"	-8.0097	110.3432	257	22	30.66	1.1
ME46	"Tileng"	-8.1646	110.7543	243	11	30	3.5
ME51	"Pager Jurang"	-7.57897	110.55963	549	5	29.3	4

Table 2. Crustal thickness estimated for stations which we have no independent control on Vp/Vs ratio. Uncertainty was calculated using a bootstrapping method.

Conflict of Interest and Authorship Conformation Form

Please check the following as appropriate:

- ✓ All authors have participated in (a) conception and design, or analysis and interpretation of the data; (b) drafting the article or revising it critically for important intellectual content; and (c) approval of the final version.

- ✓ This manuscript has not been submitted to, nor is under review at, another journal or other publishing venue.

- ✓ The authors have no affiliation with any organization with a direct or indirect financial interest in the subject matter discussed in the manuscript

- ✓ The following authors have affiliations with organizations with direct or indirect financial interest in the subject matter discussed in the manuscript:

Author's name	Affiliation
Dr. Sandy Kurniawan Suhardja	Pertamina University
Prof. Sri Widiyantoro	Institut Teknologi Bandung
Dr. Metaxian Jean-Philippe	Universite de Savoie Mont Blanc
Professor Nicholas Rawlinson	University of Cambridge
Dr. Mohamad Ramdhan	Indonesian Agency for Meteorology, Climatology and Geophysics
Dr. Agus Budi Santoso	Center for Volcanology and Geological Hazard Mitigation, Indonesia

Plots of RFs with respect to epicentral distance/ray parameter and H-K stack contour for all stations used in the network

Station ME01: Vp = 6.5, Vp/Vs = 1.93 ± 0.07, H = 29 ± 1.5

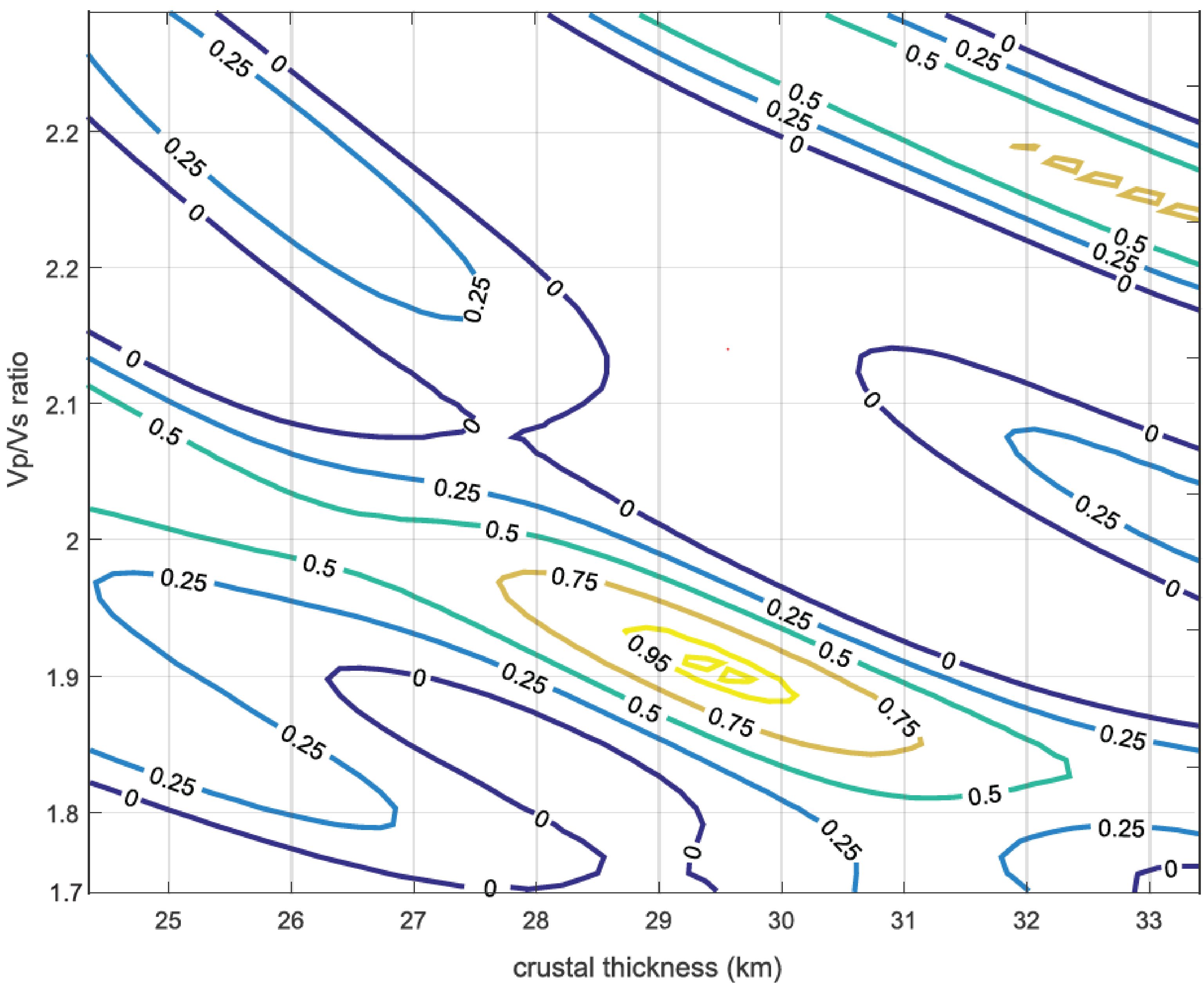

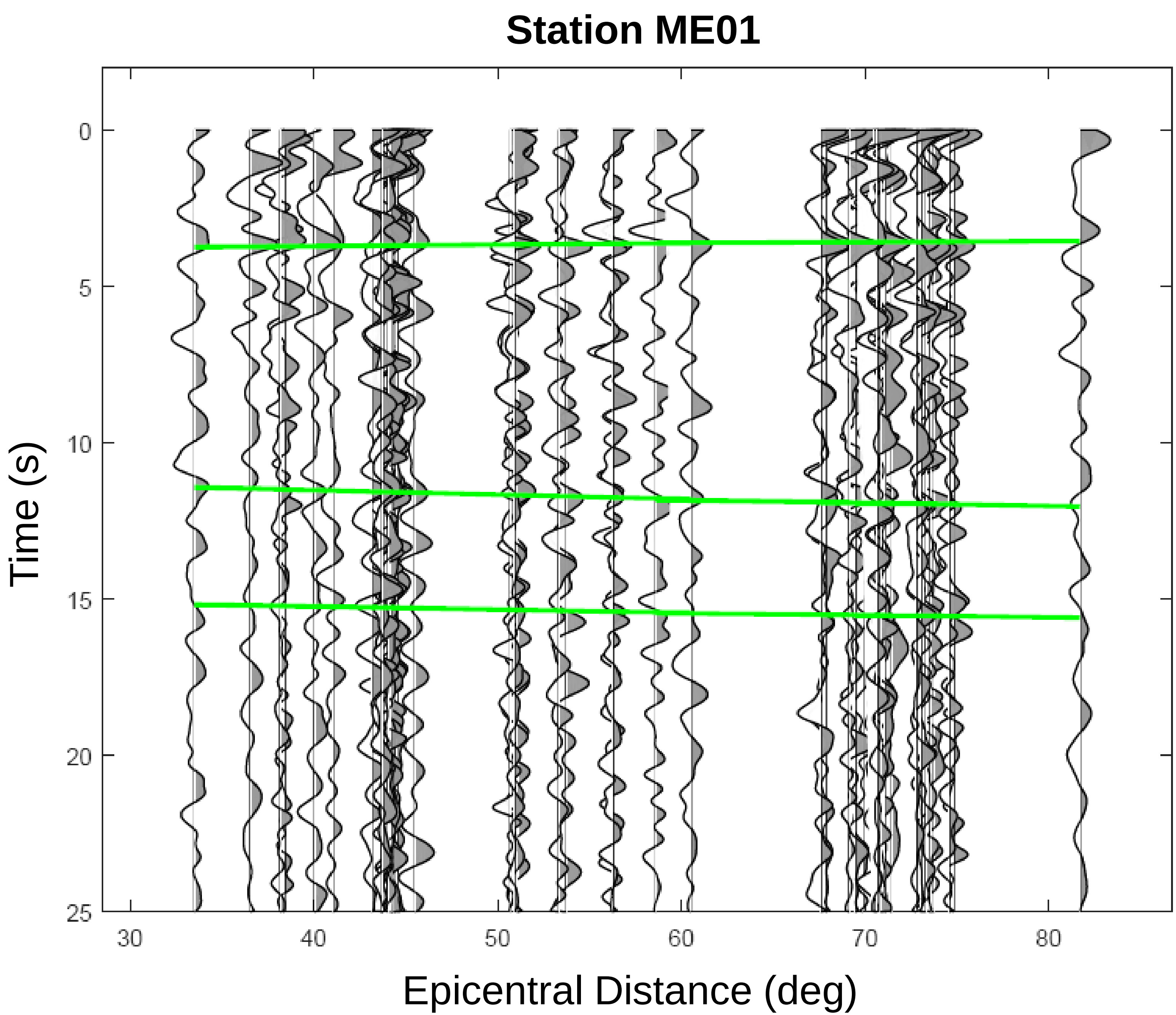
Station ME01
Time (s)
0
5
10
15
20
25
30
40
50
60
70
80
Epicentral Distance (deg)

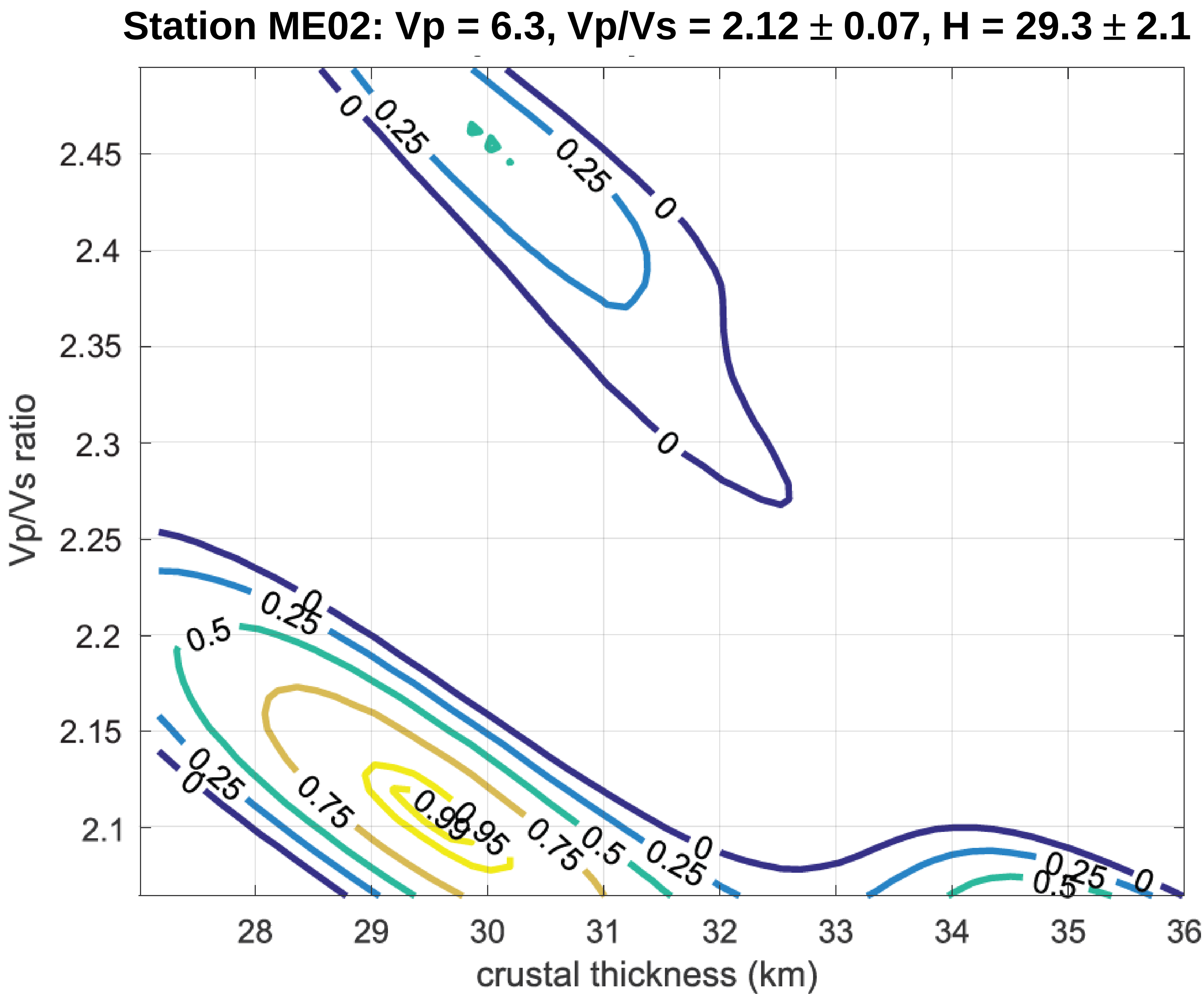
Station ME02: Vp = 6.3, Vp/Vs = 2.12 ± 0.07, H = 29.3 ± 2.1
Vp/Vs ratio
2.45
2.4
2.35
2.3
2.25
2.2
2.15
2.1
28
29
30
31
32
33
34
35
36
crustal thickness (km)
0
0.25
0.5
0.75
0.95
0.99

Station ME02

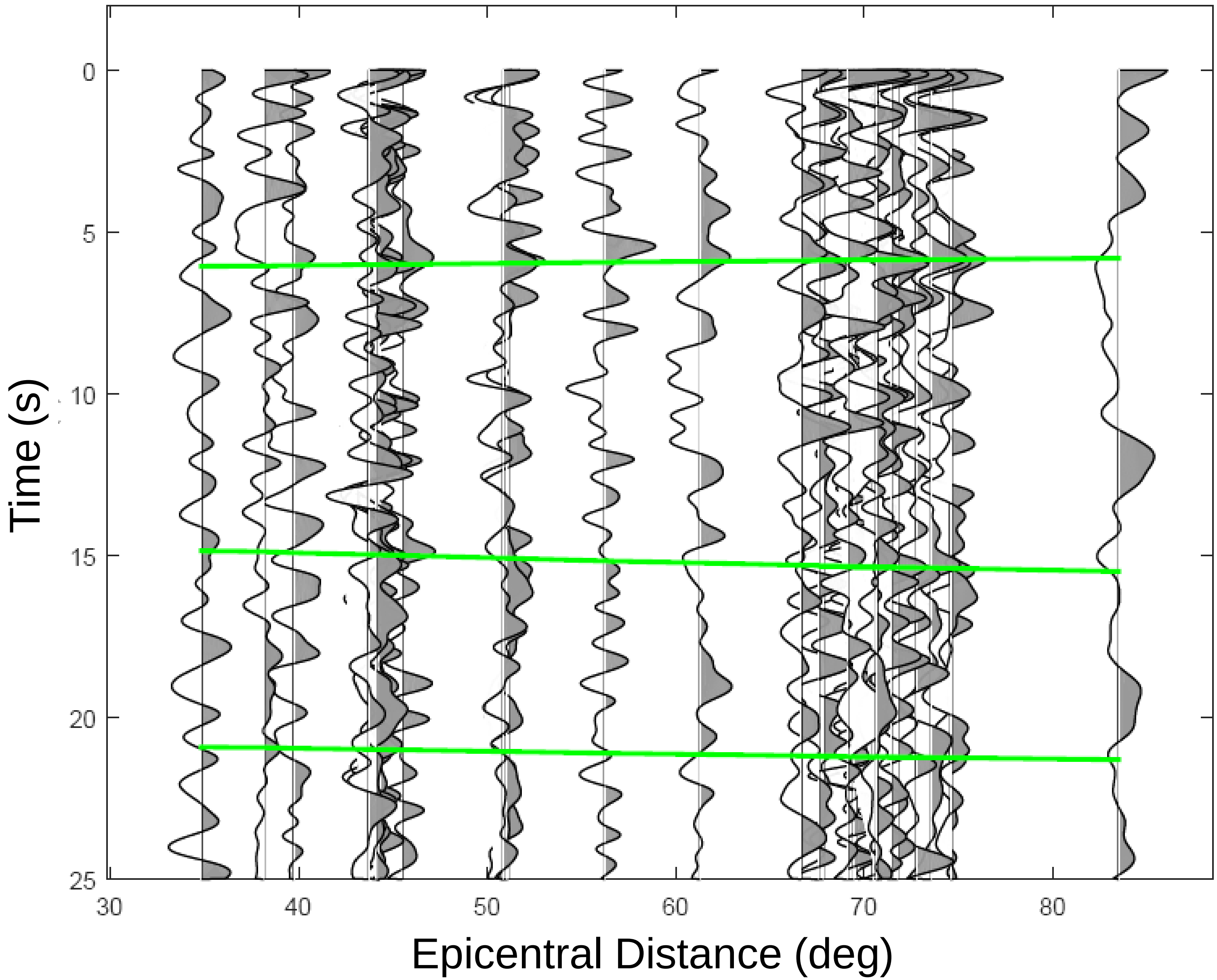

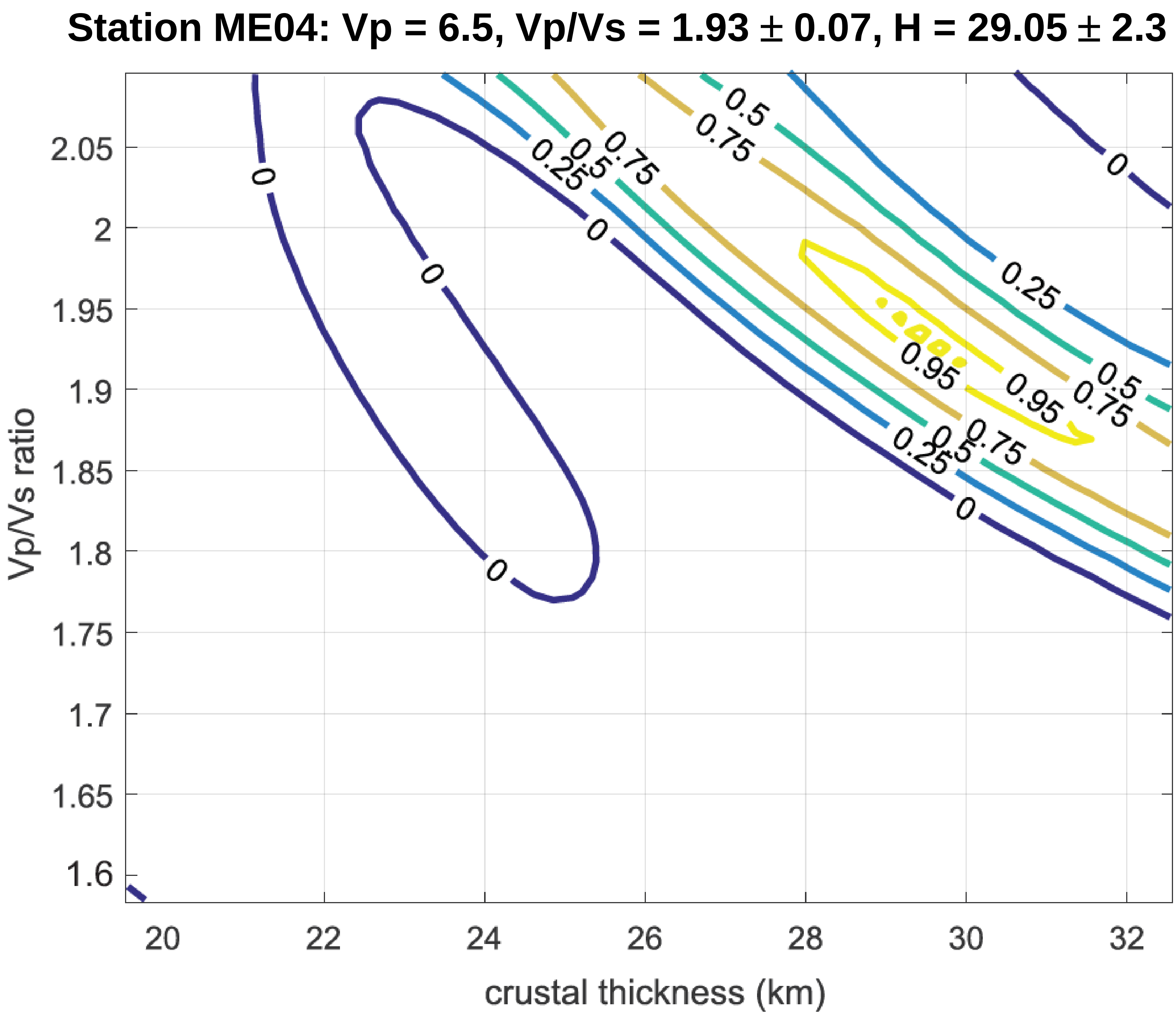

Station ME04: Vp = 6.5, Vp/Vs = 1.93 ± 0.07, H = 29.05 ± 2.3
Vp/Vs ratio
crustal thickness (km)
2.05
2
1.95
1.9
1.85
1.8
1.75
1.7
1.65
1.6
20
22
24
26
28
30
32
0
0.25
0.5
0.75
0.95

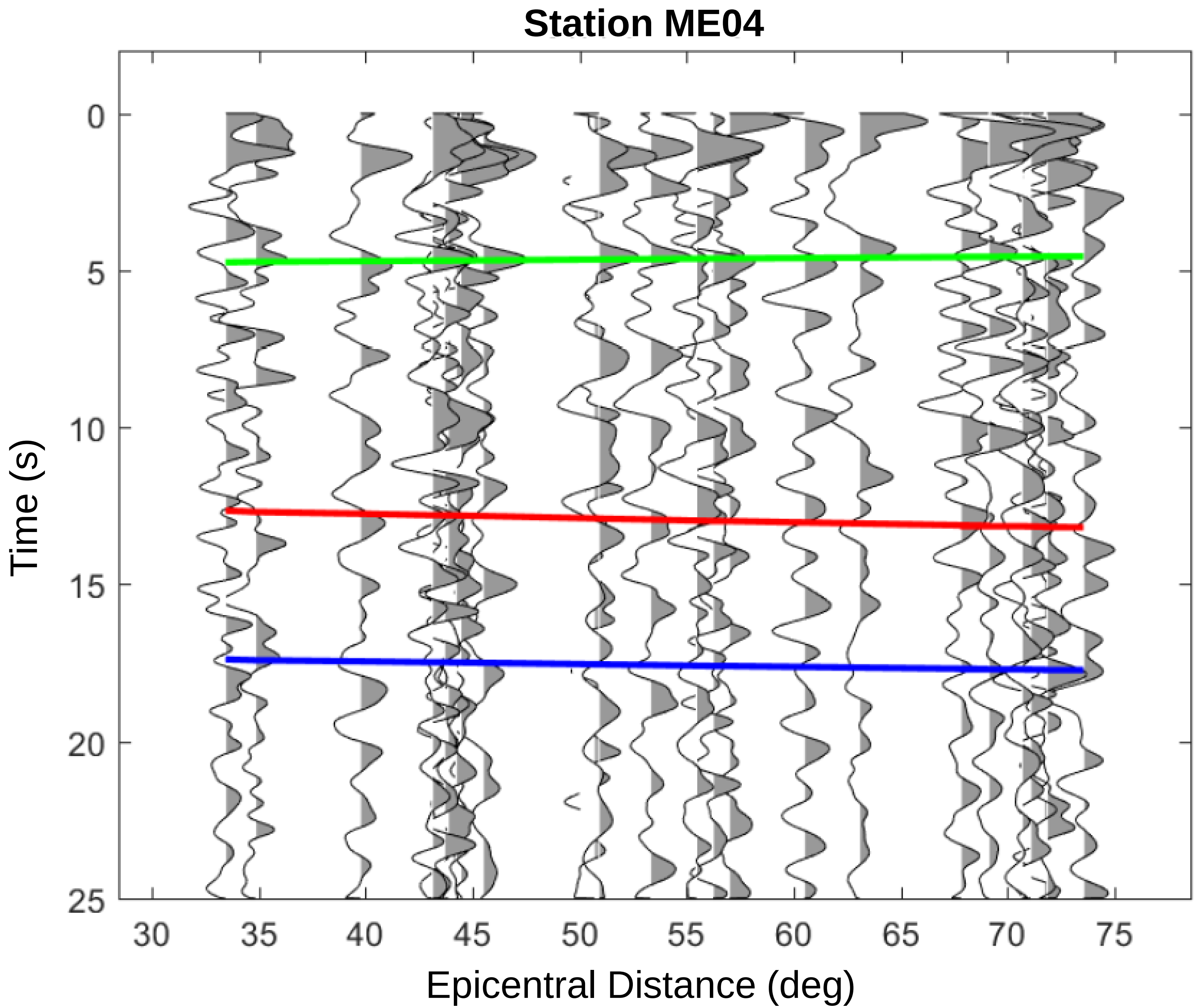
Station ME04
Time (s)
0
5
10
15
20
25
30
35
40
45
50
55
60
65
70
75
Epicentral Distance (deg)

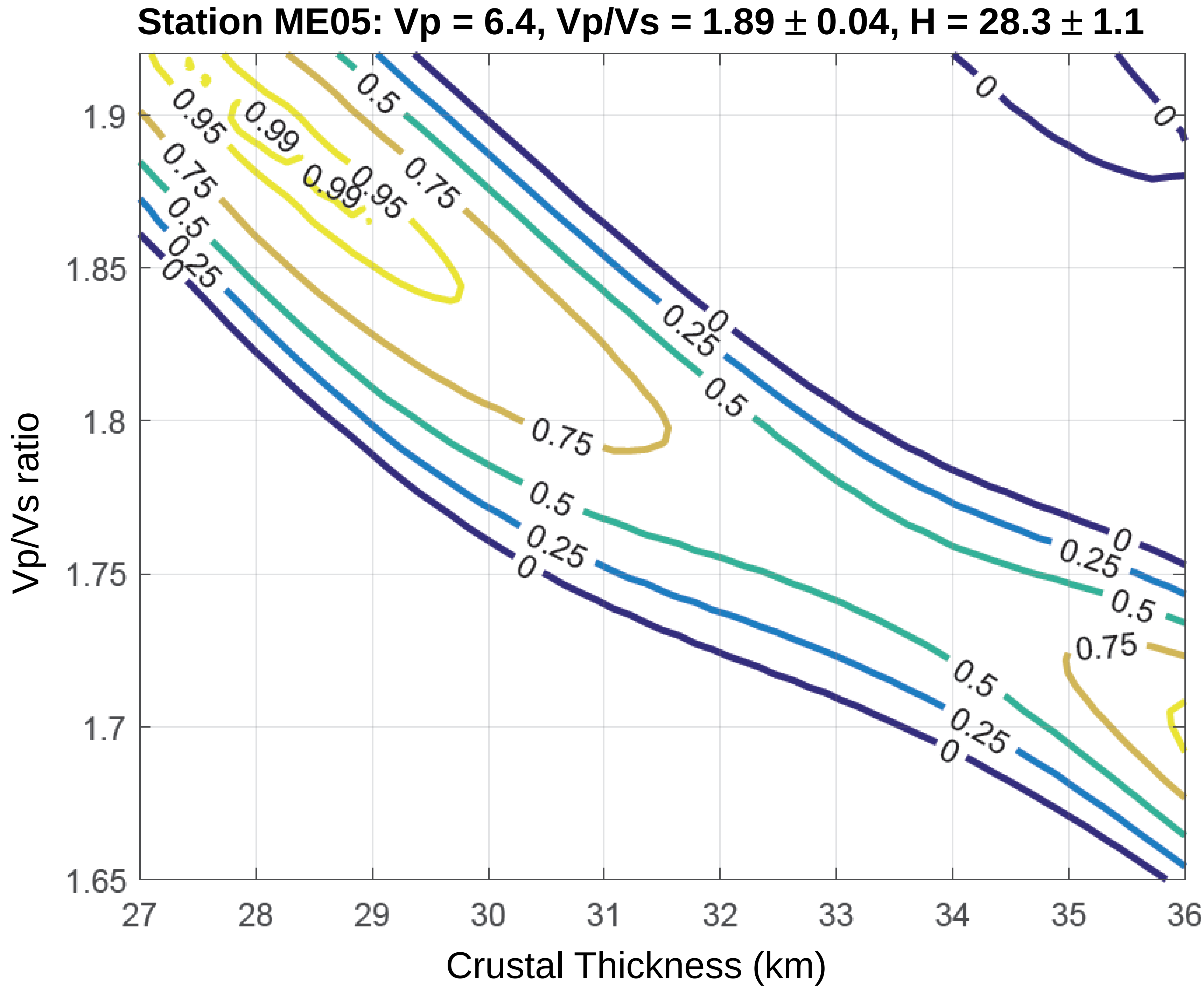

Station ME05: Vp = 6.4, Vp/Vs = 1.89 ± 0.04, H = 28.3 ± 1.1
Vp/Vs ratio
1.9
1.85
1.8
1.75
1.7
1.65
27
28
29
30
31
32
33
34
35
36
Crustal Thickness (km)
0.95
0.99
0.75
0.5
0.25
0
0.99
0.95
0.75
0.5
0.25
0
0.75
0.5
0.25
0
0.5
0.25
0
0.75

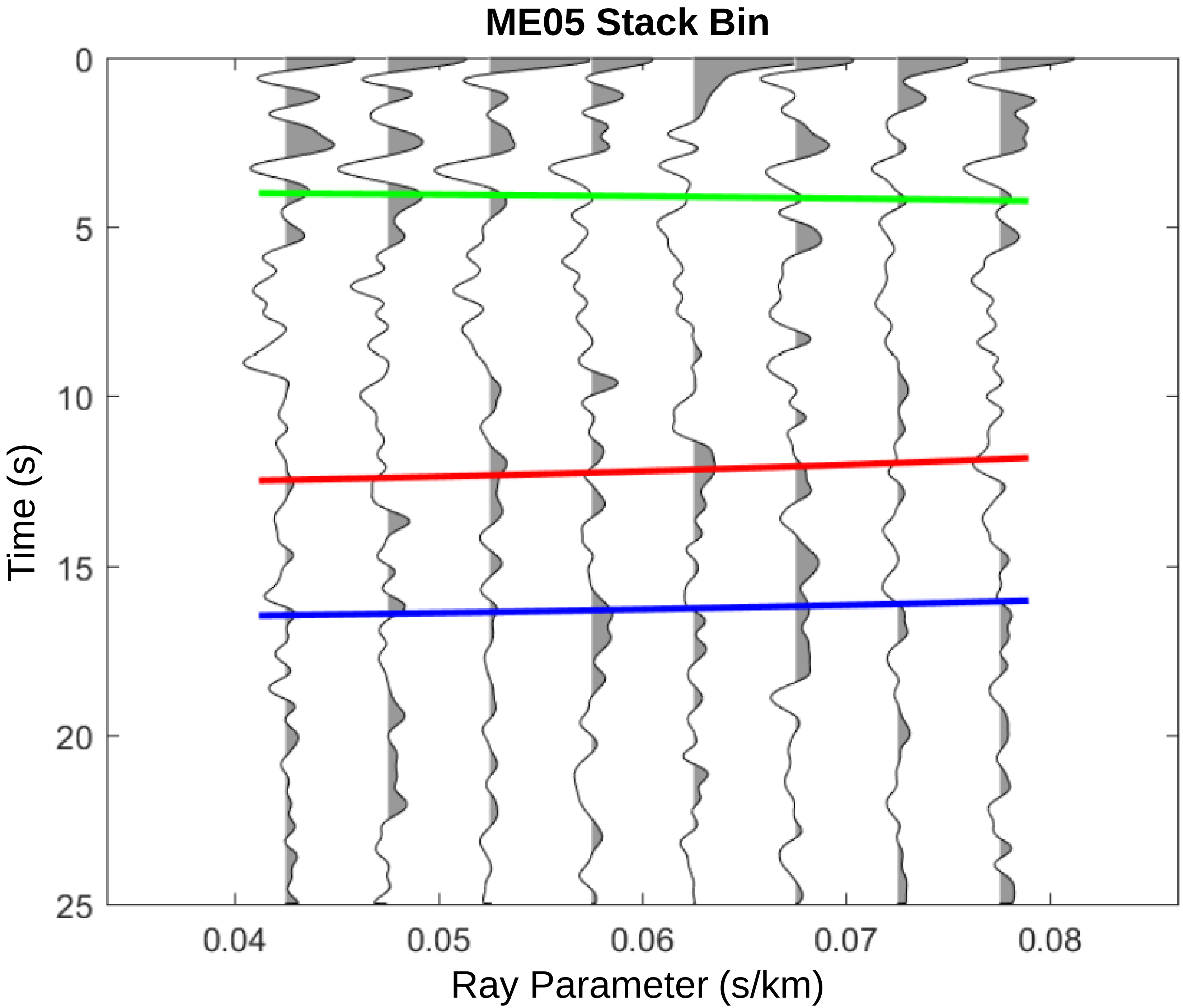

ME05 Stack Bin
Time (s)
0
5
10
15
20
25
0.04
0.05
0.06
0.07
0.08
Ray Parameter (s/km)

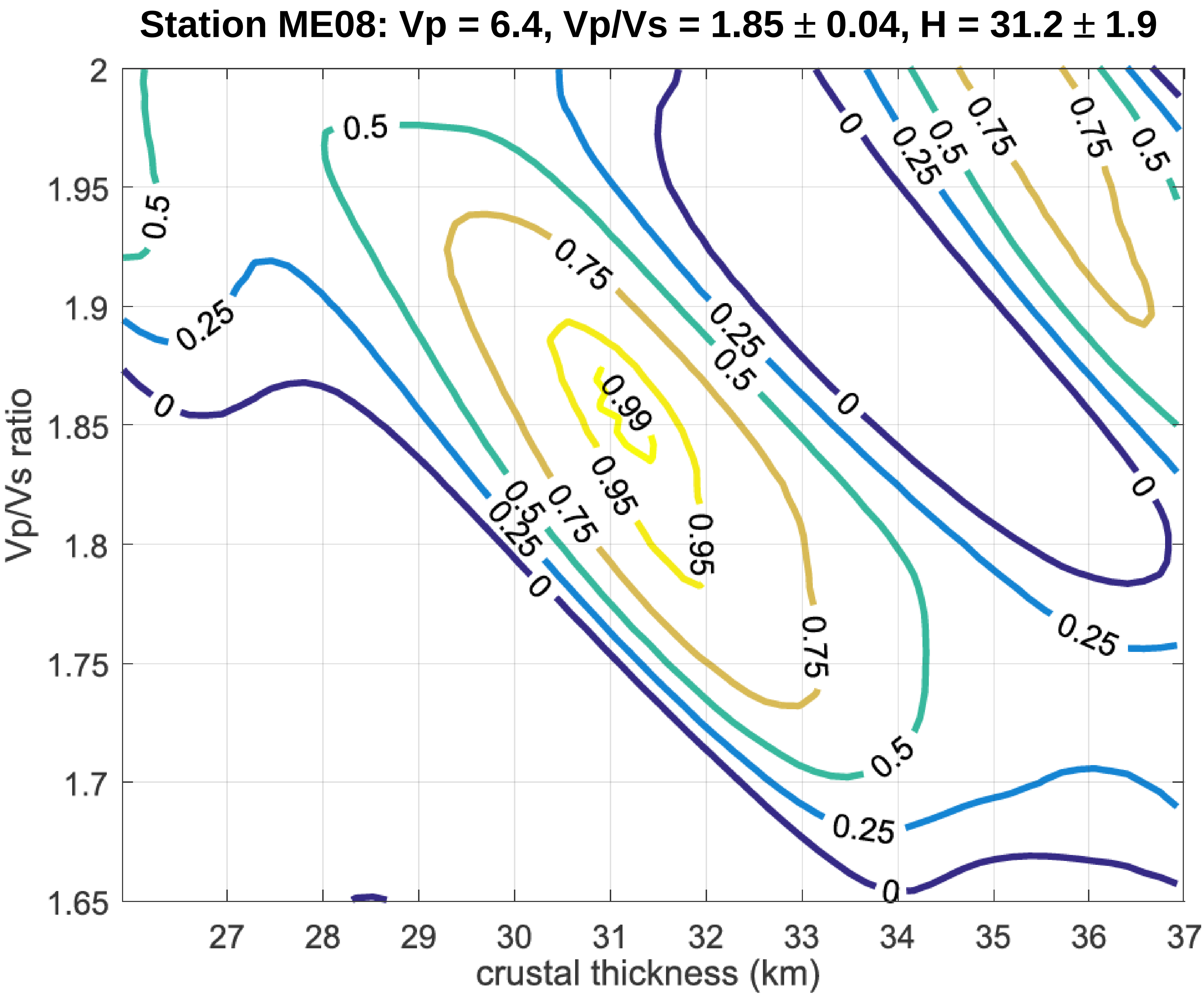

Station ME08: Vp = 6.4, Vp/Vs = 1.85 ± 0.04, H = 31.2 ± 1.9
Vp/Vs ratio
crustal thickness (km)
2
1.95
1.9
1.85
1.8
1.75
1.7
1.65
27
28
29
30
31
32
33
34
35
36
37
0
0.25
0.5
0.75
0.95
0.99

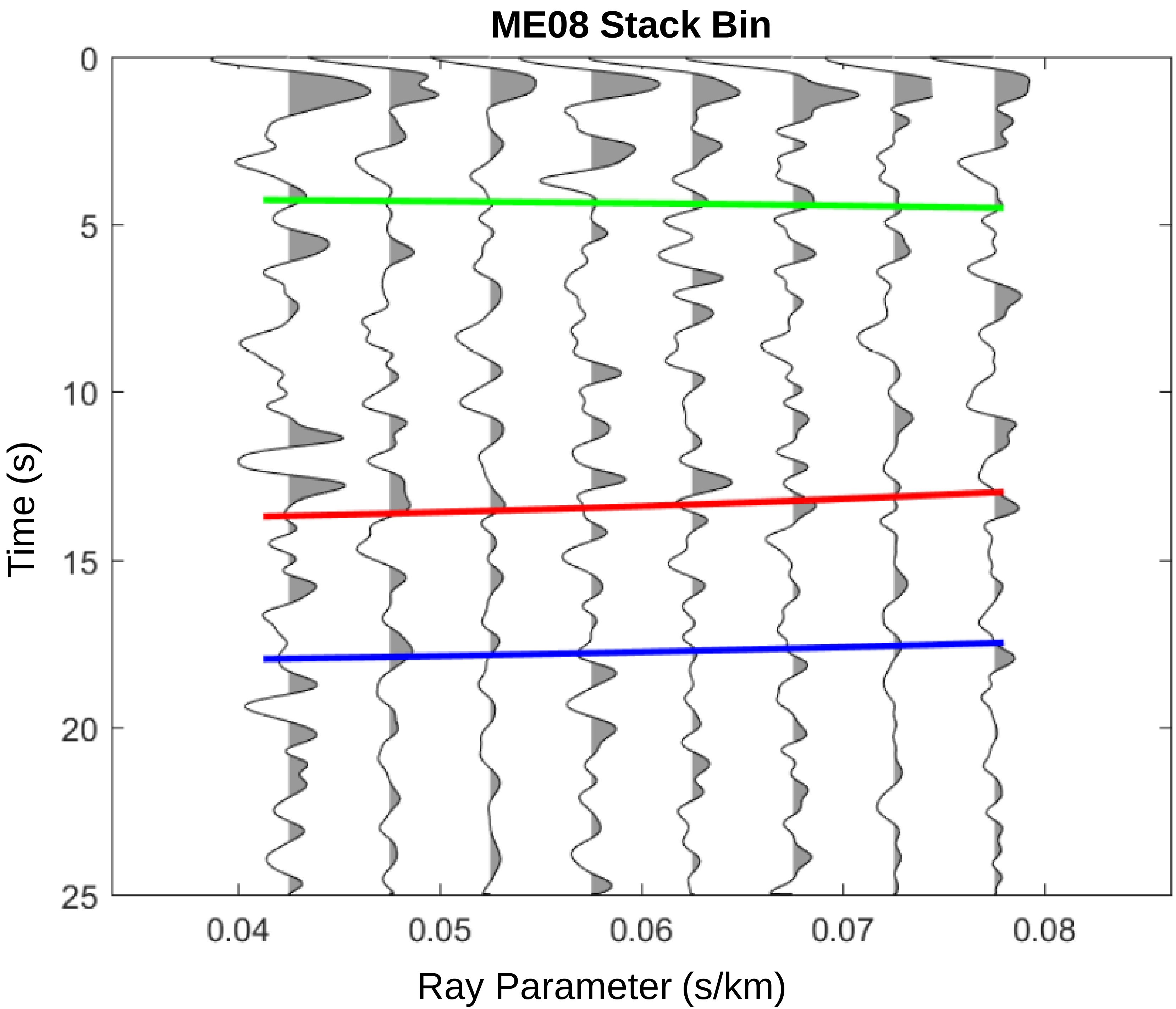
ME08 Stack Bin
Time (s)
0
5
10
15
20
25
0.04
0.05
0.06
0.07
0.08
Ray Parameter (s/km)

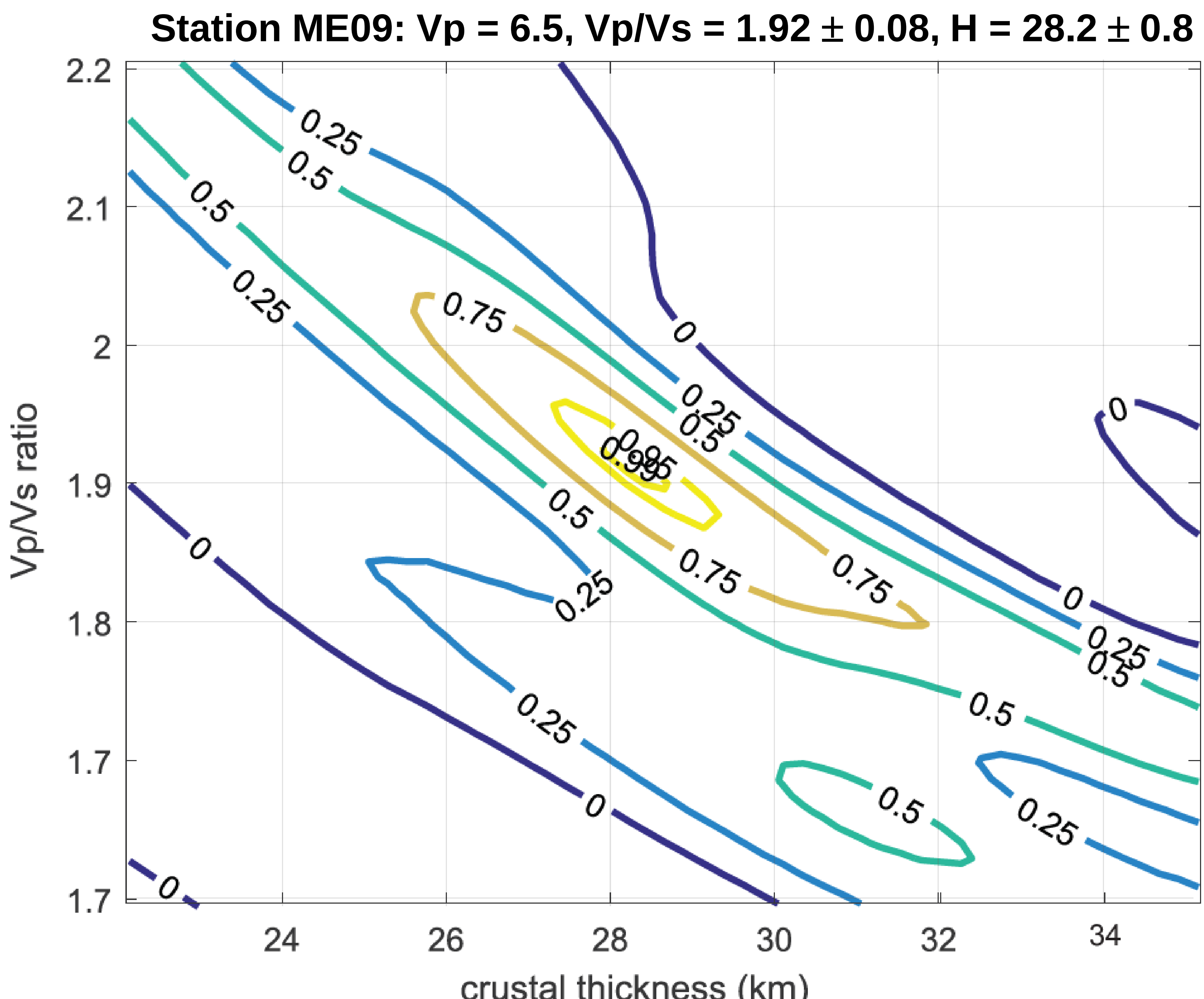

Station ME09: Vp = 6.5, Vp/Vs = 1.92 ± 0.08, H = 28.2 ± 0.8
Vp/Vs ratio
crustal thickness (km)
2.2
2.1
2
1.9
1.8
1.7
1.7
24
26
28
30
32
34
0
0.25
0.5
0.75
0.95
0.99

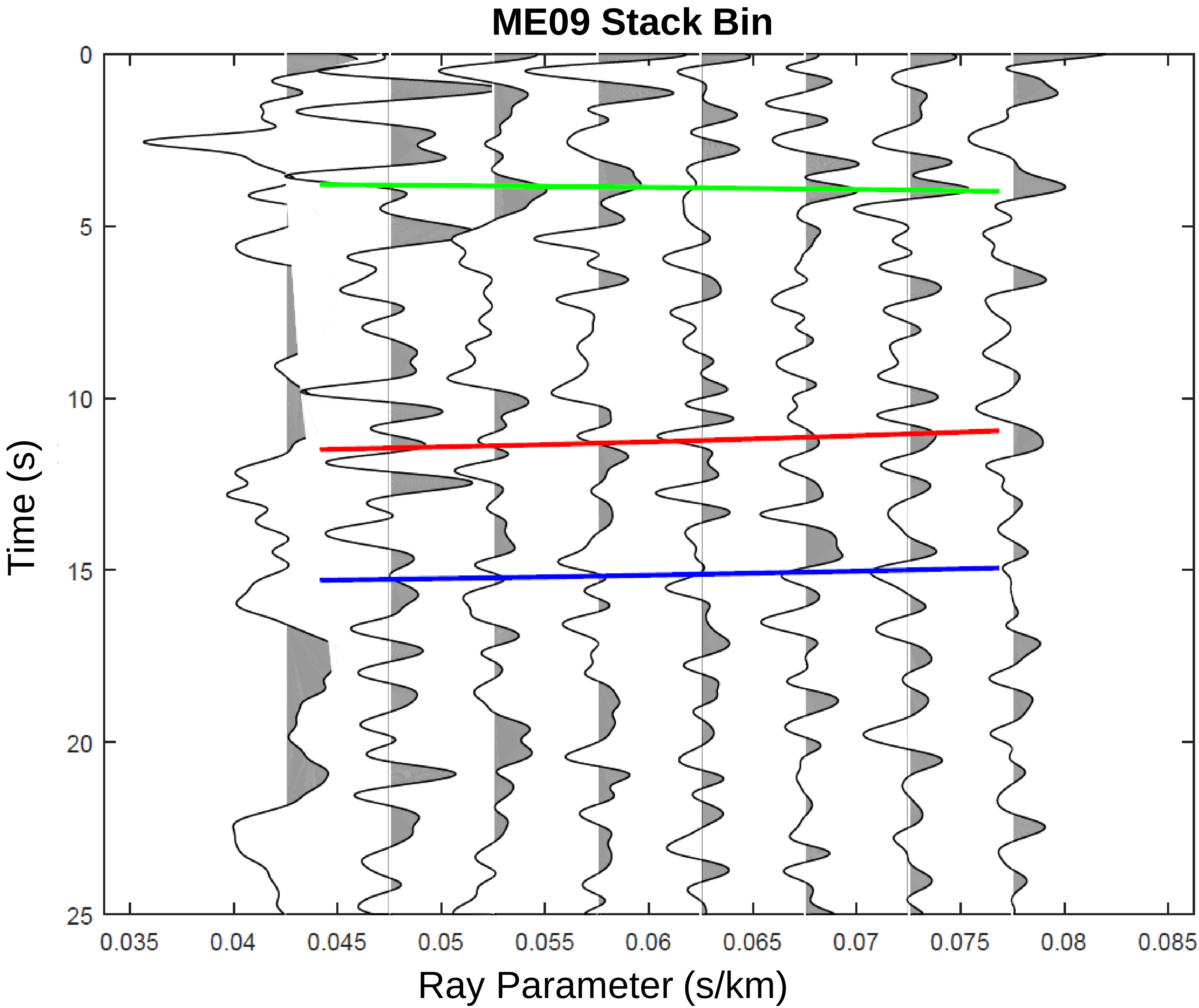

ME09 Stack Bin
Time (s)
0
5
10
15
20
25
0.035
0.04
0.045
0.05
0.055
0.06
0.065
0.07
0.075
0.08
0.085
Ray Parameter (s/km)

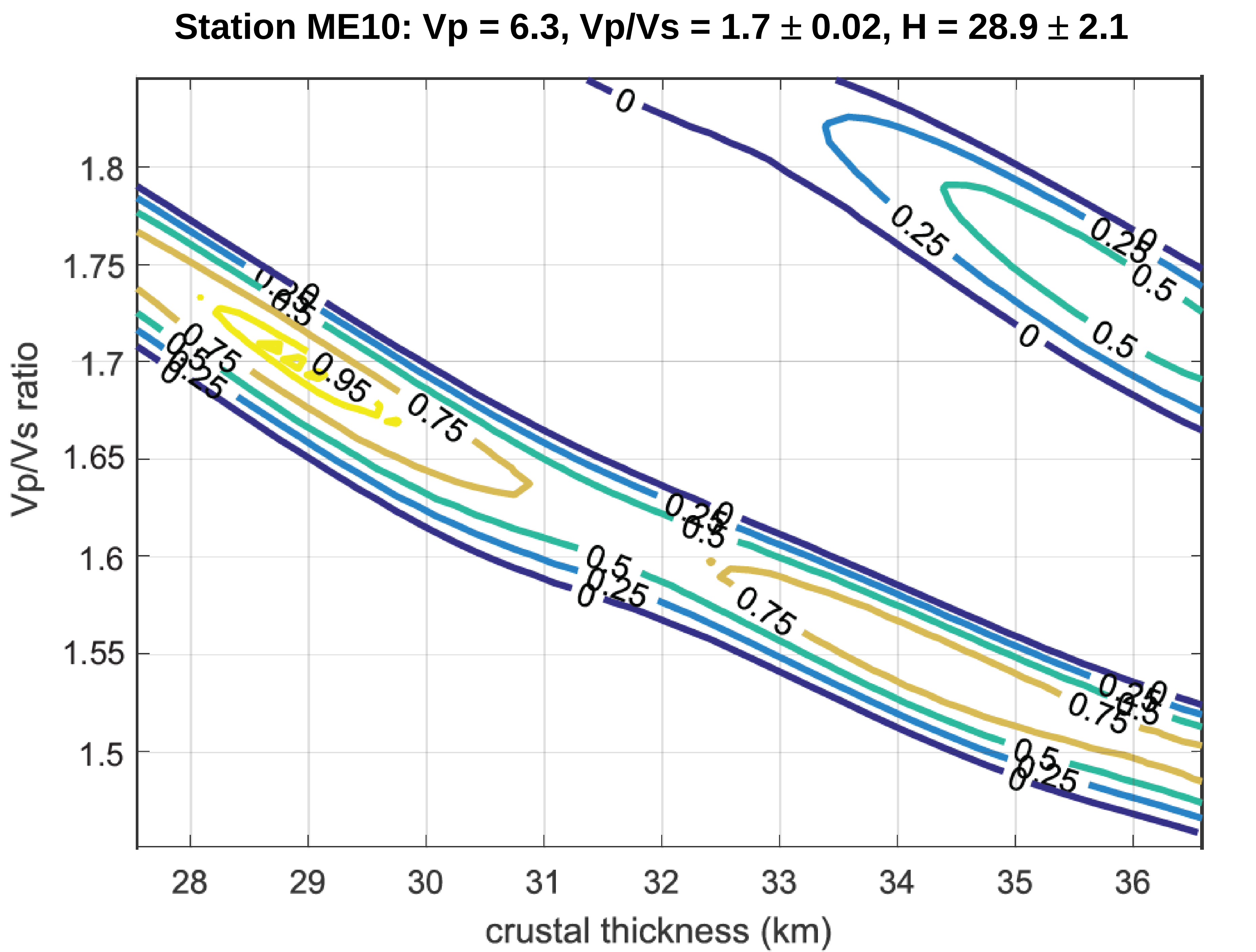

Station ME10: Vp = 6.3, Vp/Vs = 1.7 ± 0.02, H = 28.9 ± 2.1
Vp/Vs ratio
1.8
1.75
1.7
1.65
1.6
1.55
1.5
28
29
30
31
32
33
34
35
36
crustal thickness (km)
0
0.25
0.5
0.75
0.95

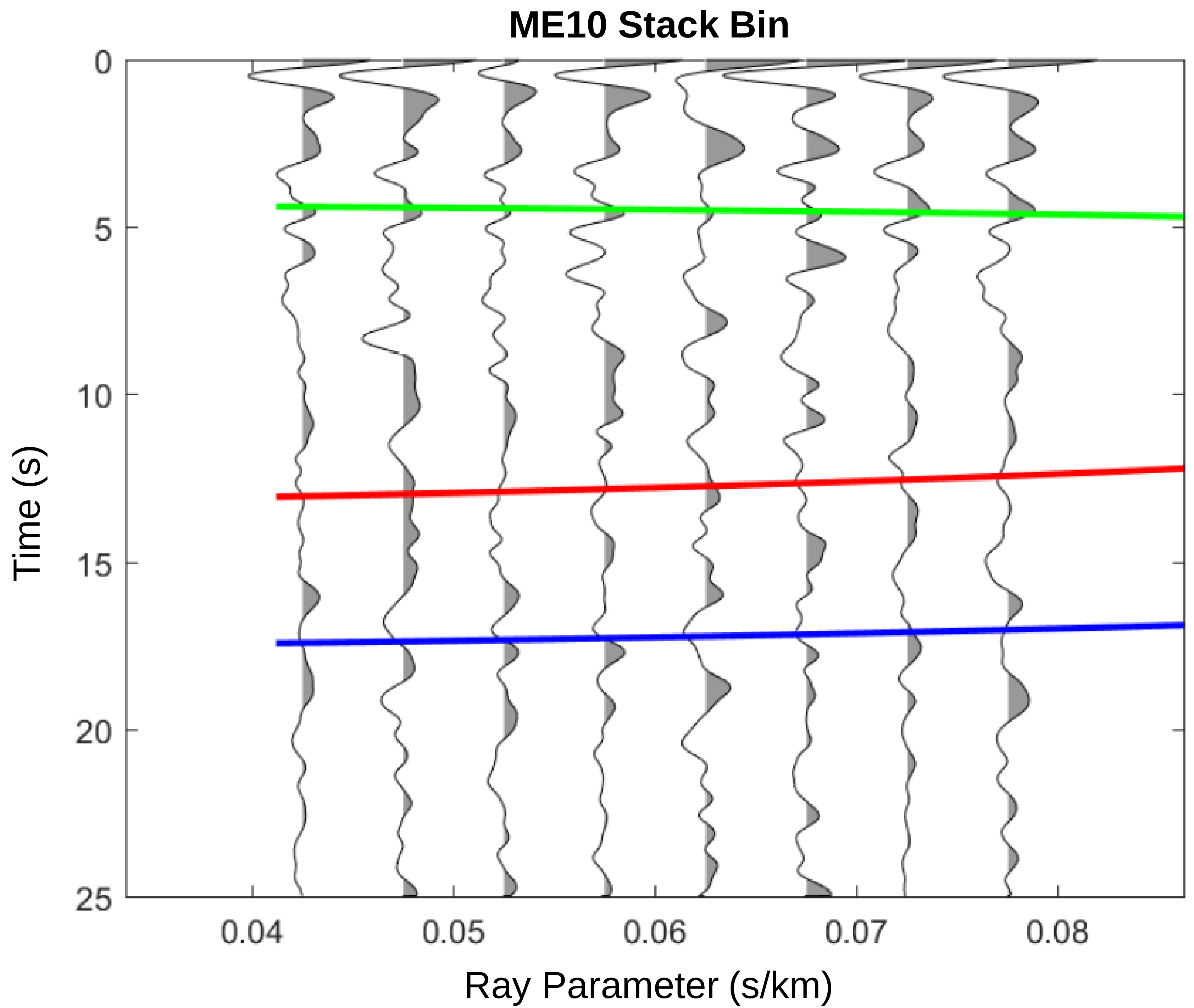

ME10 Stack Bin
Time (s)
0
5
10
15
20
25
0.04
0.05
0.06
0.07
0.08
Ray Parameter (s/km)

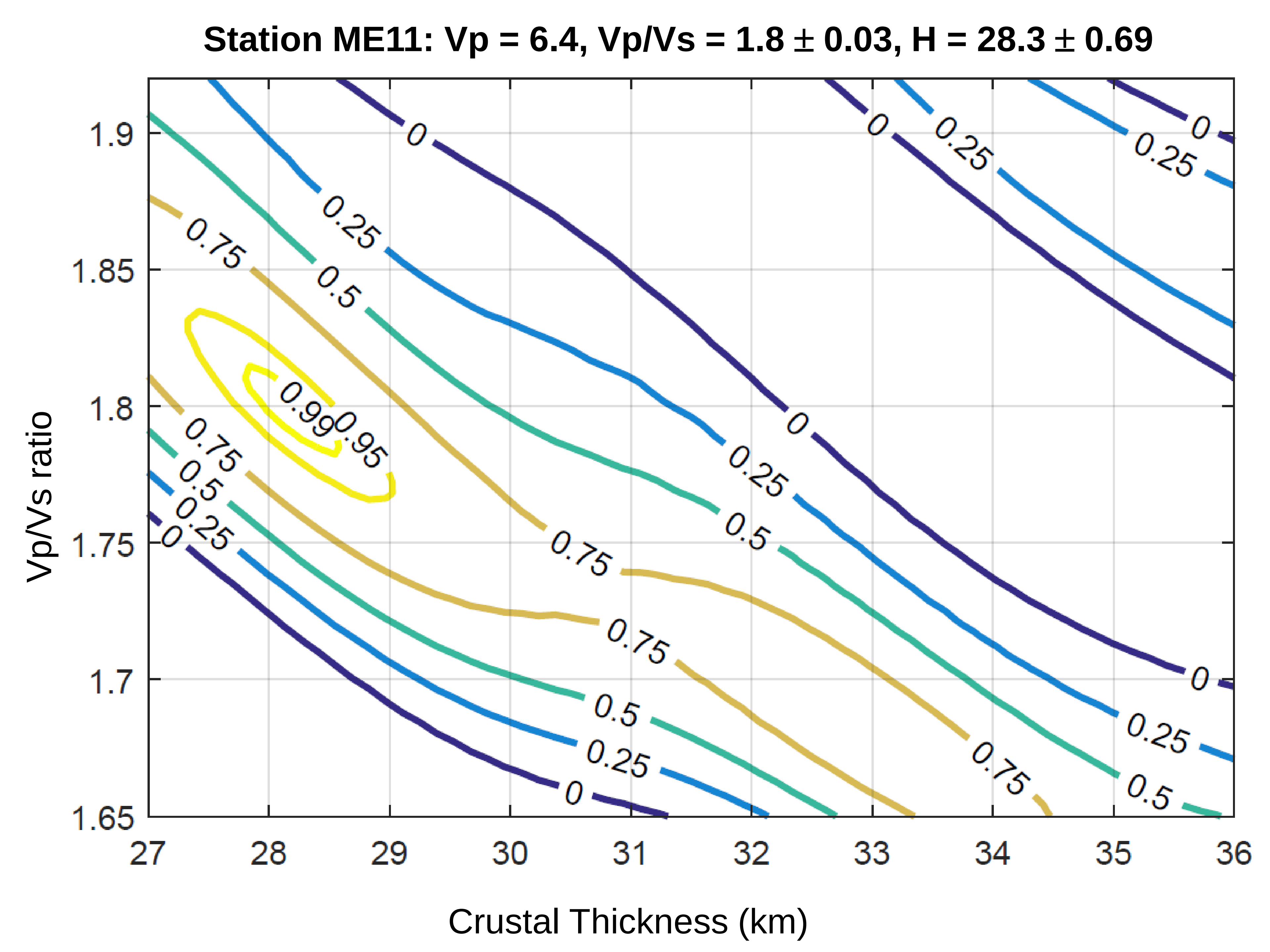

Station ME11: Vp = 6.4, Vp/Vs = 1.8 ± 0.03, H = 28.3 ± 0.69
Vp/Vs ratio
Crustal Thickness (km)
1.9
1.85
1.8
1.75
1.7
1.65
27
28
29
30
31
32
33
34
35
36
0
0.25
0.5
0.75
0.95
0.99

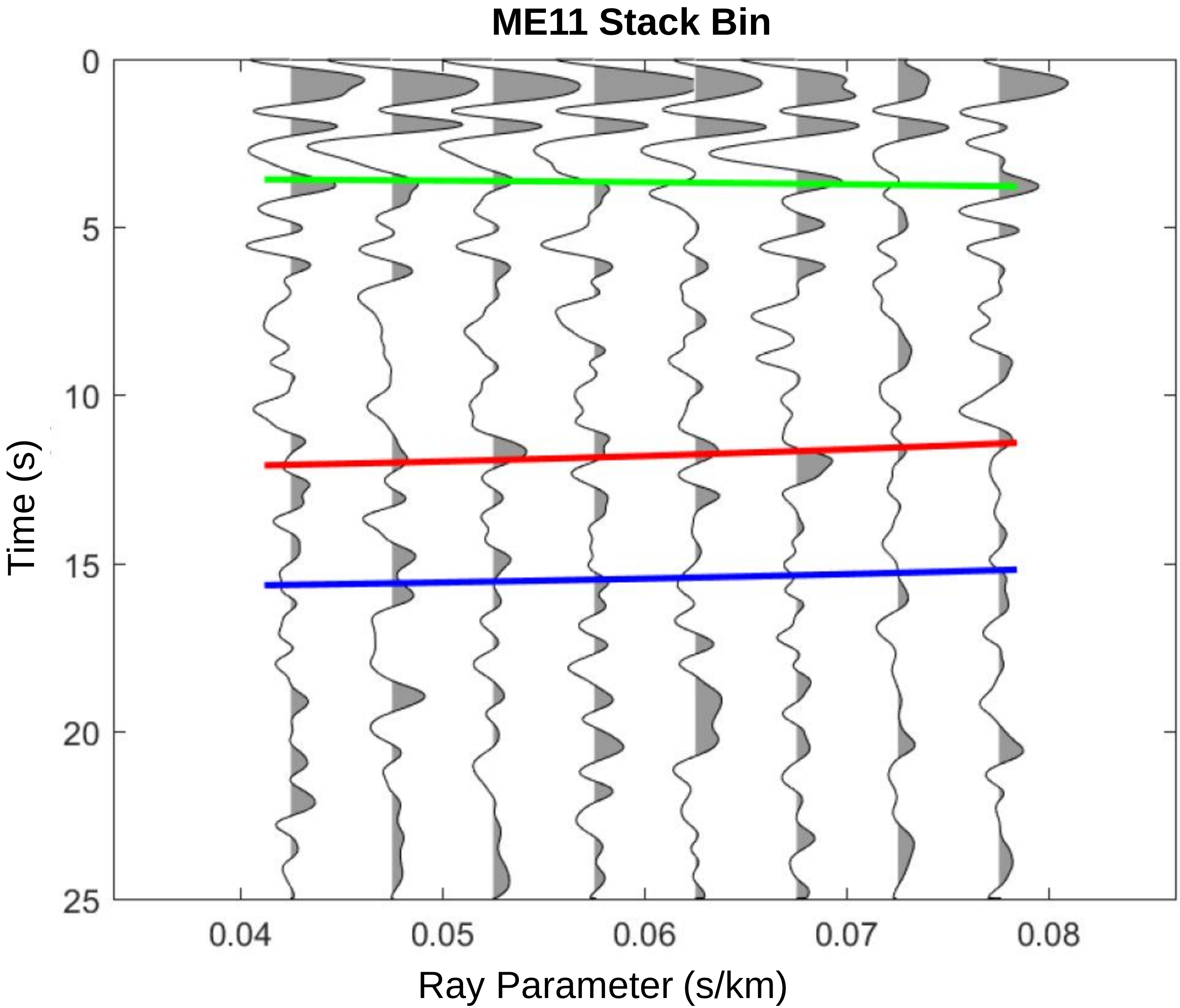
ME11 Stack Bin
Time (s)
0
5
10
15
20
25
0.04
0.05
0.06
0.07
0.08
Ray Parameter (s/km)

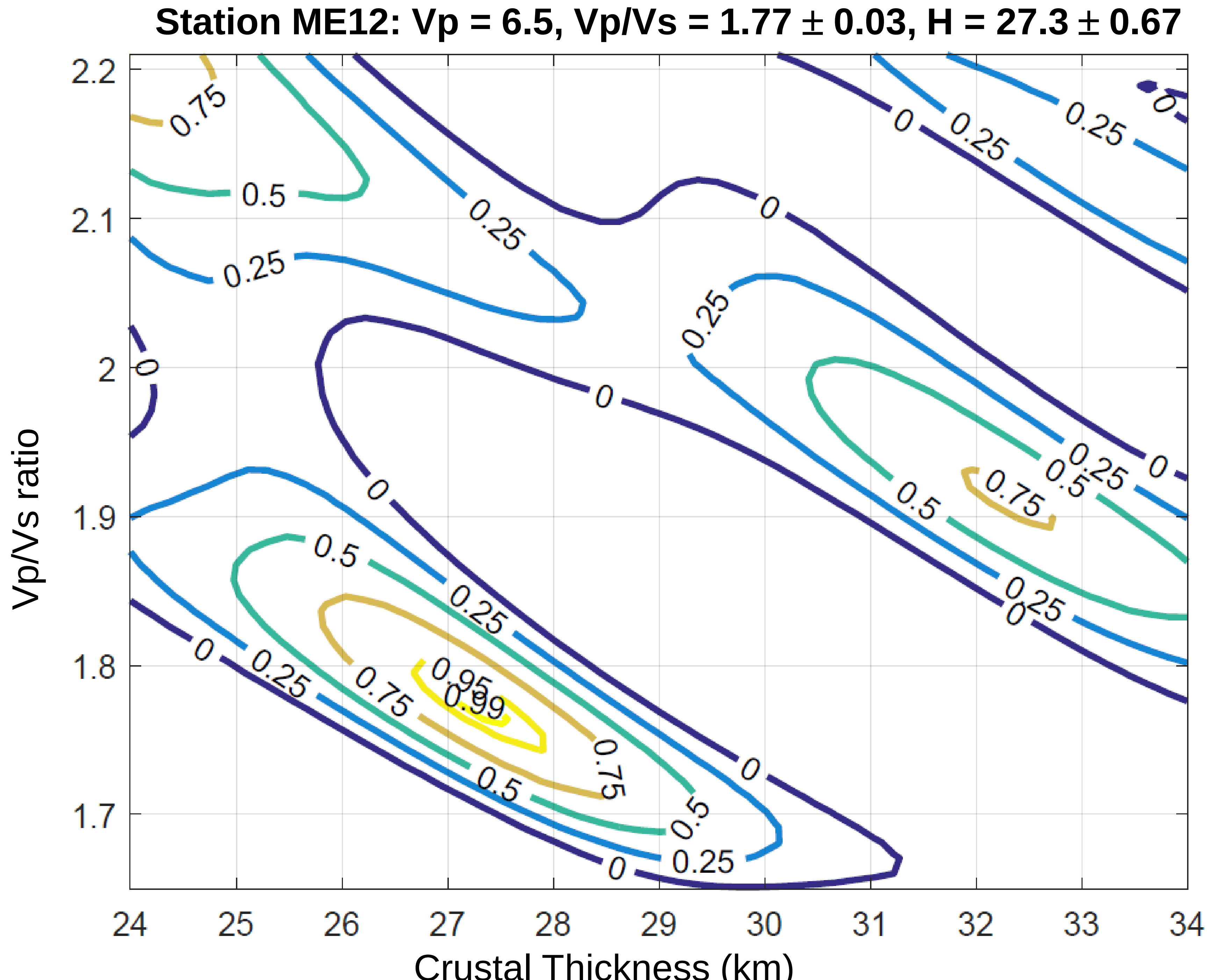

Station ME12: Vp = 6.5, Vp/Vs = 1.77 ± 0.03, H = 27.3 ± 0.67
Vp/Vs ratio
Crustal Thickness (km)
2.2
2.1
2
1.9
1.8
1.7
24
25
26
27
28
29
30
31
32
33
34
0
0.25
0.5
0.75
0.95
0.99

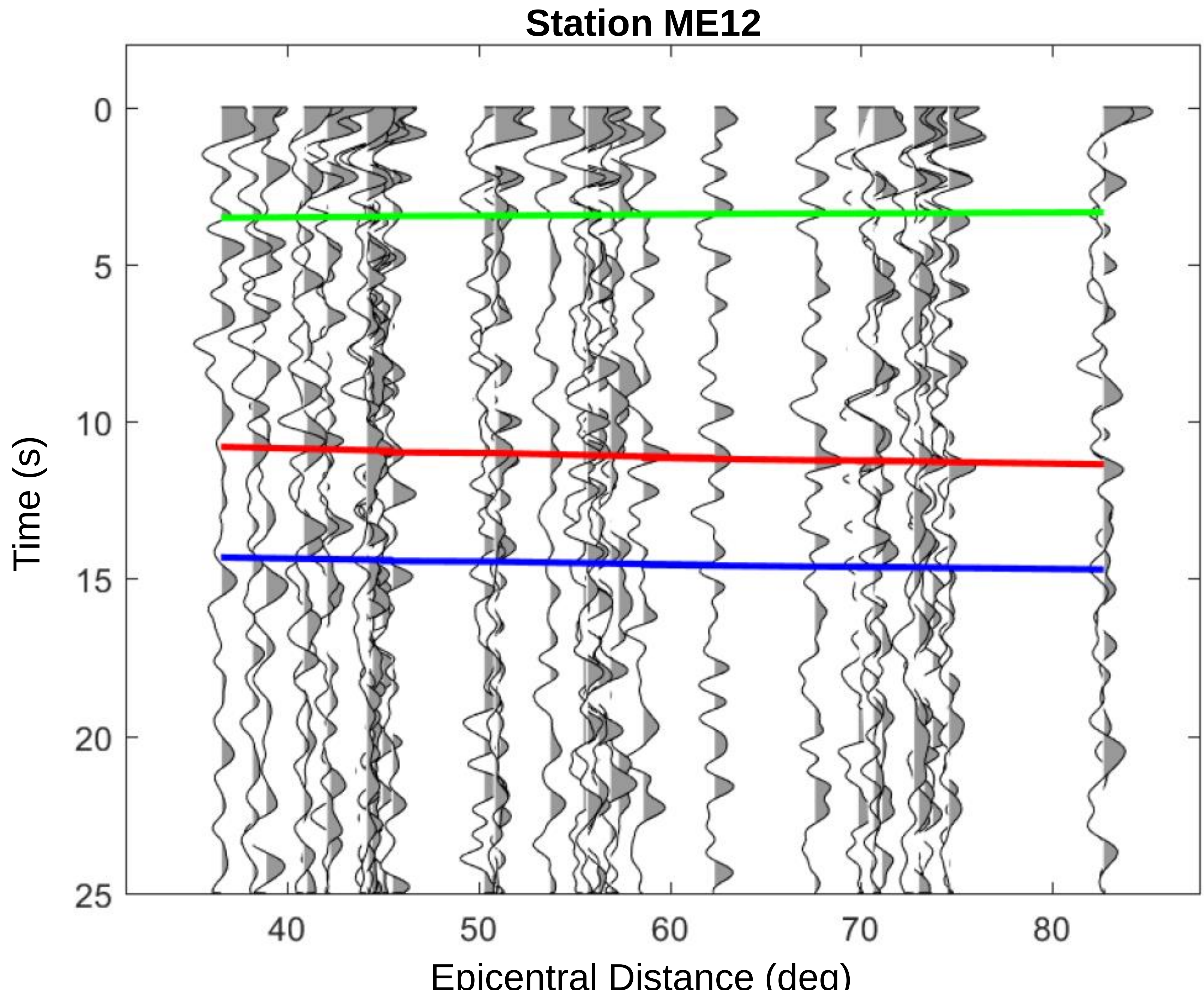

Station ME12
0
5
10
15
20
25
Time (s)
40
50
60
70
80
Epicentral Distance (deg)

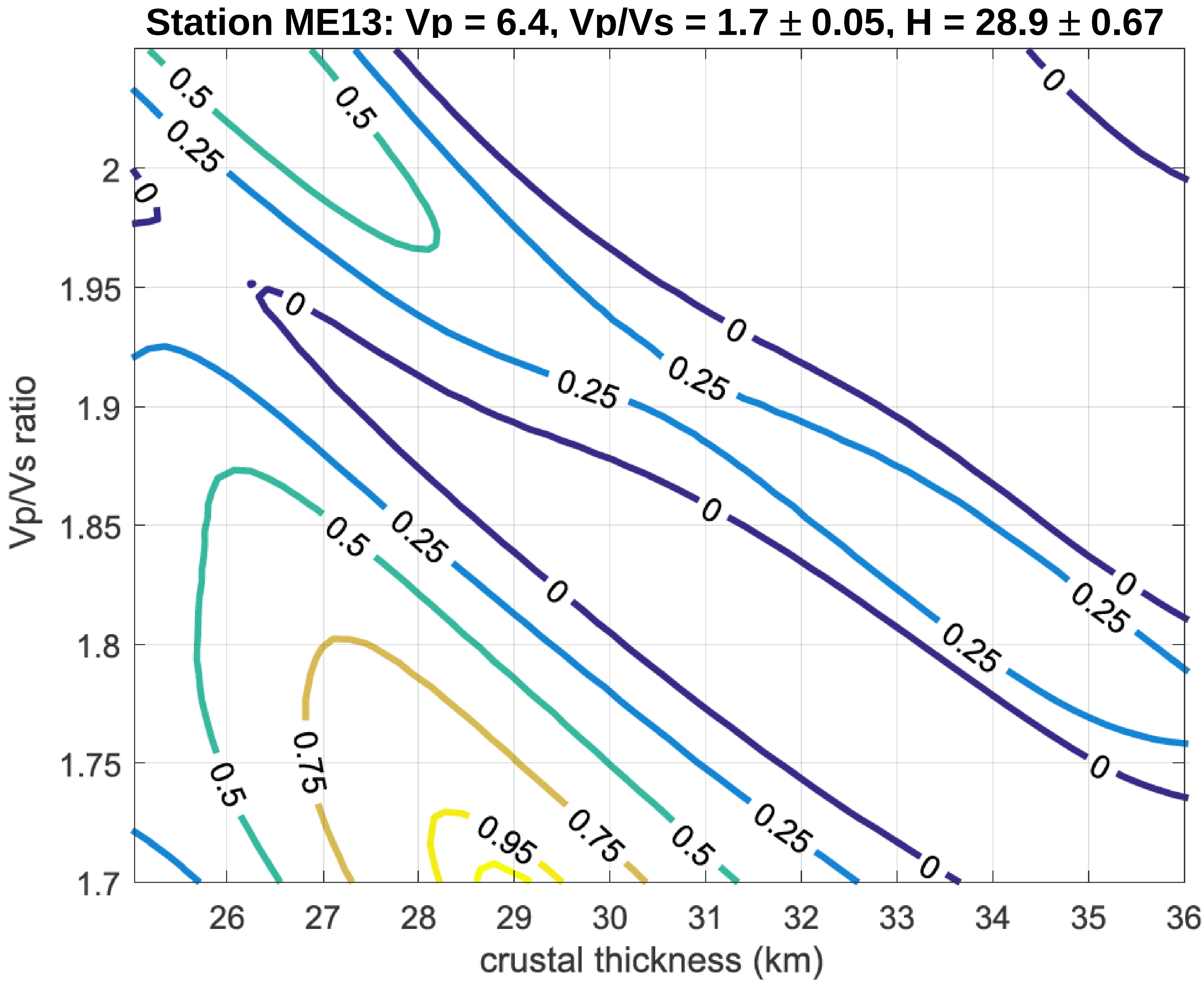
Station ME13: Vp = 6.4, Vp/Vs = 1.7 ± 0.05, H = 28.9 ± 0.67
Vp/Vs ratio
crustal thickness (km)
2
1.95
1.9
1.85
1.8
1.75
1.7
26
27
28
29
30
31
32
33
34
35
36
0
0.25
0.5
0.75
0.95

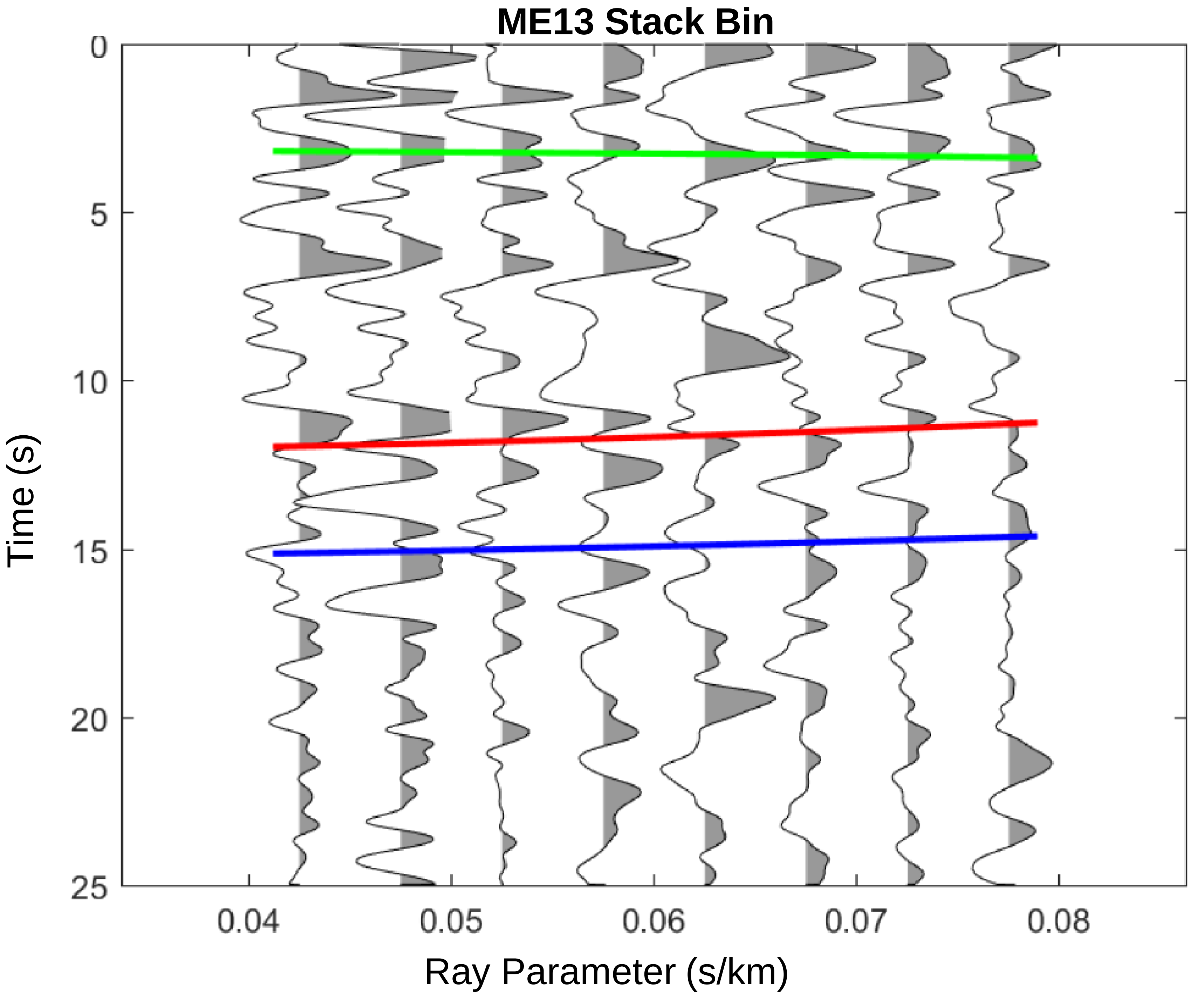
ME13 Stack Bin
Time (s)
0
5
10
15
20
25
0.04
0.05
0.06
0.07
0.08
Ray Parameter (s/km)

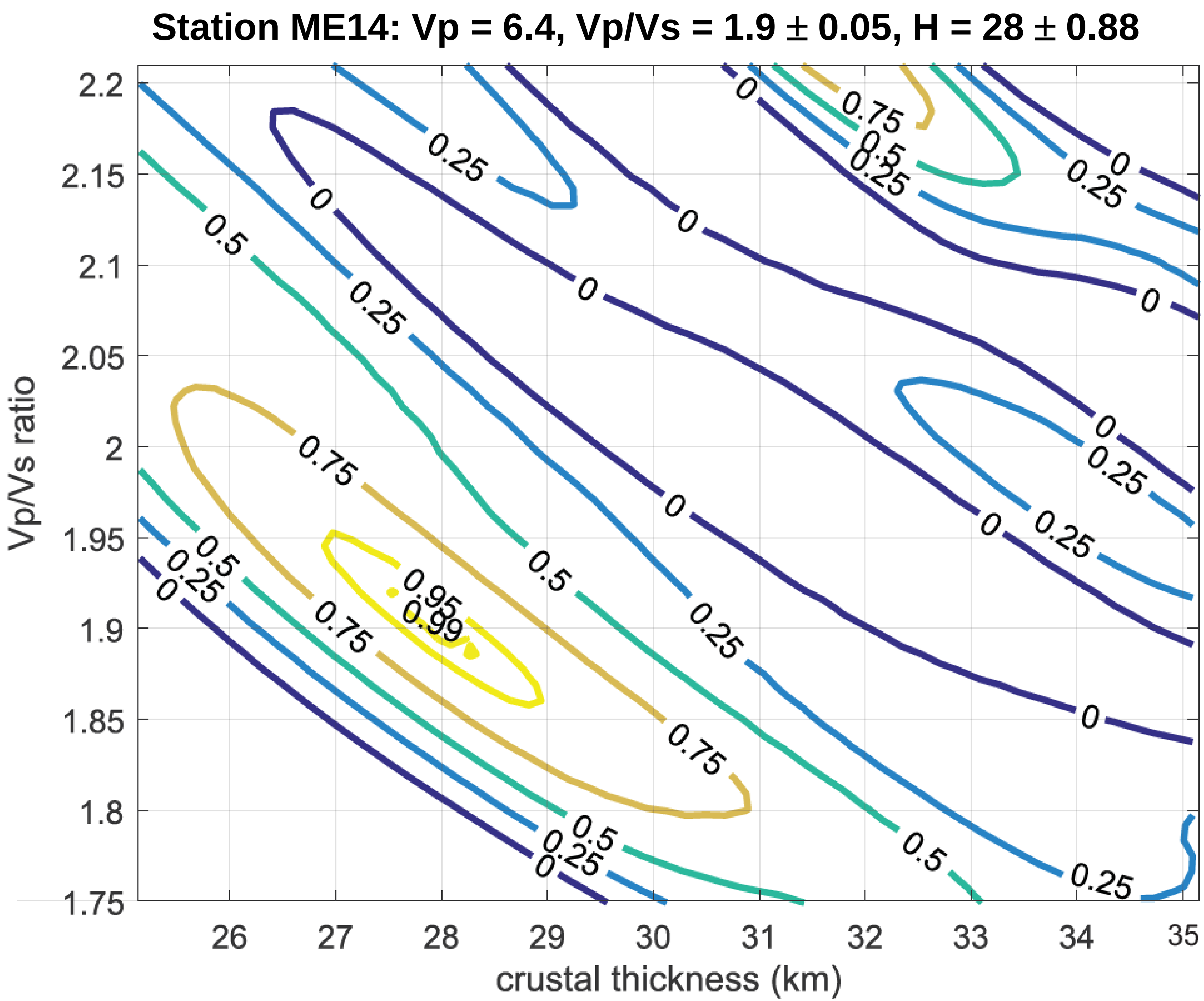

Station ME14: Vp = 6.4, Vp/Vs = 1.9 ± 0.05, H = 28 ± 0.88
Vp/Vs ratio
crustal thickness (km)
2.2
2.15
2.1
2.05
2
1.95
1.9
1.85
1.8
1.75
26
27
28
29
30
31
32
33
34
35
0
0.25
0.5
0.75
0.95
0.99

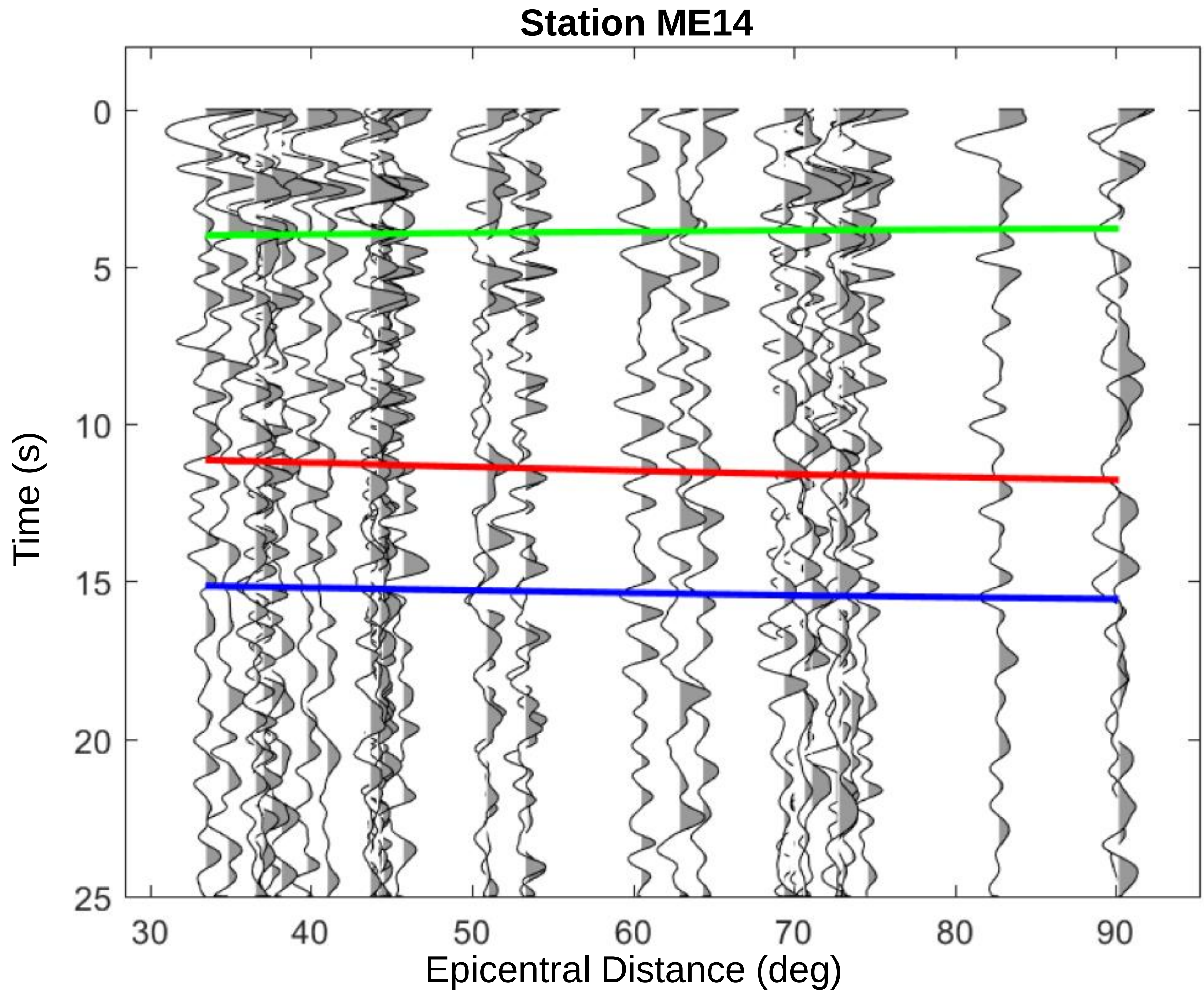

Station ME14
Time (s)
0
5
10
15
20
25
30
40
50
60
70
80
90
Epicentral Distance (deg)

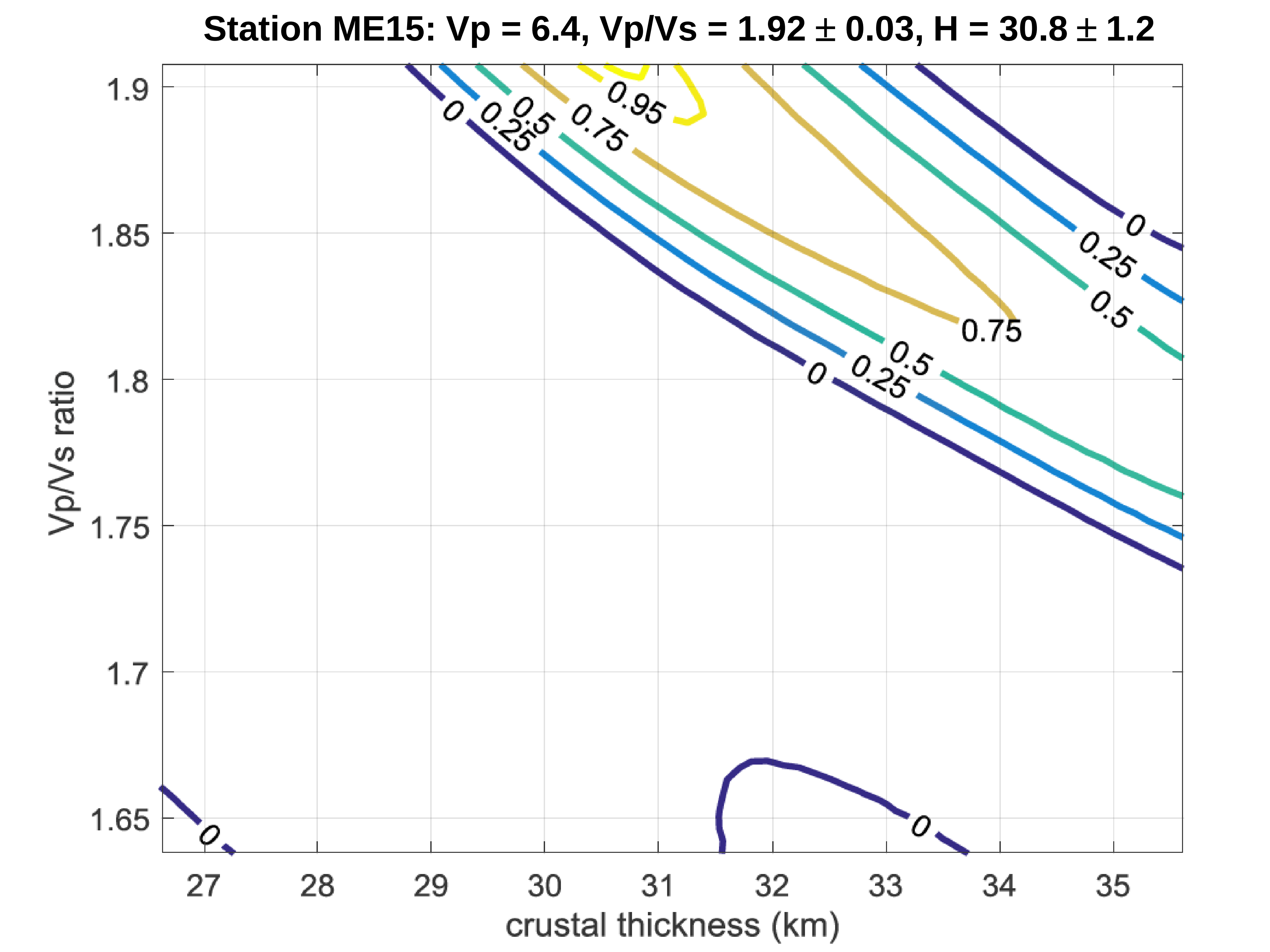
Station ME15: Vp = 6.4, Vp/Vs = 1.92 ± 0.03, H = 30.8 ± 1.2
Vp/Vs ratio
crustal thickness (km)
1.9
1.85
1.8
1.75
1.7
1.65
27
28
29
30
31
32
33
34
35
0
0.25
0.5
0.75
0.95

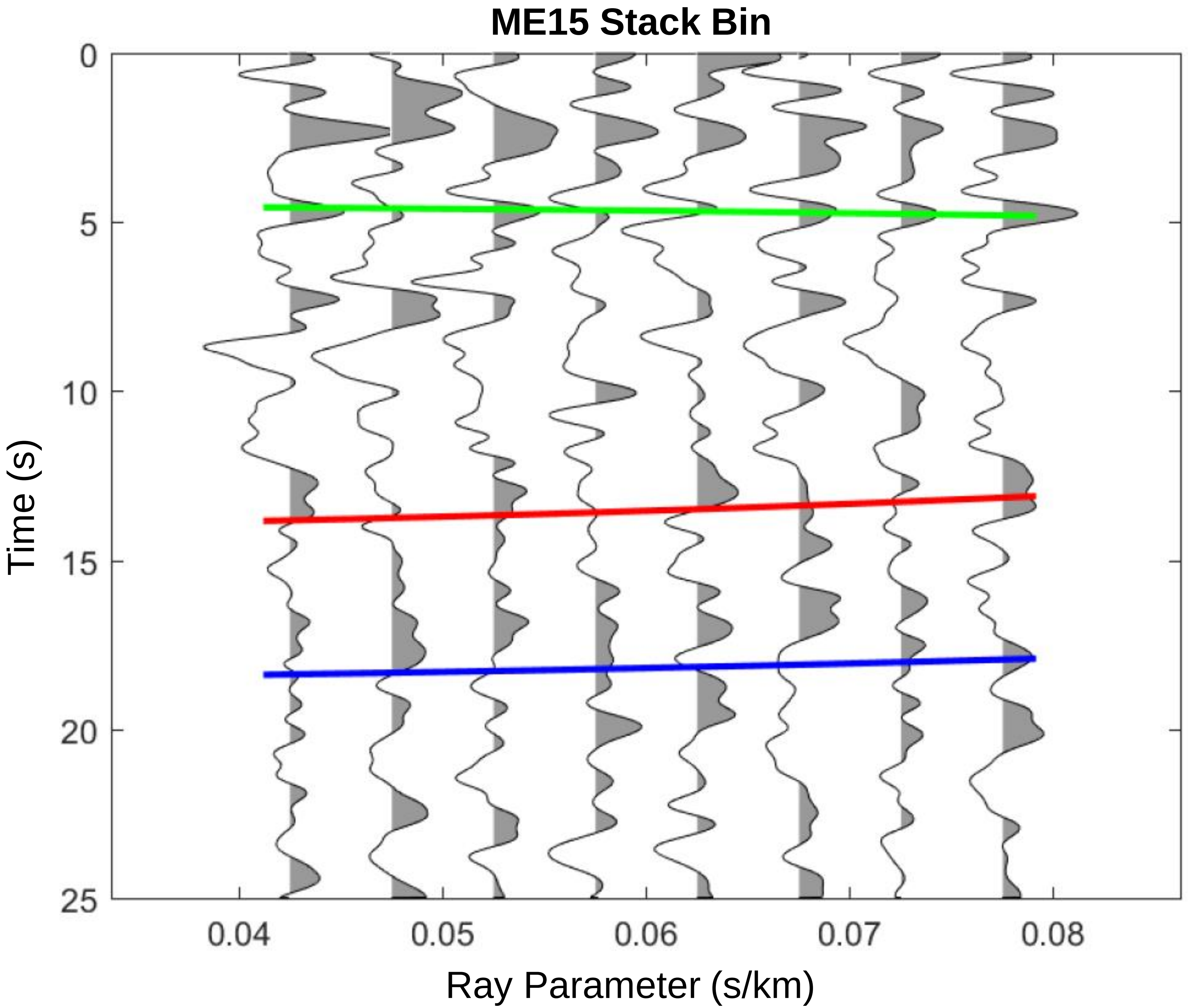
ME15 Stack Bin
Time (s)
0
5
10
15
20
25
0.04
0.05
0.06
0.07
0.08
Ray Parameter (s/km)

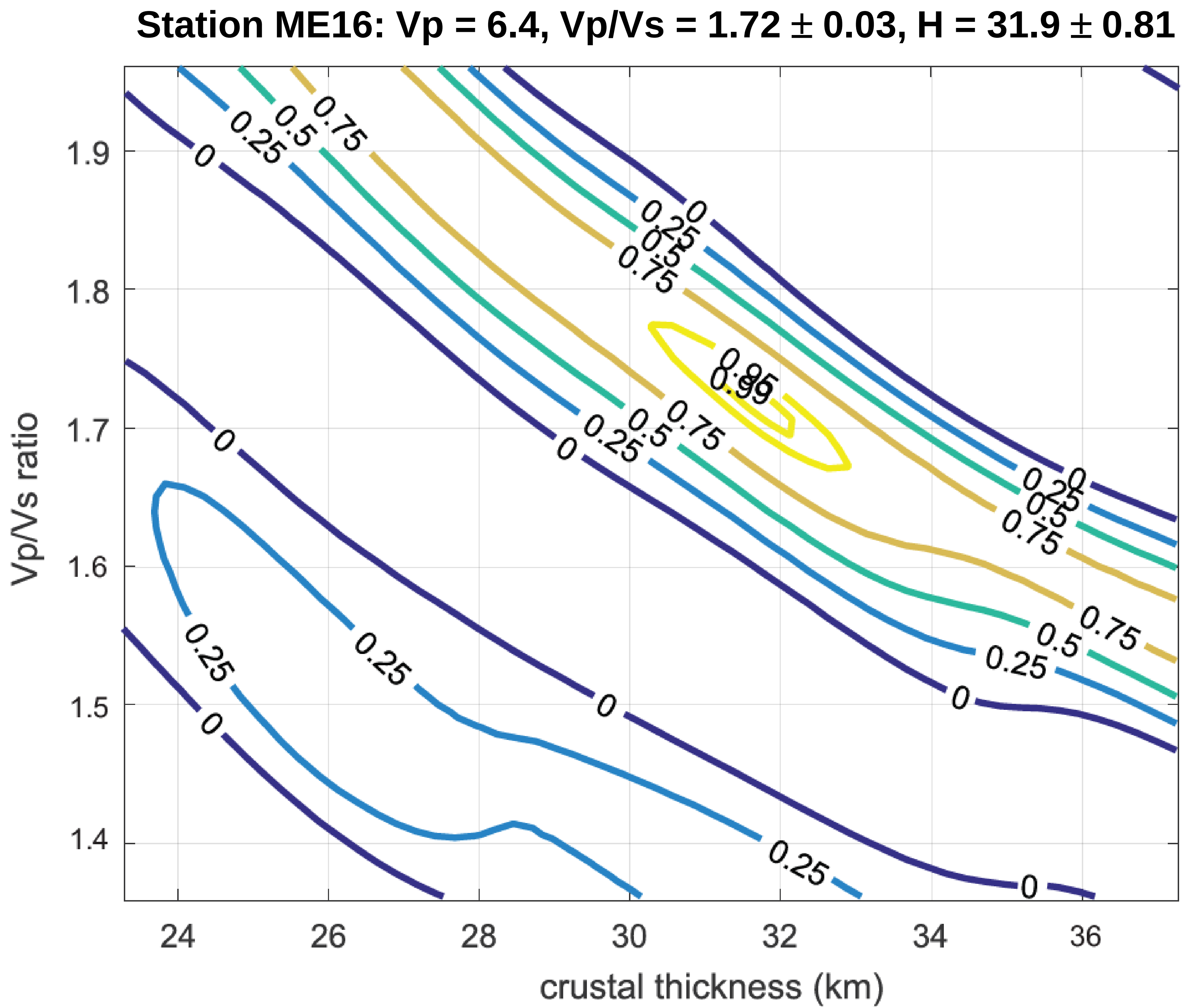
Station ME16: Vp = 6.4, Vp/Vs = 1.72 ± 0.03, H = 31.9 ± 0.81
Vp/Vs ratio
crustal thickness (km)
1.4
1.5
1.6
1.7
1.8
1.9
24
26
28
30
32
34
36
0
0.25
0.5
0.75
0.95
0.99

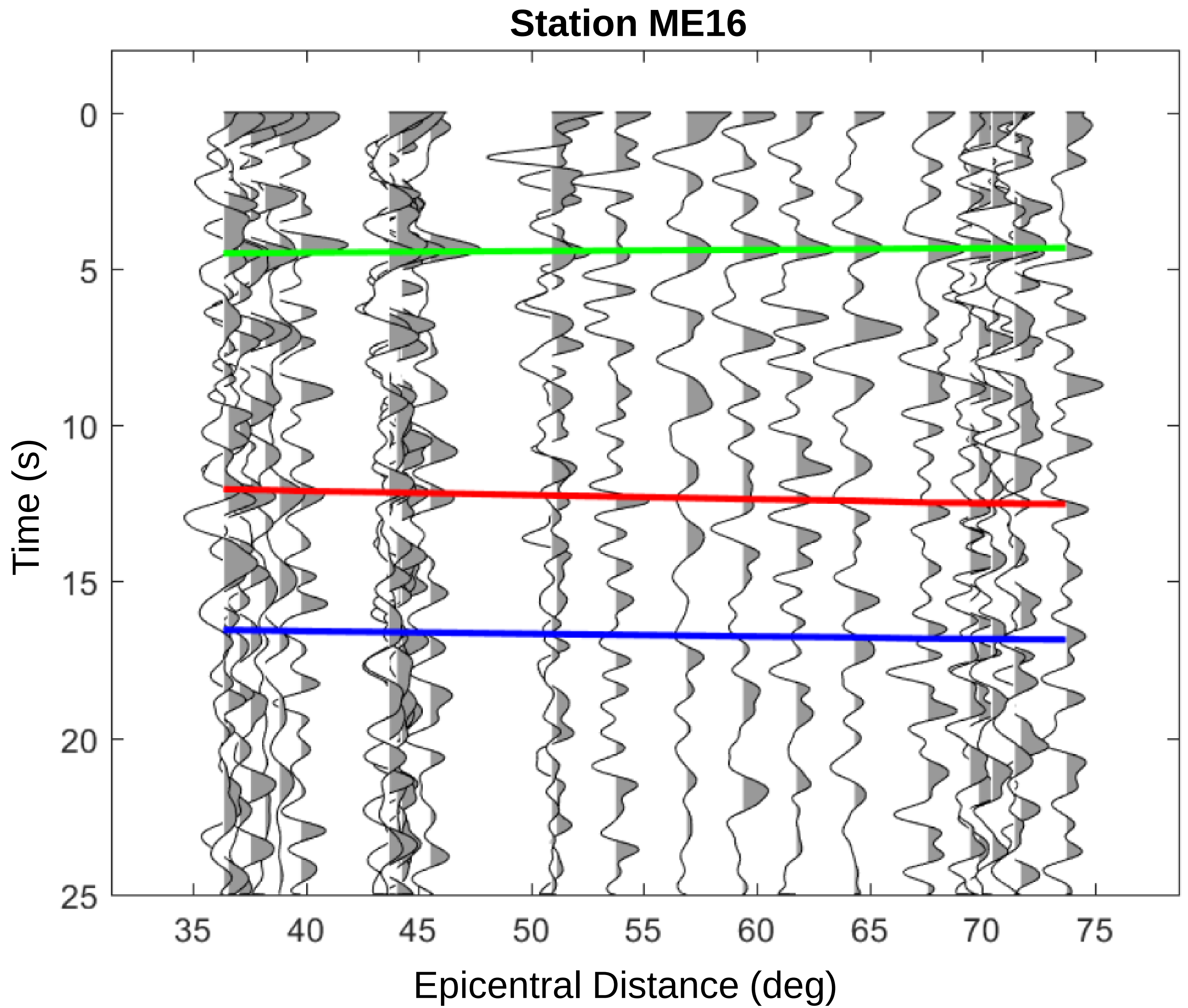

Station ME16
Time (s)
0
5
10
15
20
25
35
40
45
50
55
60
65
70
75
Epicentral Distance (deg)

Station ME17: Vp = 6.4, Vp/Vs = 1.7 ± 0.03, H = 31.7 ± 0.81

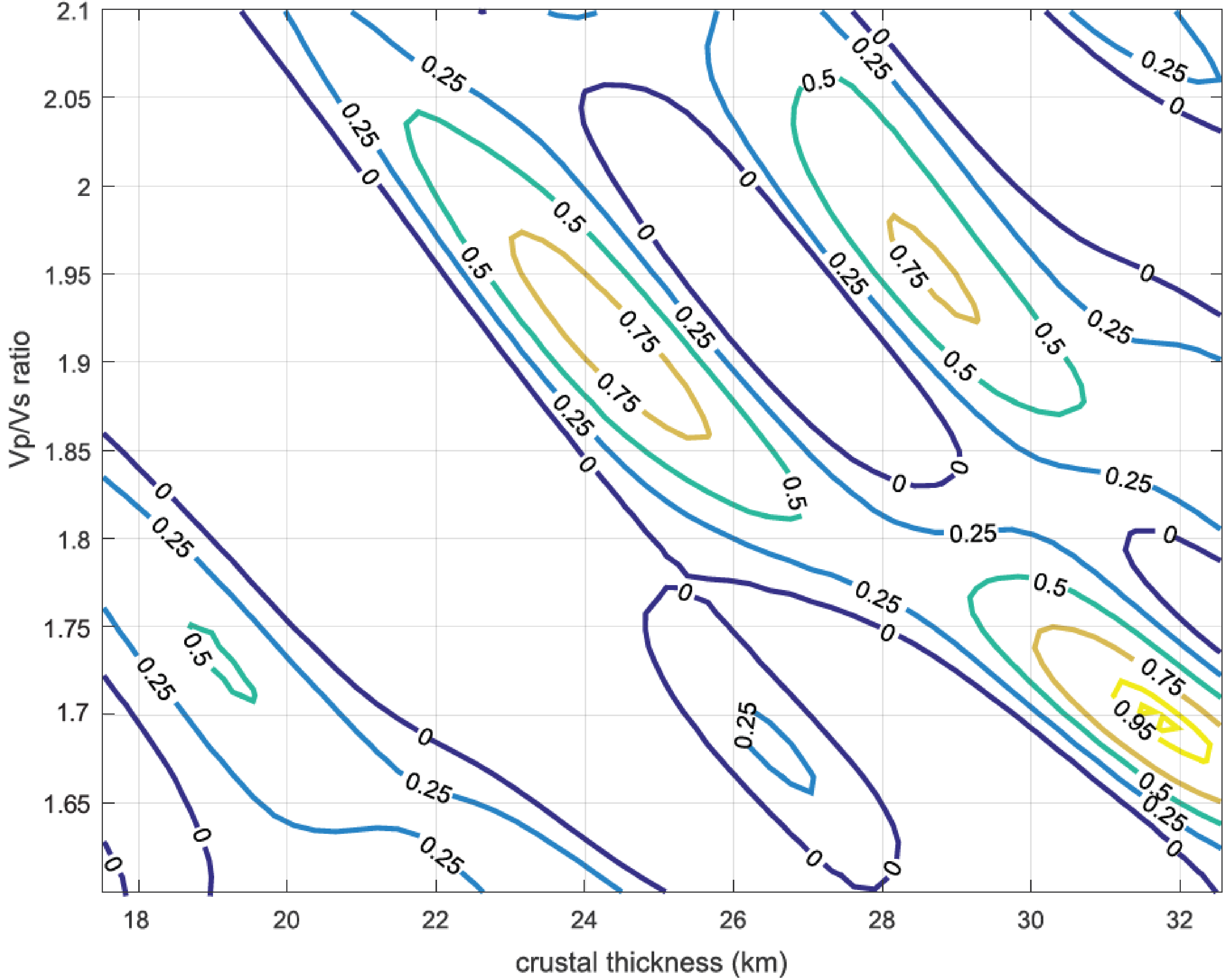

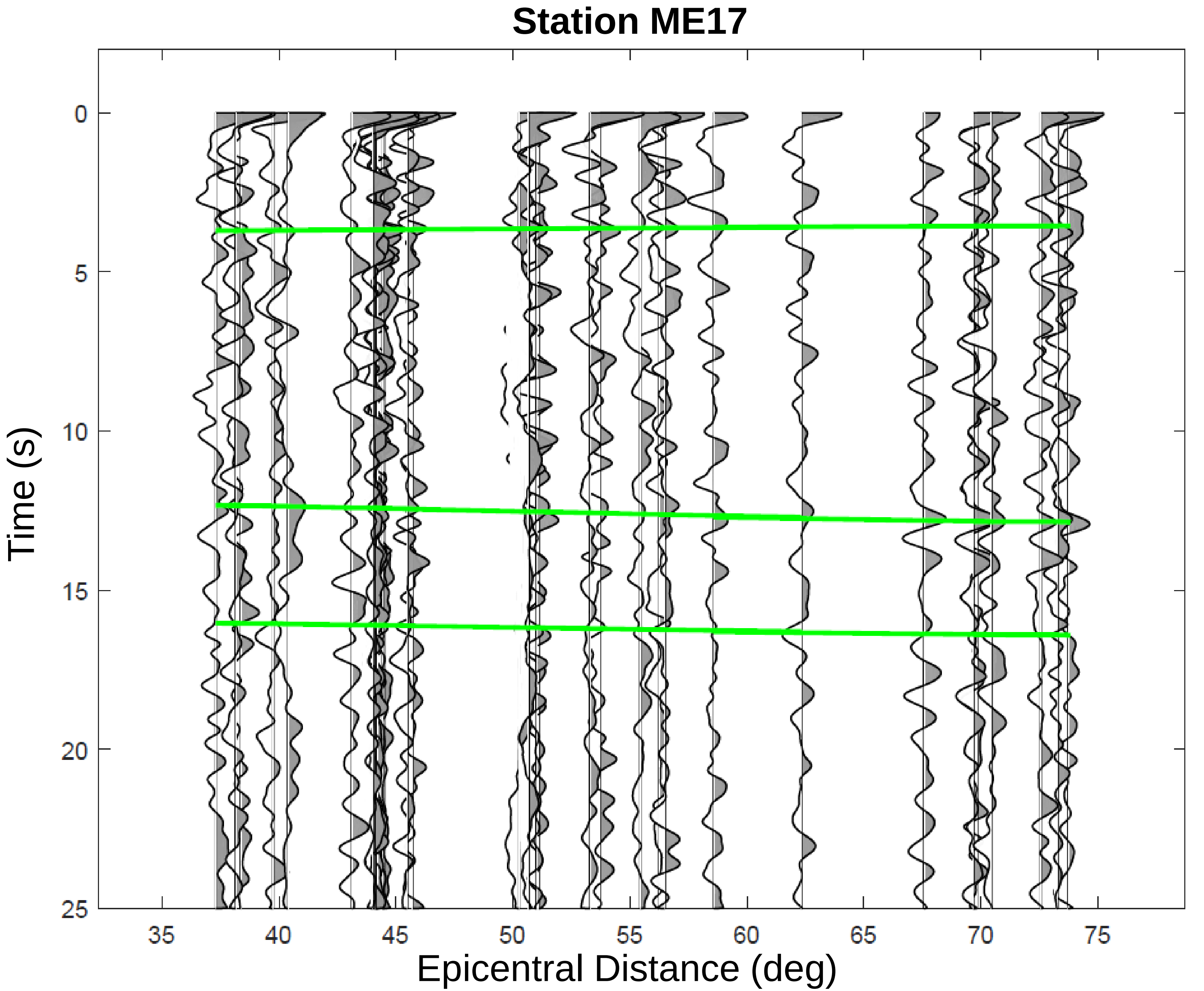
Station ME17
0
5
10
15
20
25
Time (s)
35
40
45
50
55
60
65
70
75
Epicentral Distance (deg)

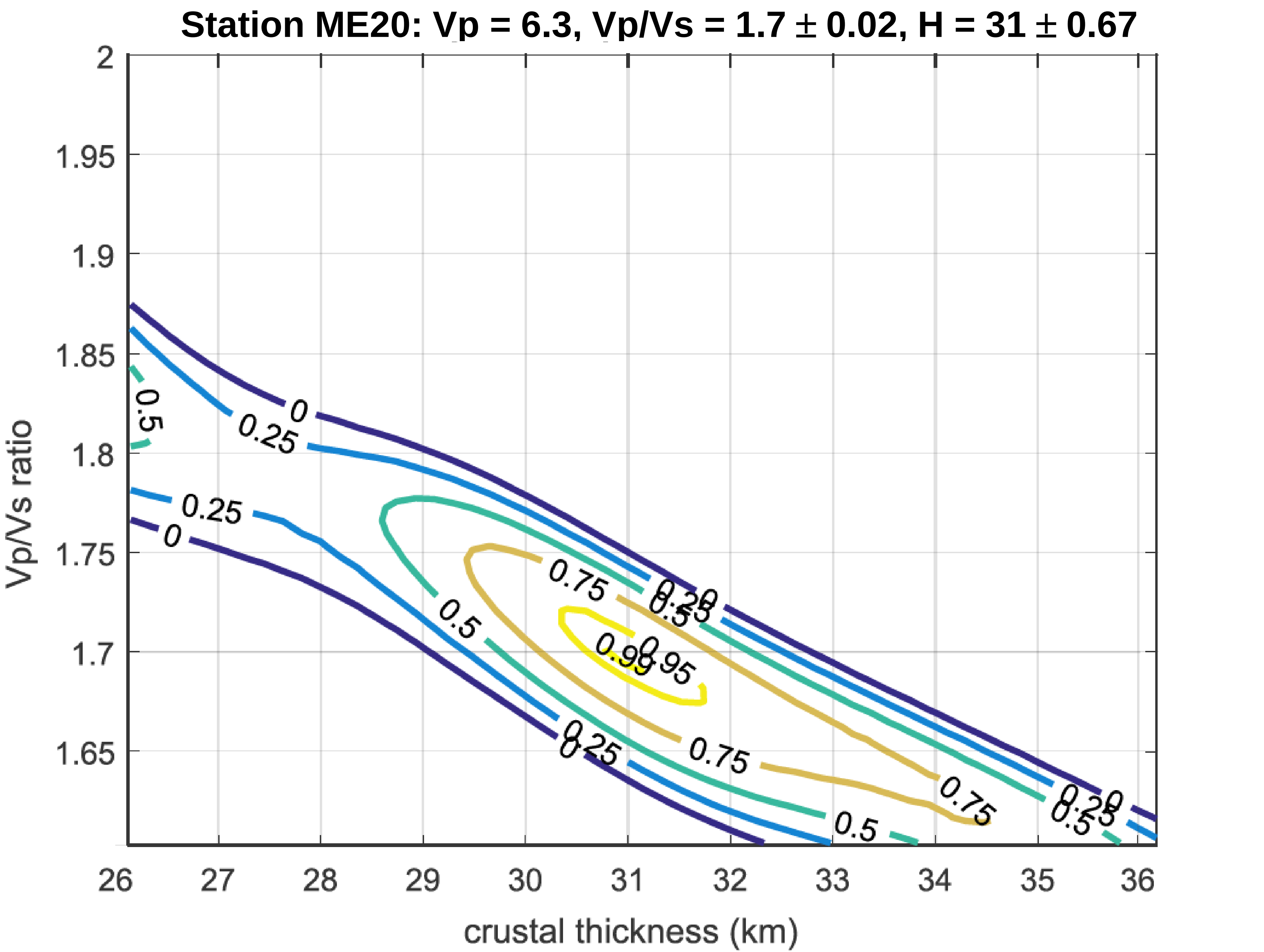

Station ME20: Vp = 6.3, Vp/Vs = 1.7 ± 0.02, H = 31 ± 0.67
Vp/Vs ratio
crustal thickness (km)
2
1.95
1.9
1.85
1.8
1.75
1.7
1.65
26
27
28
29
30
31
32
33
34
35
36
0
0.25
0.5
0.75
0.95
0.99

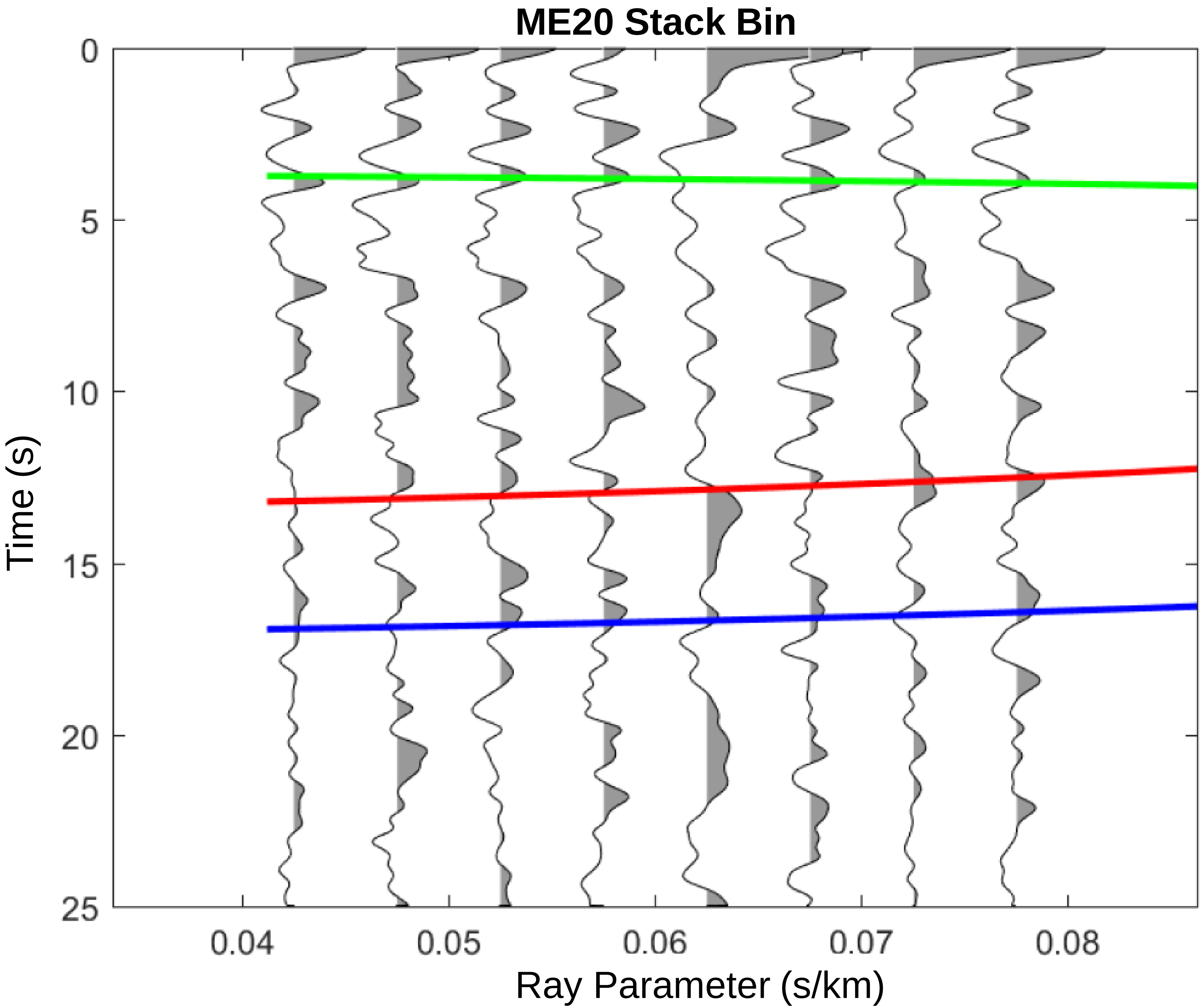
ME20 Stack Bin
Time (s)
0
5
10
15
20
25
0.04
0.05
0.06
0.07
0.08
Ray Parameter (s/km)

Station ME21: Vp = 6.3, Vp/Vs = 1.9 ± 0.09, H = 30 ± 1.08

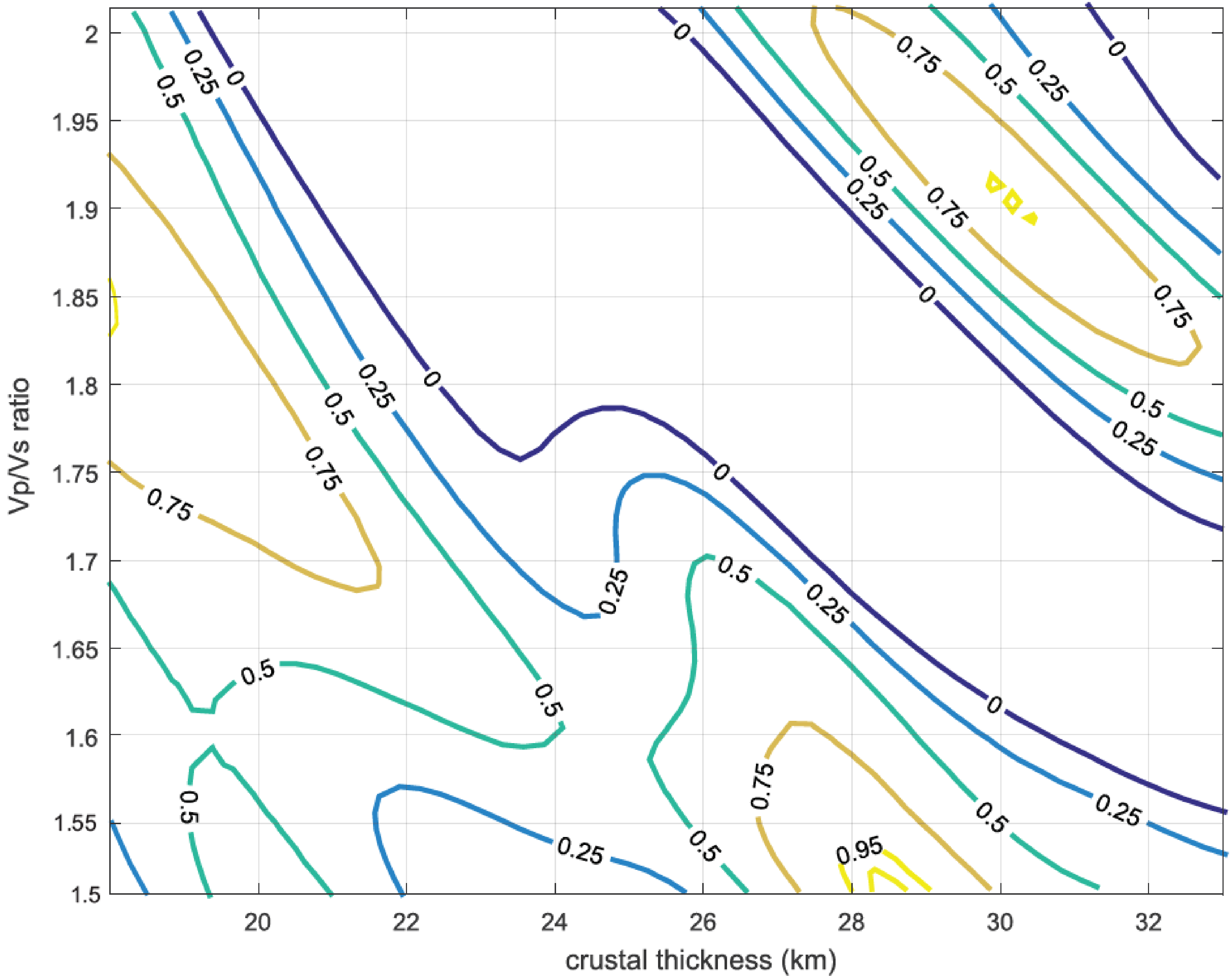

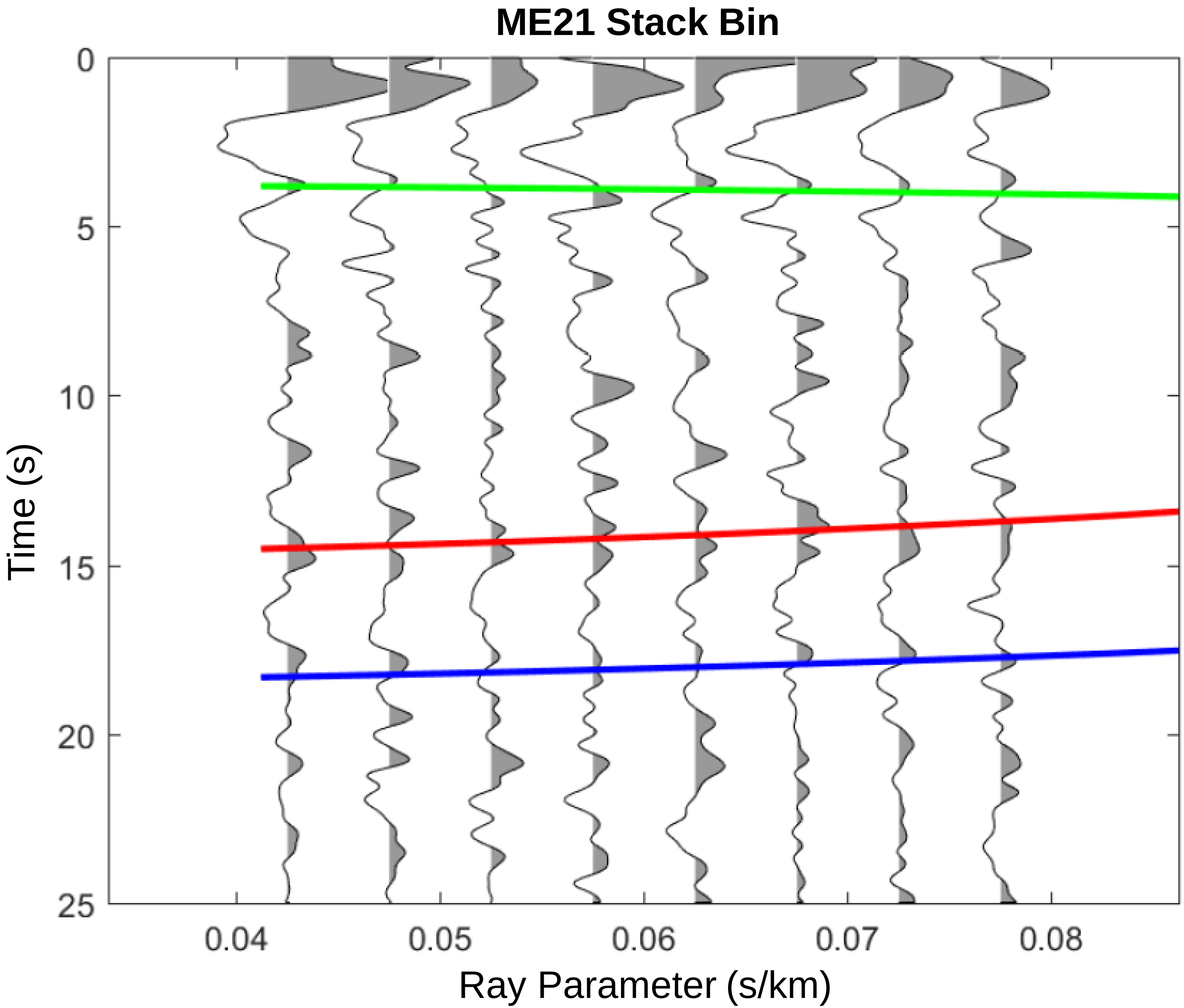
ME21 Stack Bin
Time (s)
0
5
10
15
20
25
0.04
0.05
0.06
0.07
0.08
Ray Parameter (s/km)

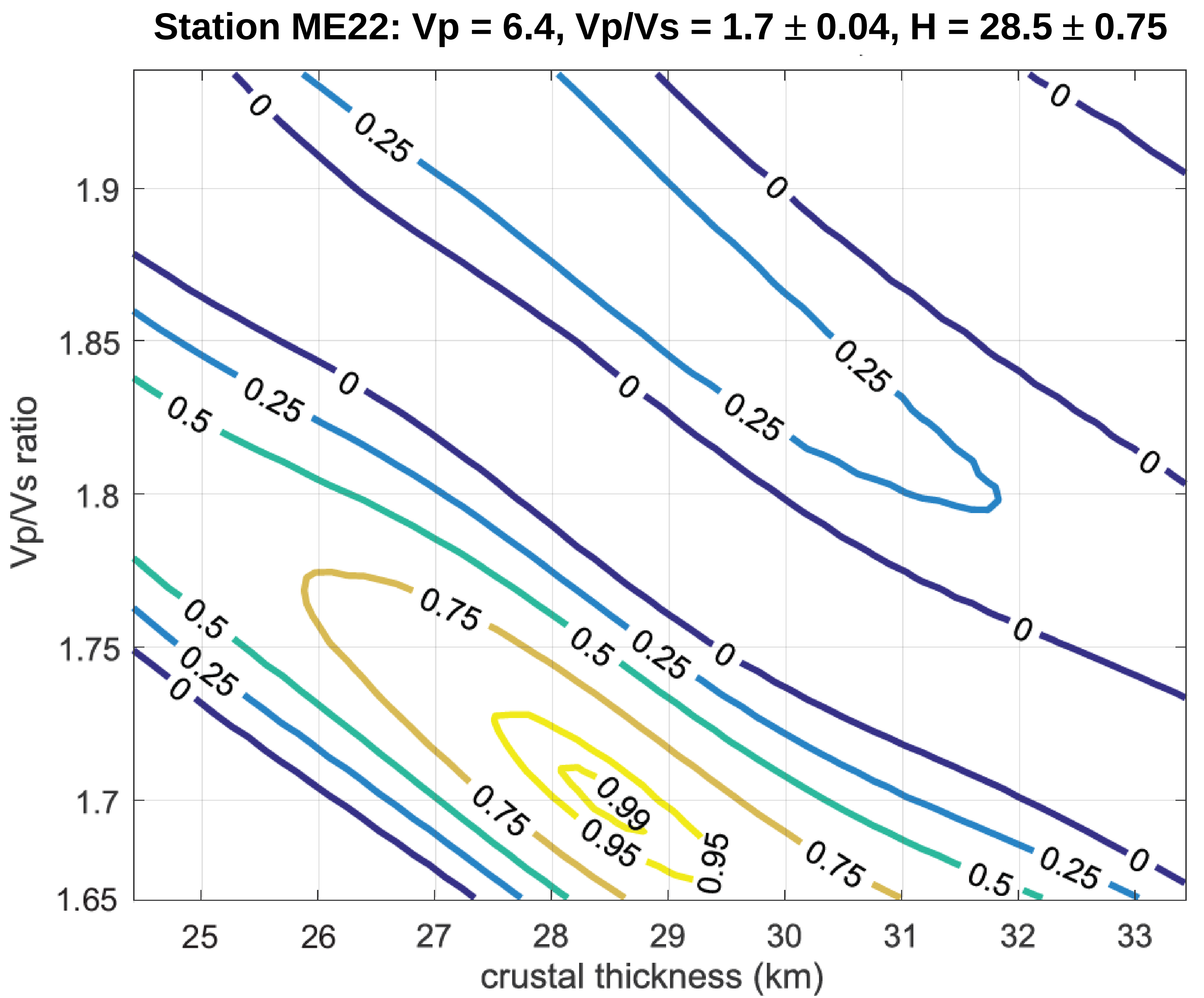
Station ME22: Vp = 6.4, Vp/Vs = 1.7 ± 0.04, H = 28.5 ± 0.75
Vp/Vs ratio
crustal thickness (km)
1.9
1.85
1.8
1.75
1.7
1.65
25
26
27
28
29
30
31
32
33
0
0.25
0.5
0.75
0.95
0.99

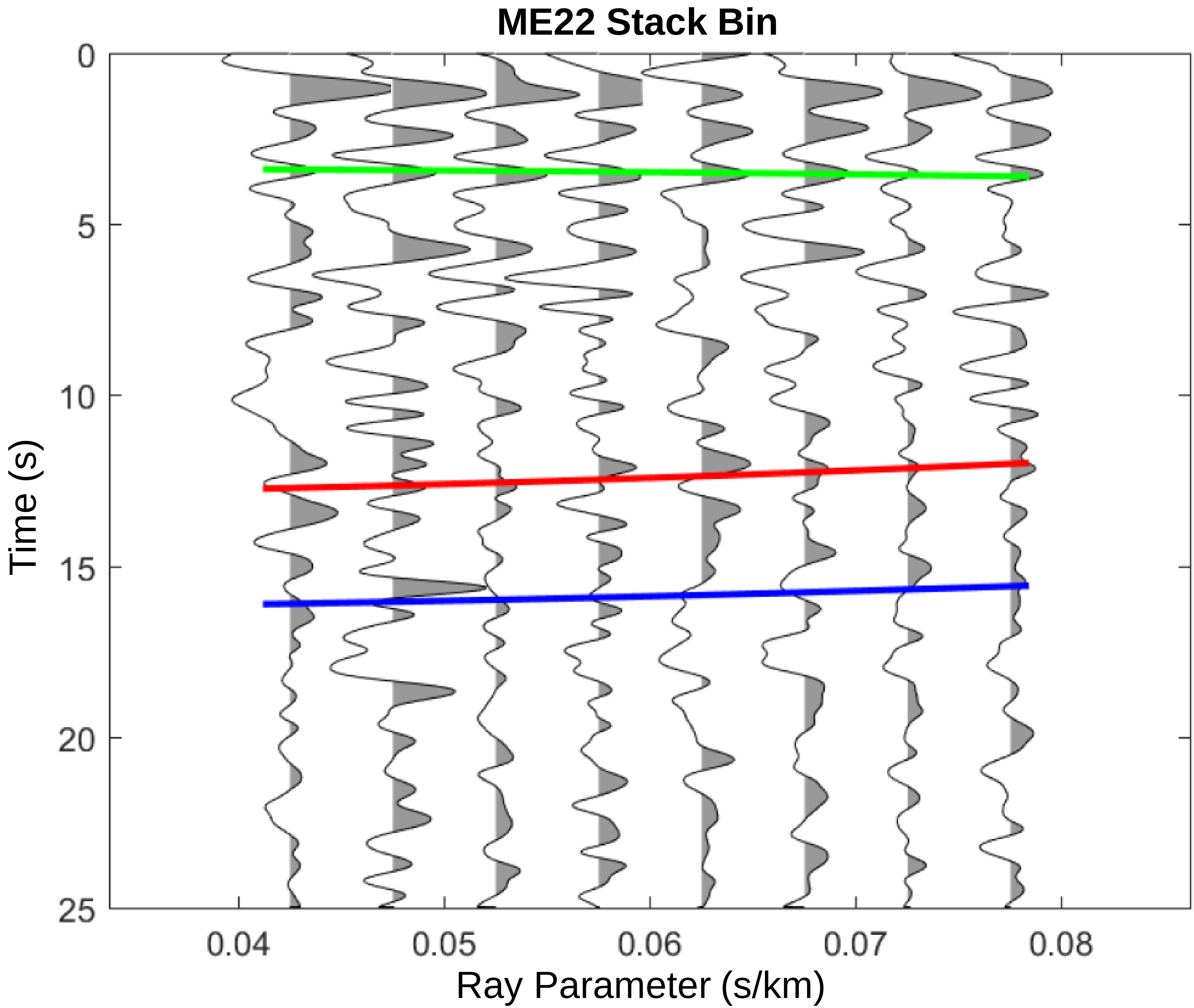
ME22 Stack Bin
Time (s)
0
5
10
15
20
25
0.04
0.05
0.06
0.07
0.08
Ray Parameter (s/km)

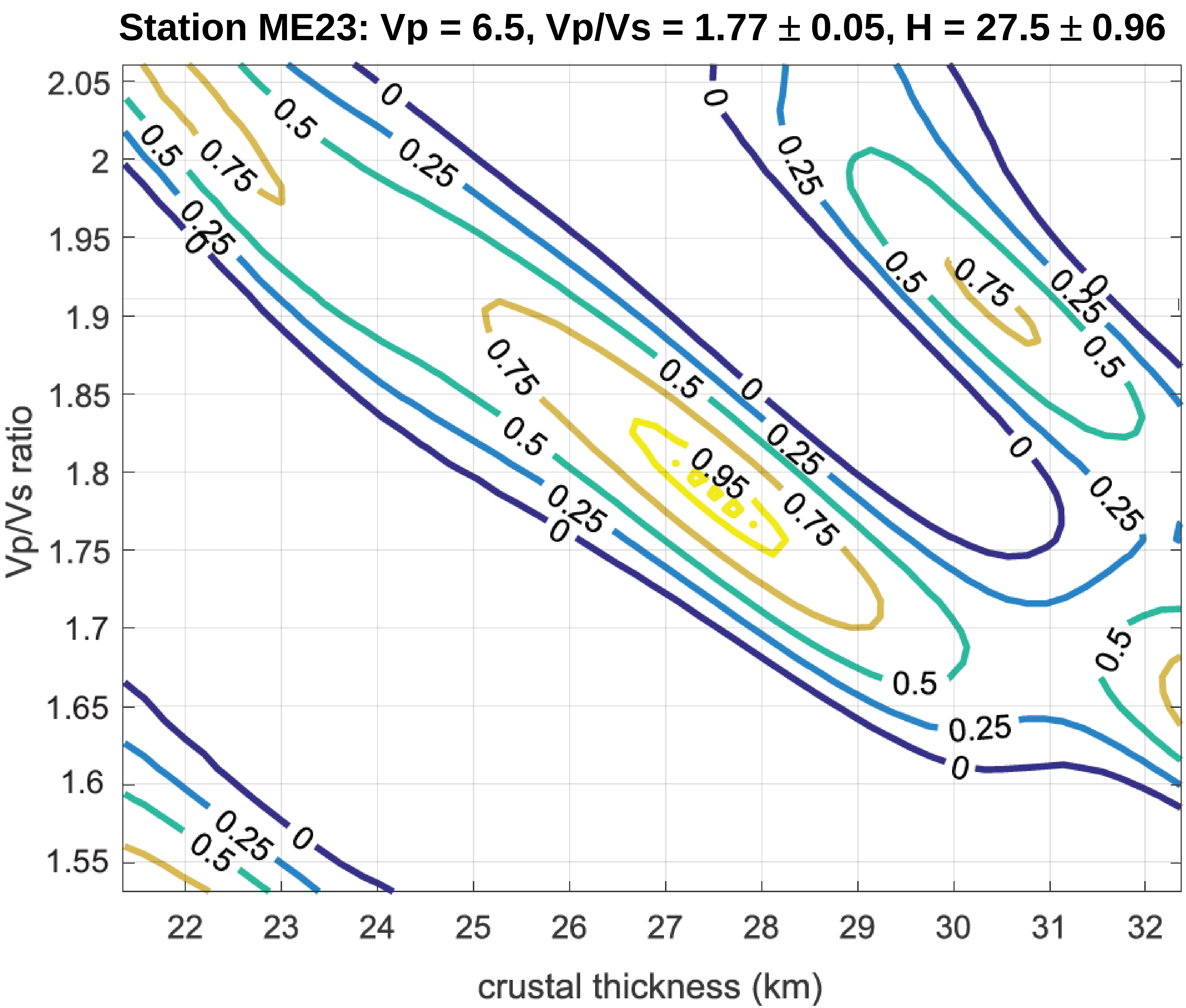

Station ME23: Vp = 6.5, Vp/Vs = 1.77 ± 0.05, H = 27.5 ± 0.96
Vp/Vs ratio
crustal thickness (km)
2.05
2
1.95
1.9
1.85
1.8
1.75
1.7
1.65
1.6
1.55
22
23
24
25
26
27
28
29
30
31
32
0
0.25
0.5
0.75
0.95

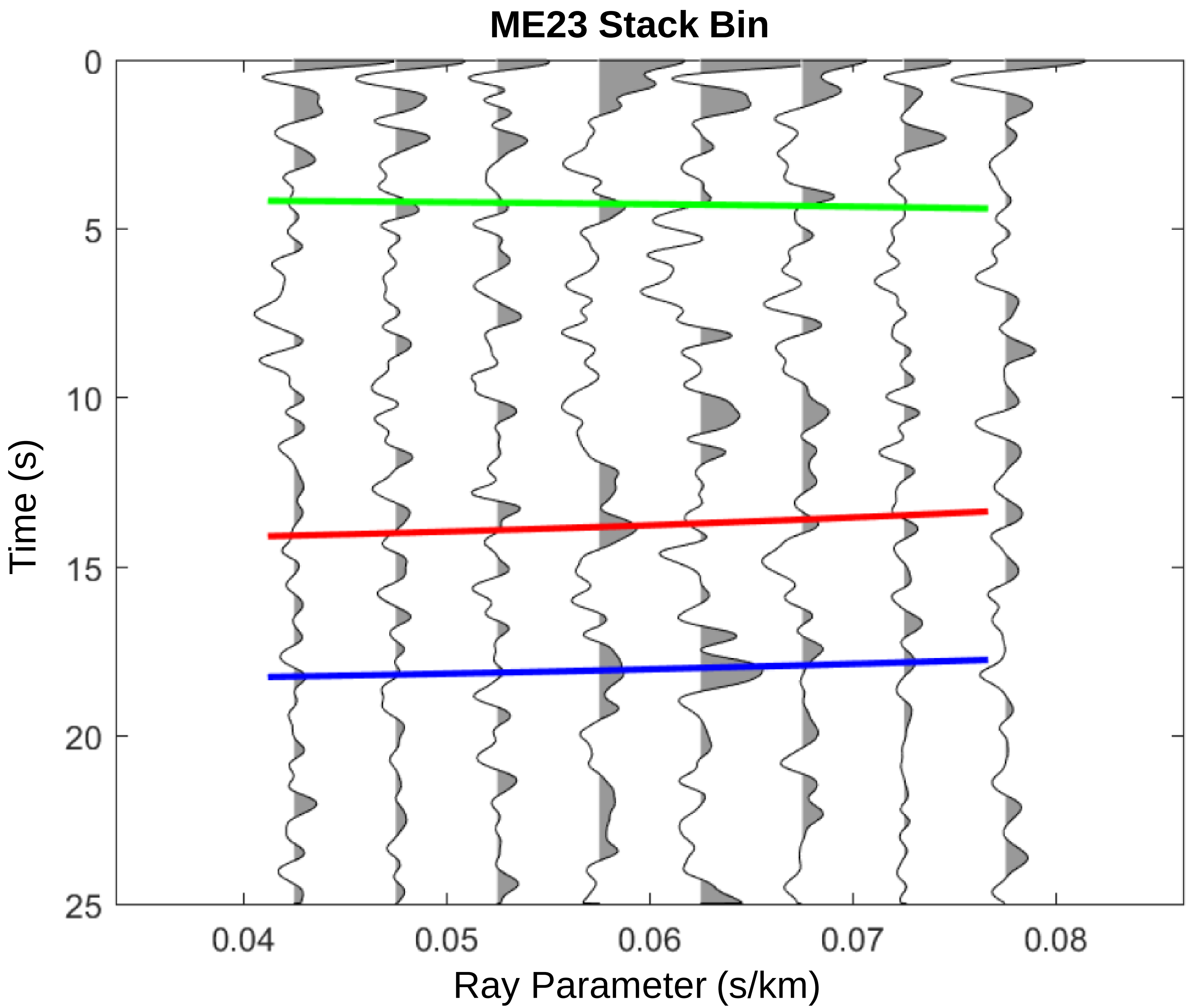
ME23 Stack Bin
Time (s)
0
5
10
15
20
25
Ray Parameter (s/km)
0.04
0.05
0.06
0.07
0.08

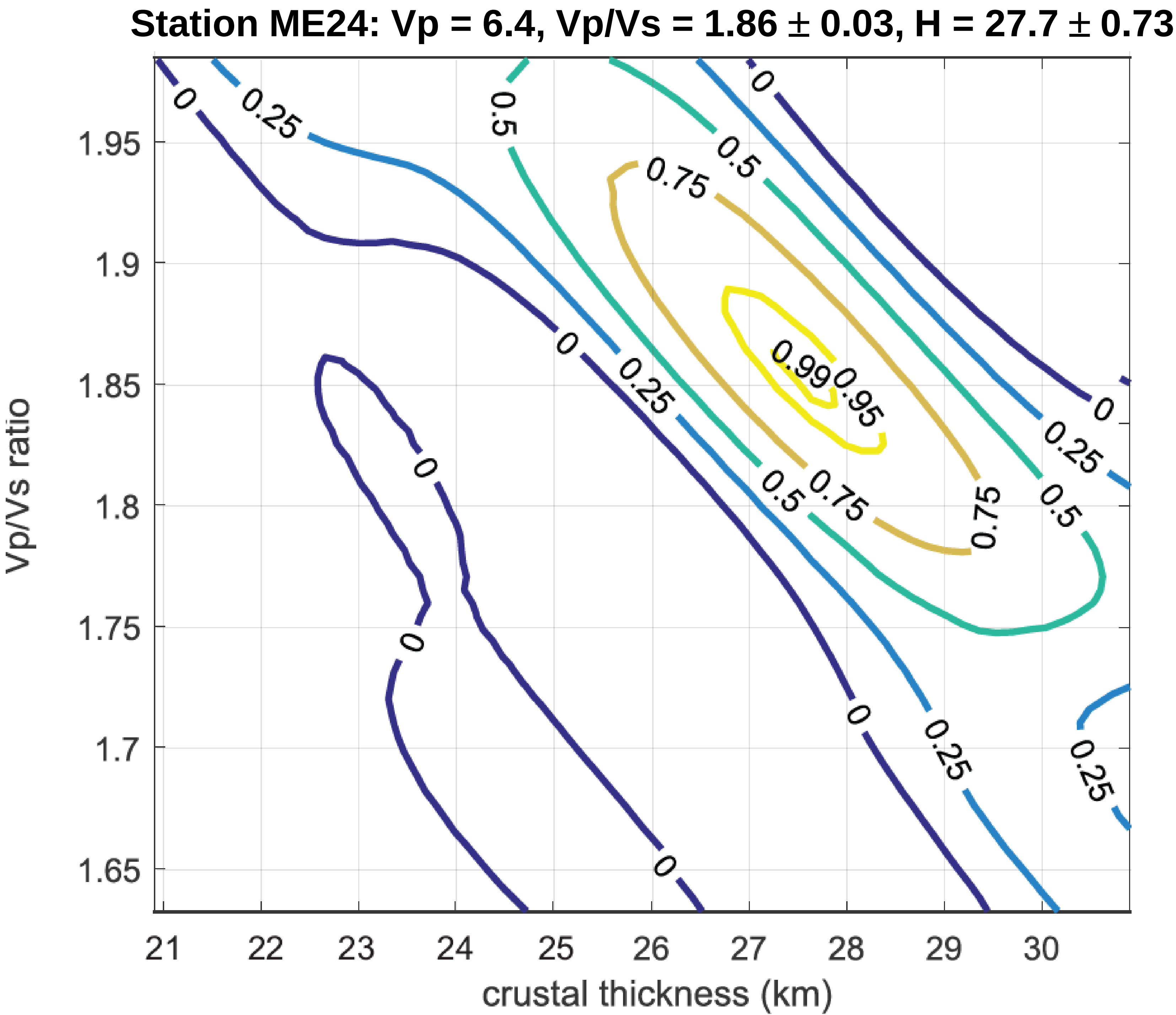

Station ME24: Vp = 6.4, Vp/Vs = 1.86 ± 0.03, H = 27.7 ± 0.73
Vp/Vs ratio
1.95
1.9
1.85
1.8
1.75
1.7
1.65
crustal thickness (km)
21
22
23
24
25
26
27
28
29
30
0
0.25
0.5
0.75
0.95
0.99

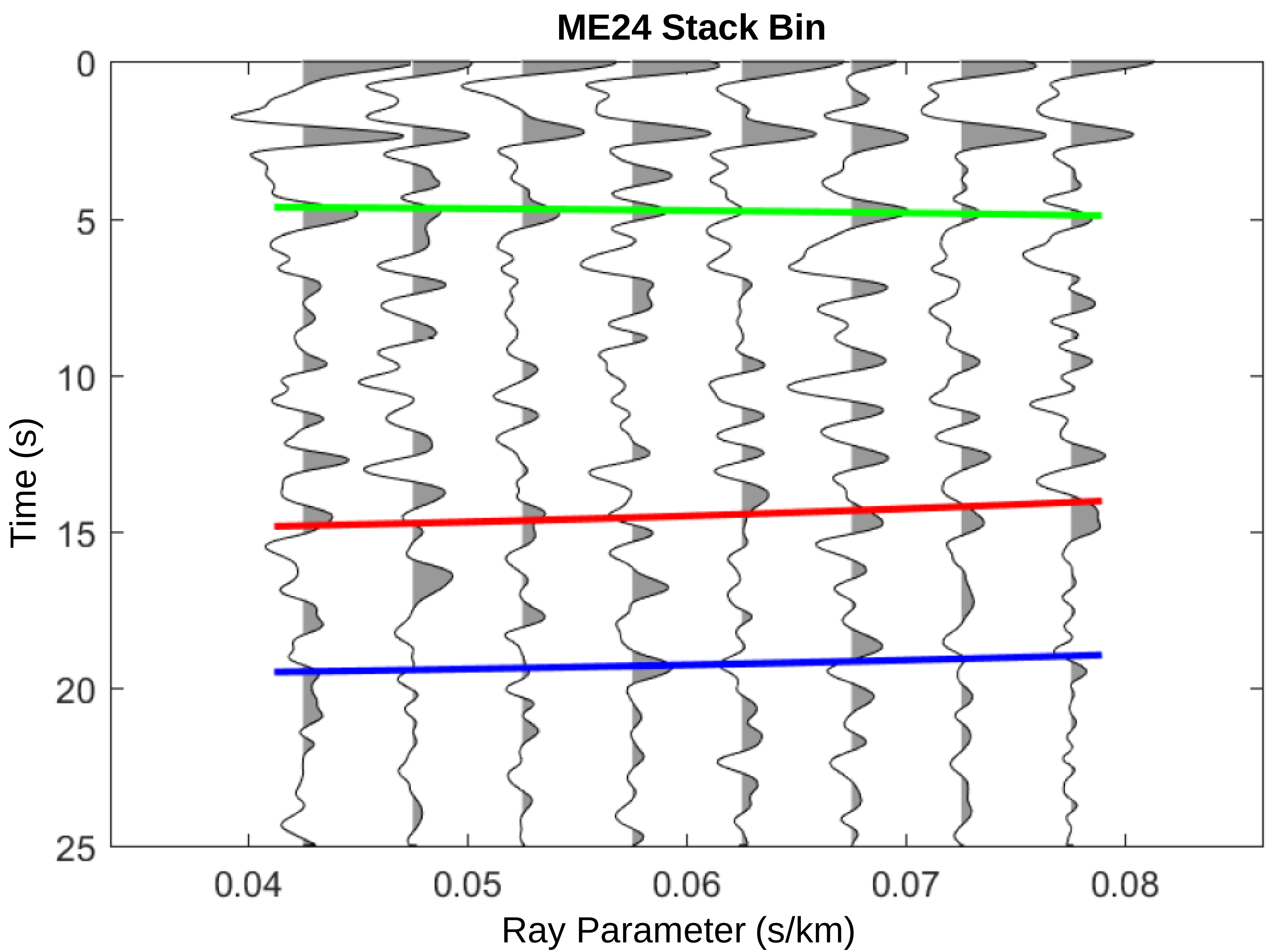
ME24 Stack Bin
Time (s)
0
5
10
15
20
25
0.04
0.05
0.06
0.07
0.08
Ray Parameter (s/km)

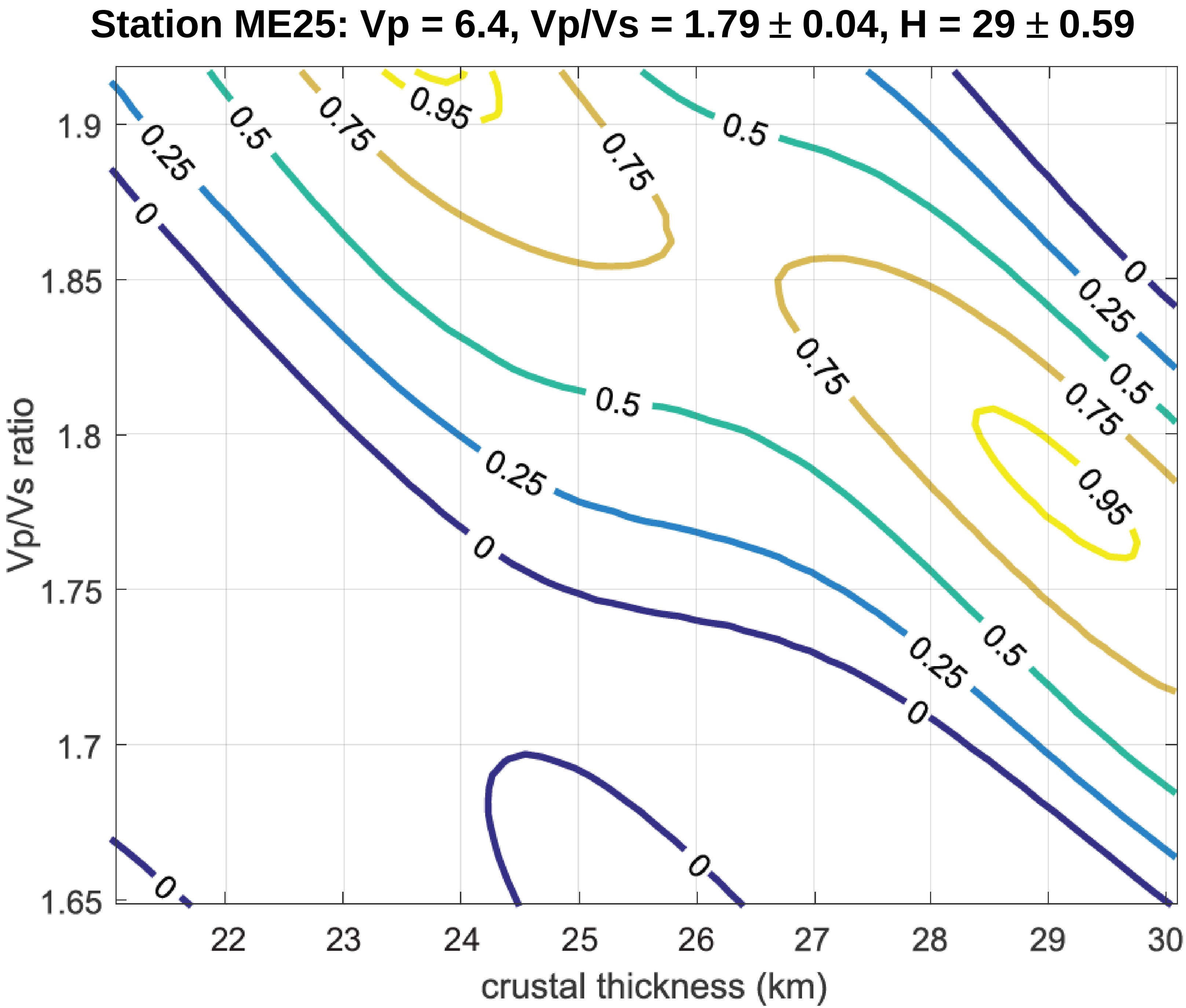

Station ME25: Vp = 6.4, Vp/Vs = 1.79 ± 0.04, H = 29 ± 0.59
Vp/Vs ratio
crustal thickness (km)
1.9
1.85
1.8
1.75
1.7
1.65
22
23
24
25
26
27
28
29
30
0
0.25
0.5
0.75
0.95

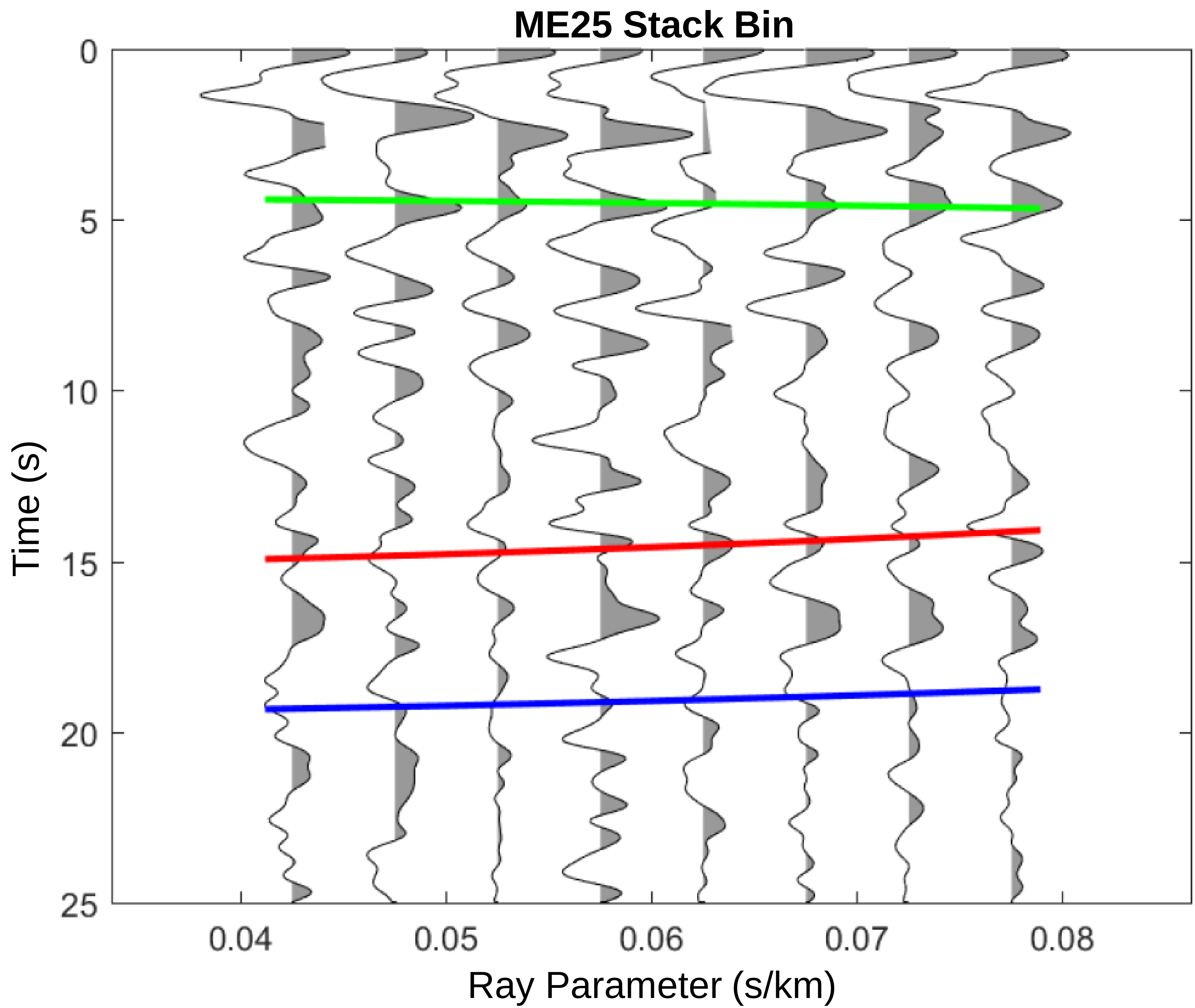
ME25 Stack Bin
Time (s)
0
5
10
15
20
25
0.04
0.05
0.06
0.07
0.08
Ray Parameter (s/km)

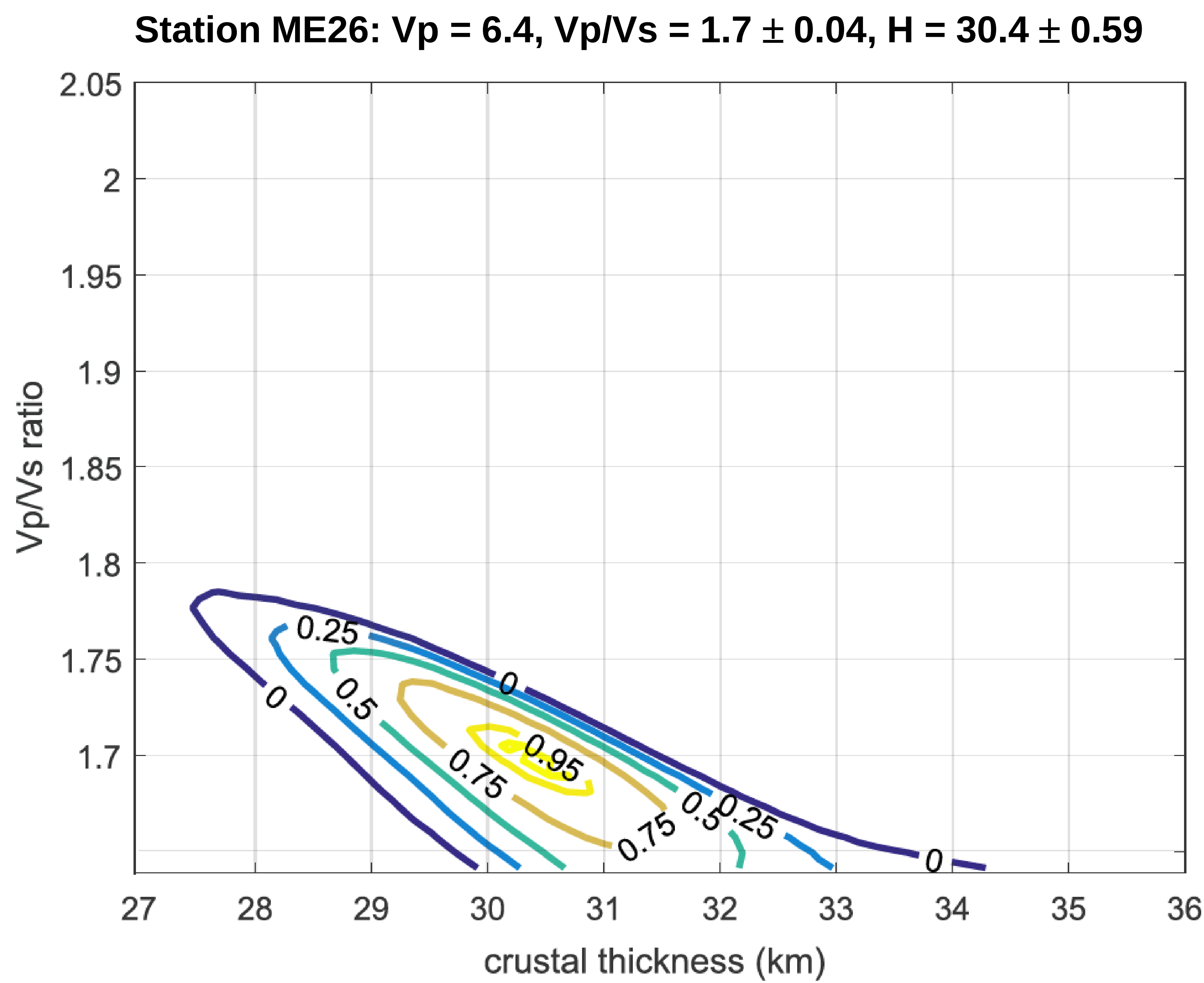
Station ME26: Vp = 6.4, Vp/Vs = 1.7 ± 0.04, H = 30.4 ± 0.59
Vp/Vs ratio
2.05
2
1.95
1.9
1.85
1.8
1.75
1.7
27
28
29
30
31
32
33
34
35
36
crustal thickness (km)
0
0.25
0.5
0.75
0.95

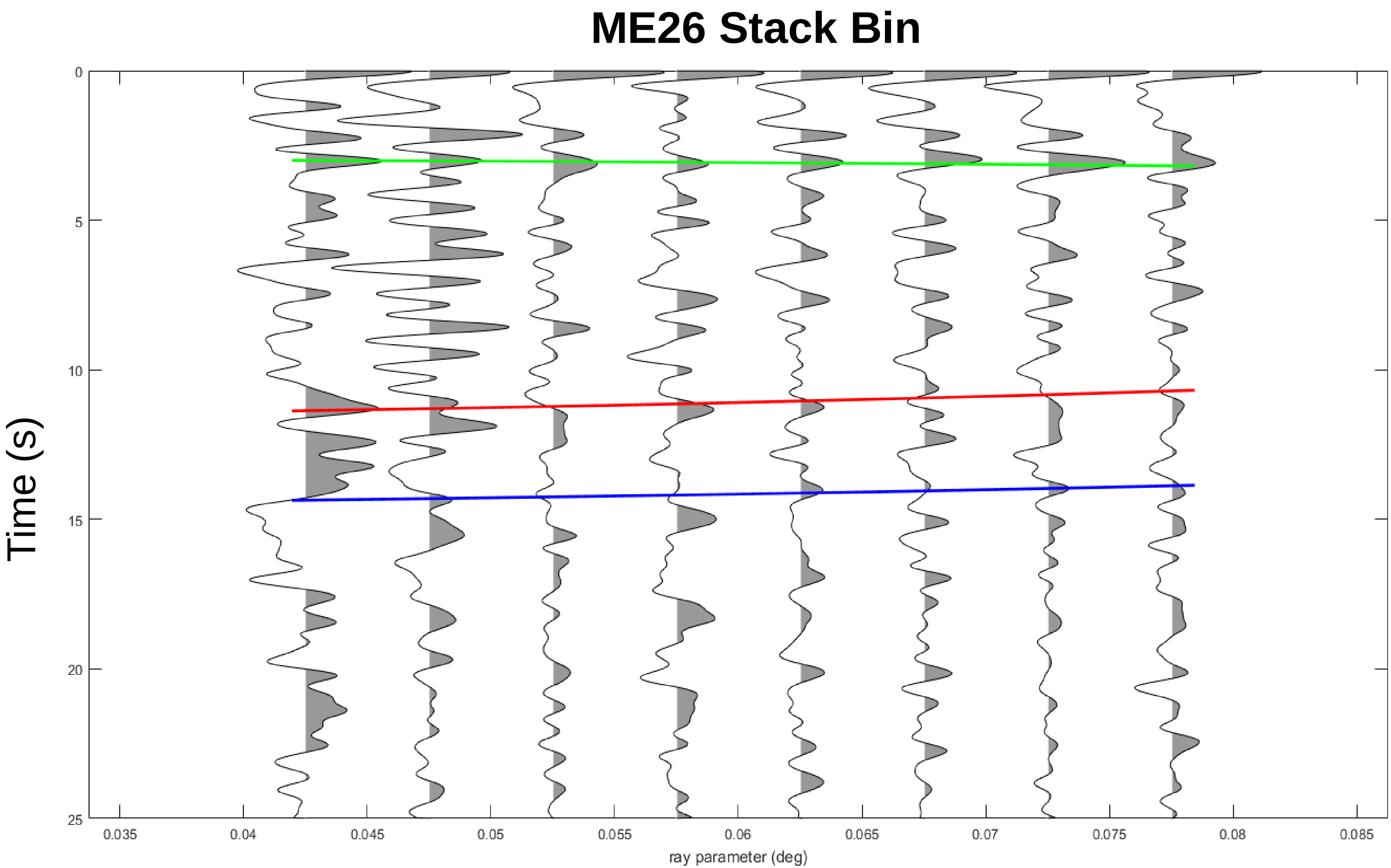
ME26 Stack Bin
Time (s)
0
5
10
15
20
25
0.035
0.04
0.045
0.05
0.055
0.06
0.065
0.07
0.075
0.08
0.085
ray parameter (deg)

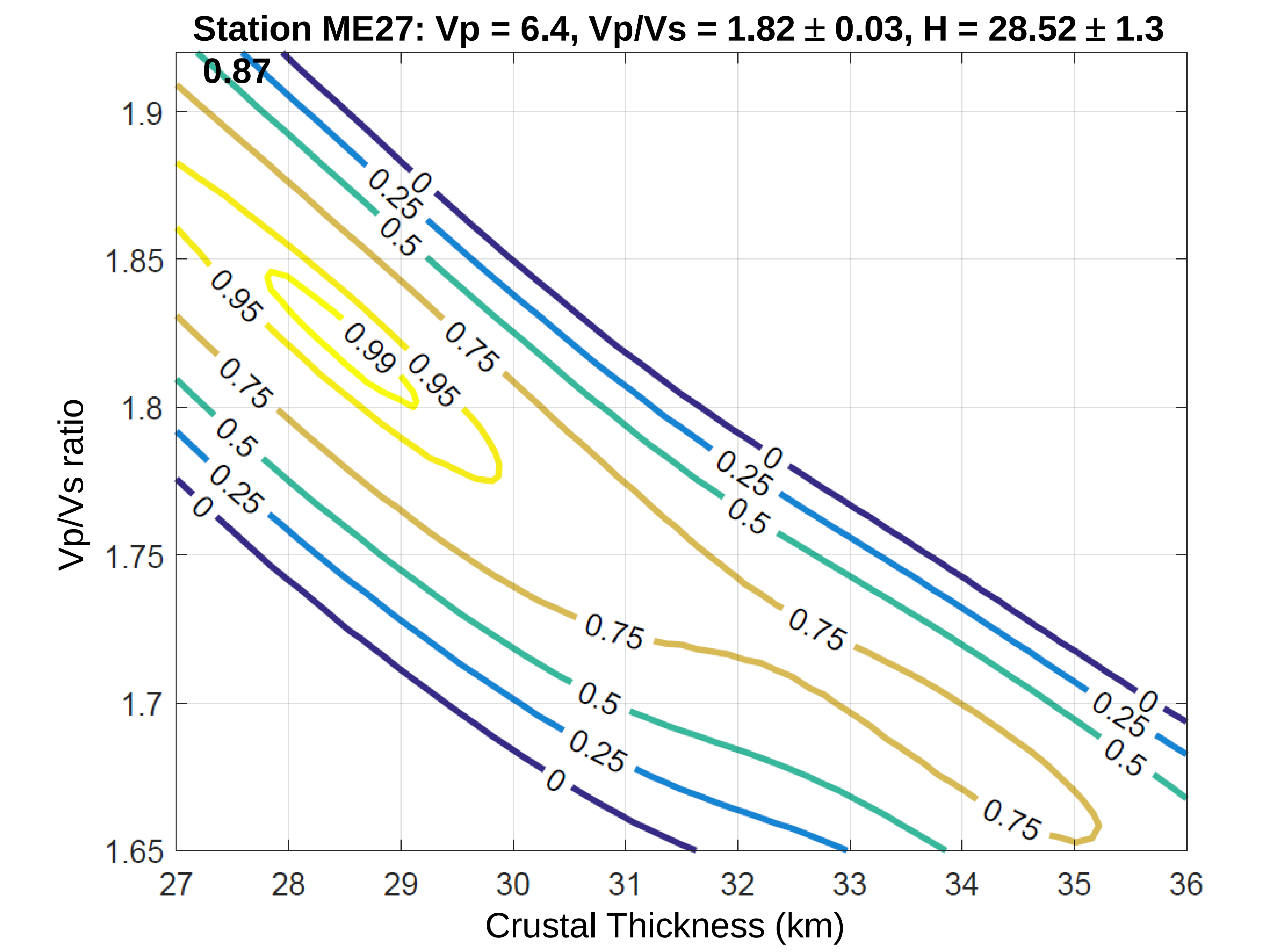
Station ME27: Vp = 6.4, Vp/Vs = 1.82 ± 0.03, H = 28.52 ± 1.3
0.87
0
0.25
0.5
0.75
0.95
0.99
1.9
1.85
1.8
1.75
1.7
1.65
27
28
29
30
31
32
33
34
35
36
Vp/Vs ratio
Crustal Thickness (km)

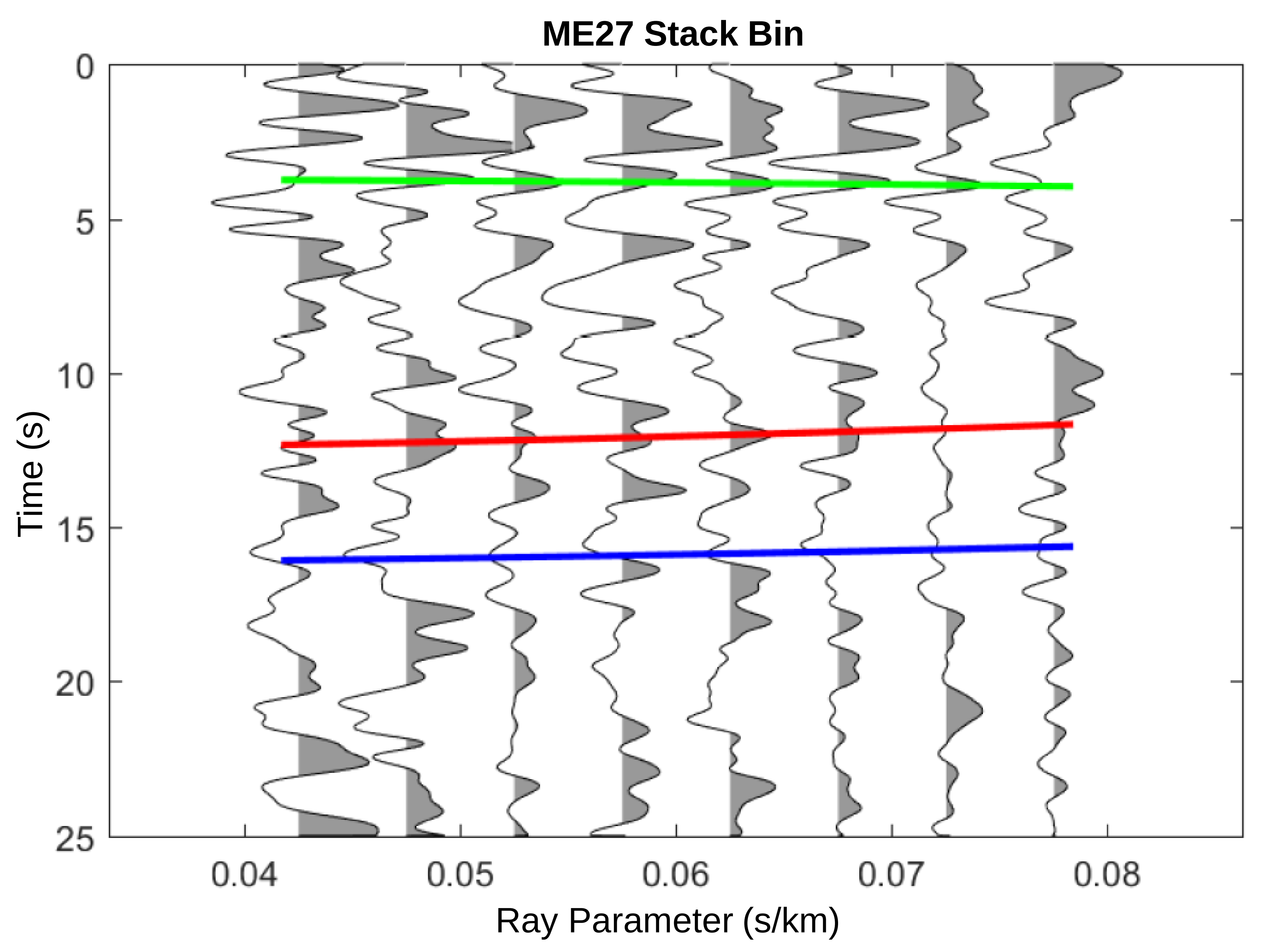
ME27 Stack Bin
Time (s)
0
5
10
15
20
25
0.04
0.05
0.06
0.07
0.08
Ray Parameter (s/km)

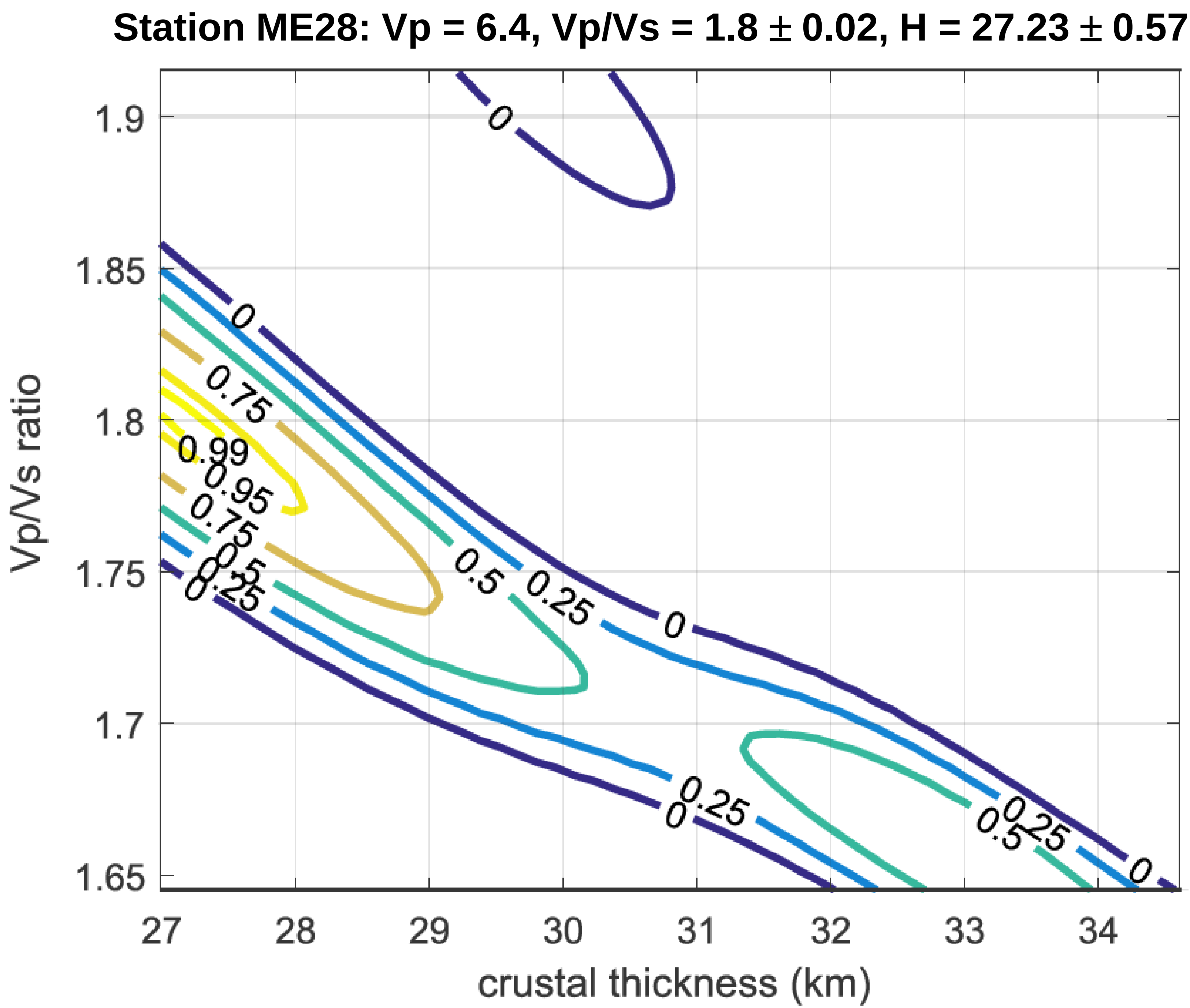

Station ME28: Vp = 6.4, Vp/Vs = 1.8 ± 0.02, H = 27.23 ± 0.57
Vp/Vs ratio
crustal thickness (km)
1.9
1.85
1.8
1.75
1.7
1.65
27
28
29
30
31
32
33
34
0
0.25
0.5
0.75
0.95
0.99

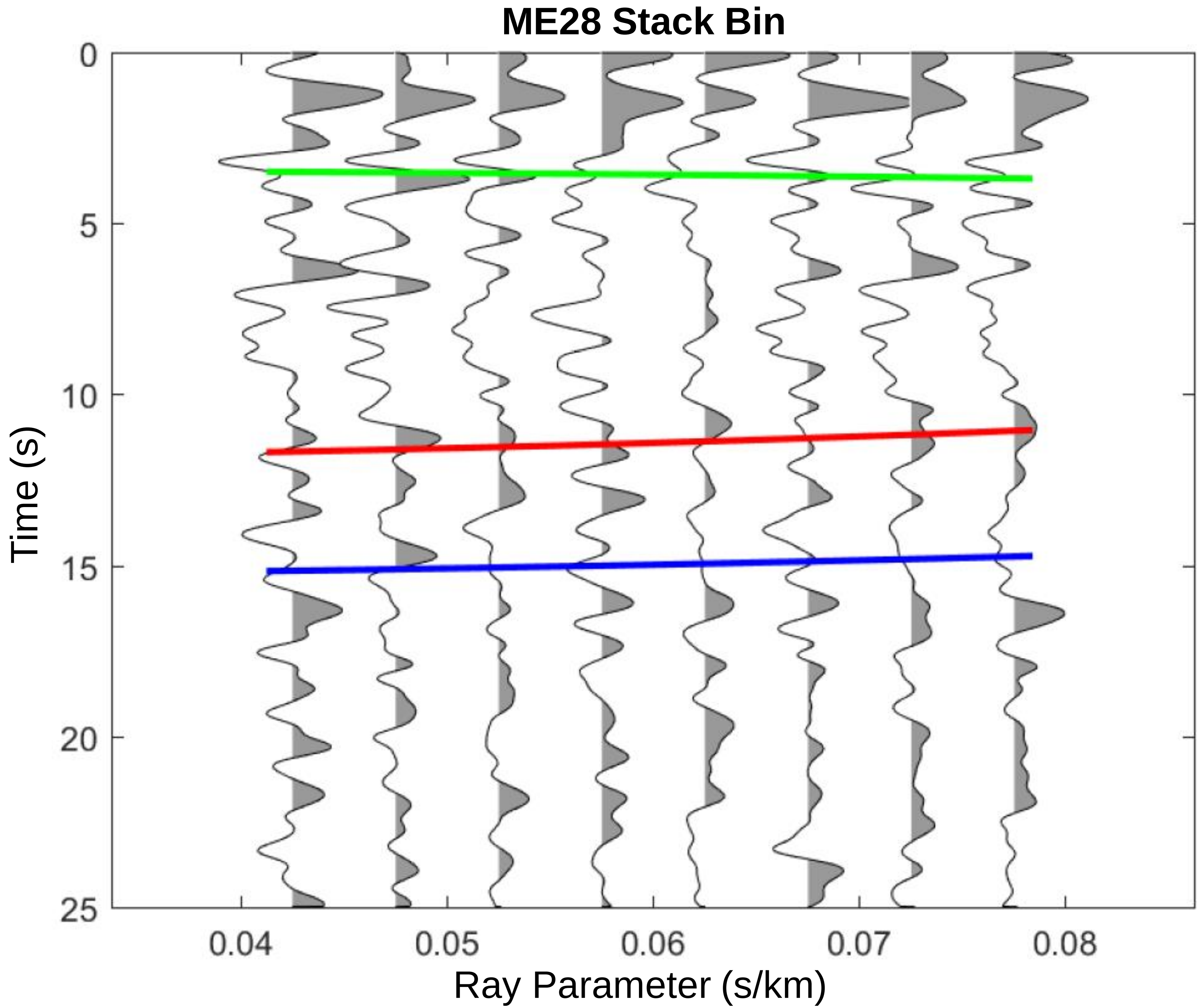

ME28 Stack Bin
Time (s)
0
5
10
15
20
25
0.04
0.05
0.06
0.07
0.08
Ray Parameter (s/km)

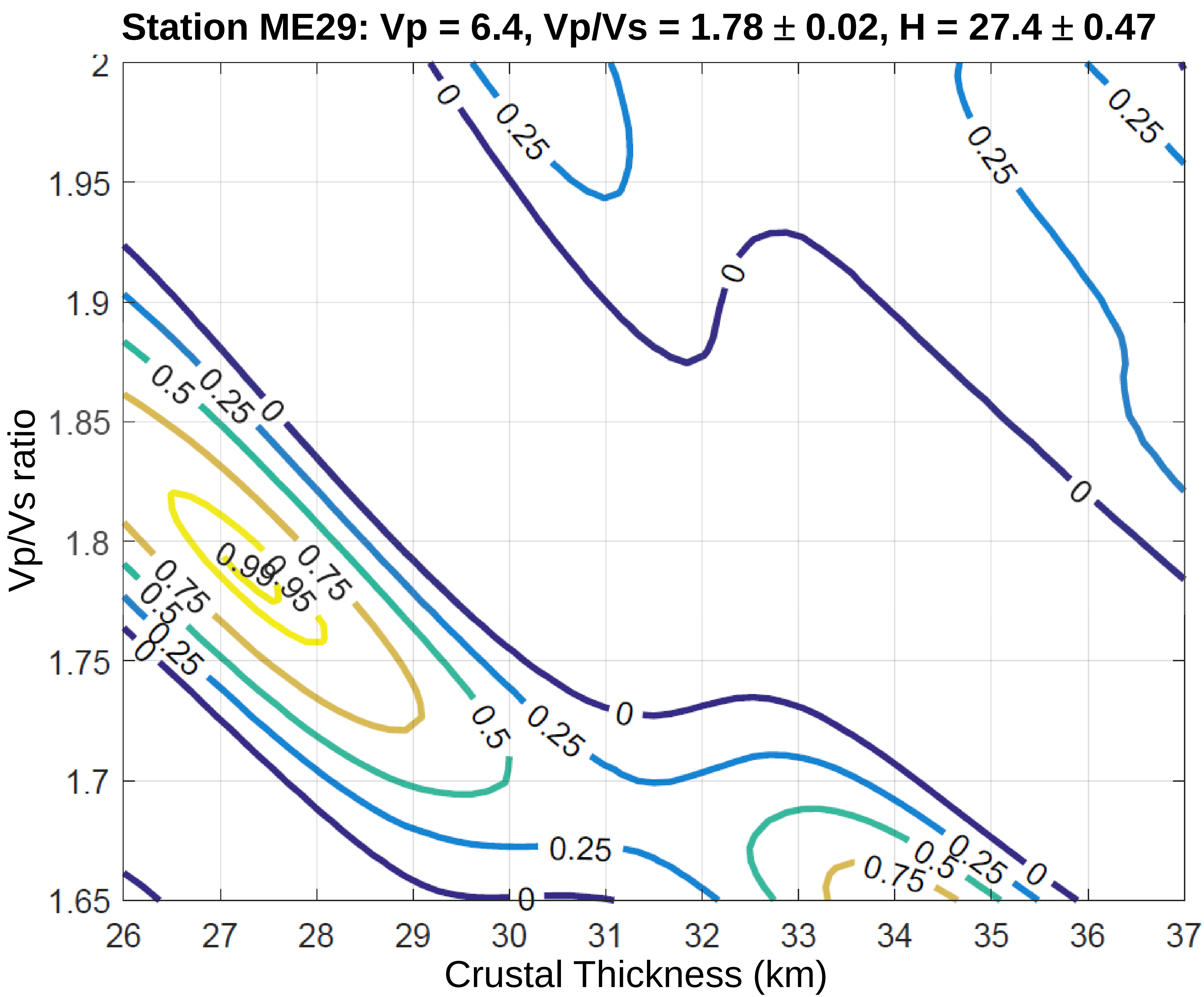
Station ME29: Vp = 6.4, Vp/Vs = 1.78 ± 0.02, H = 27.4 ± 0.47
Vp/Vs ratio
Crustal Thickness (km)
2
1.95
1.9
1.85
1.8
1.75
1.7
1.65
26
27
28
29
30
31
32
33
34
35
36
37
0
0.25
0.5
0.75
0.95
0.99

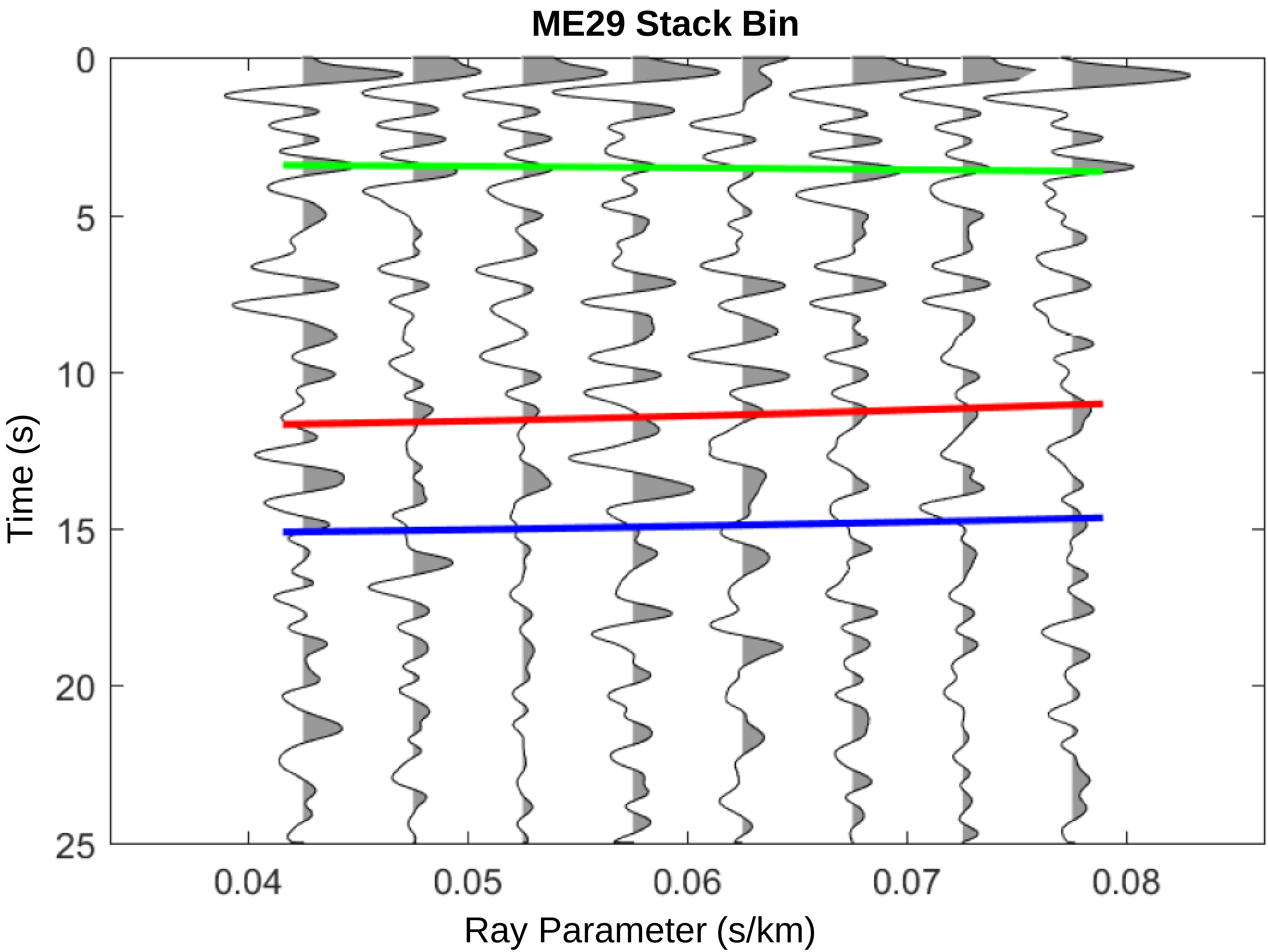
ME29 Stack Bin
Time (s)
0
5
10
15
20
25
0.04
0.05
0.06
0.07
0.08
Ray Parameter (s/km)

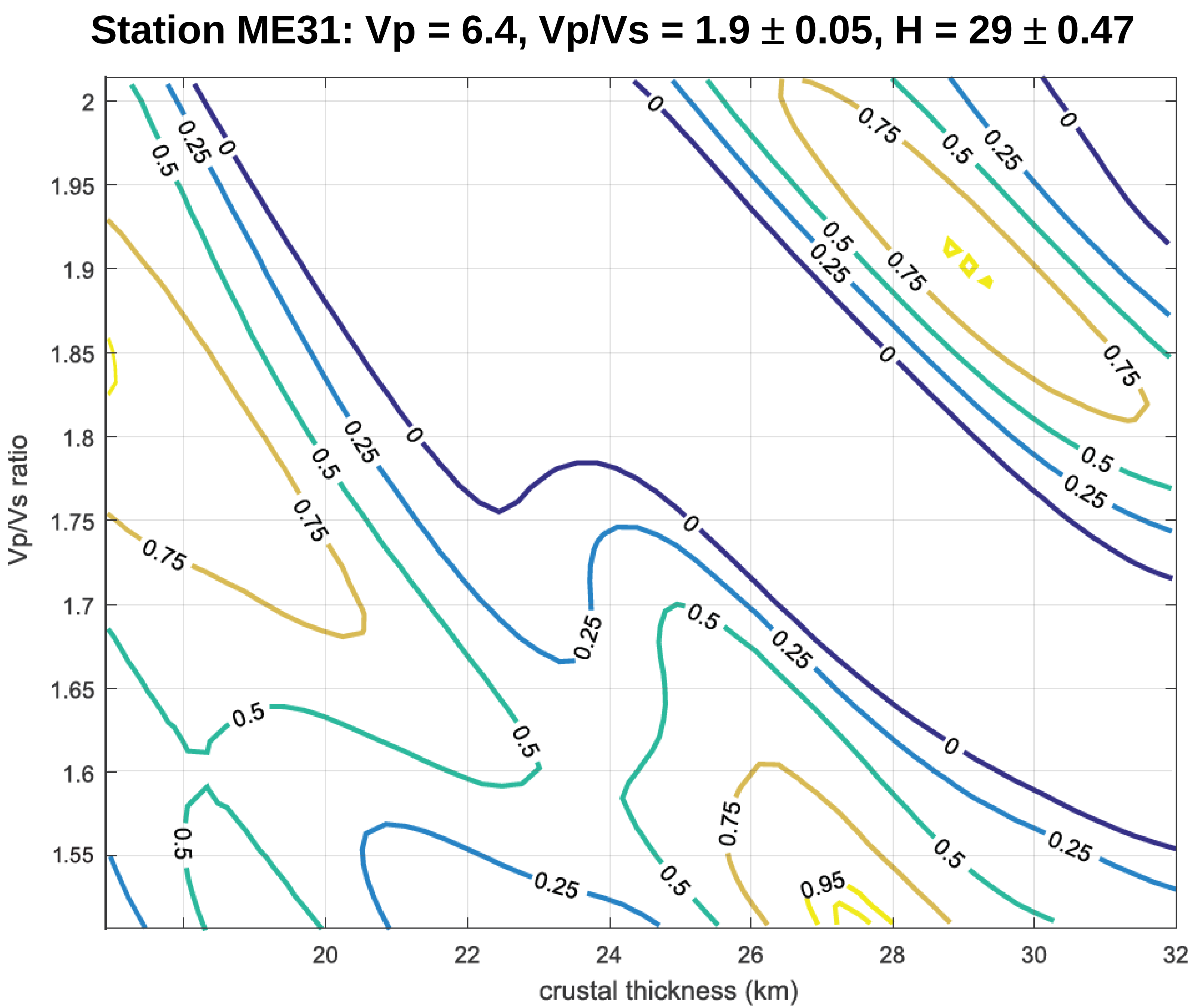

Station ME31: Vp = 6.4, Vp/Vs = 1.9 ± 0.05, H = 29 ± 0.47
Vp/Vs ratio
crustal thickness (km)

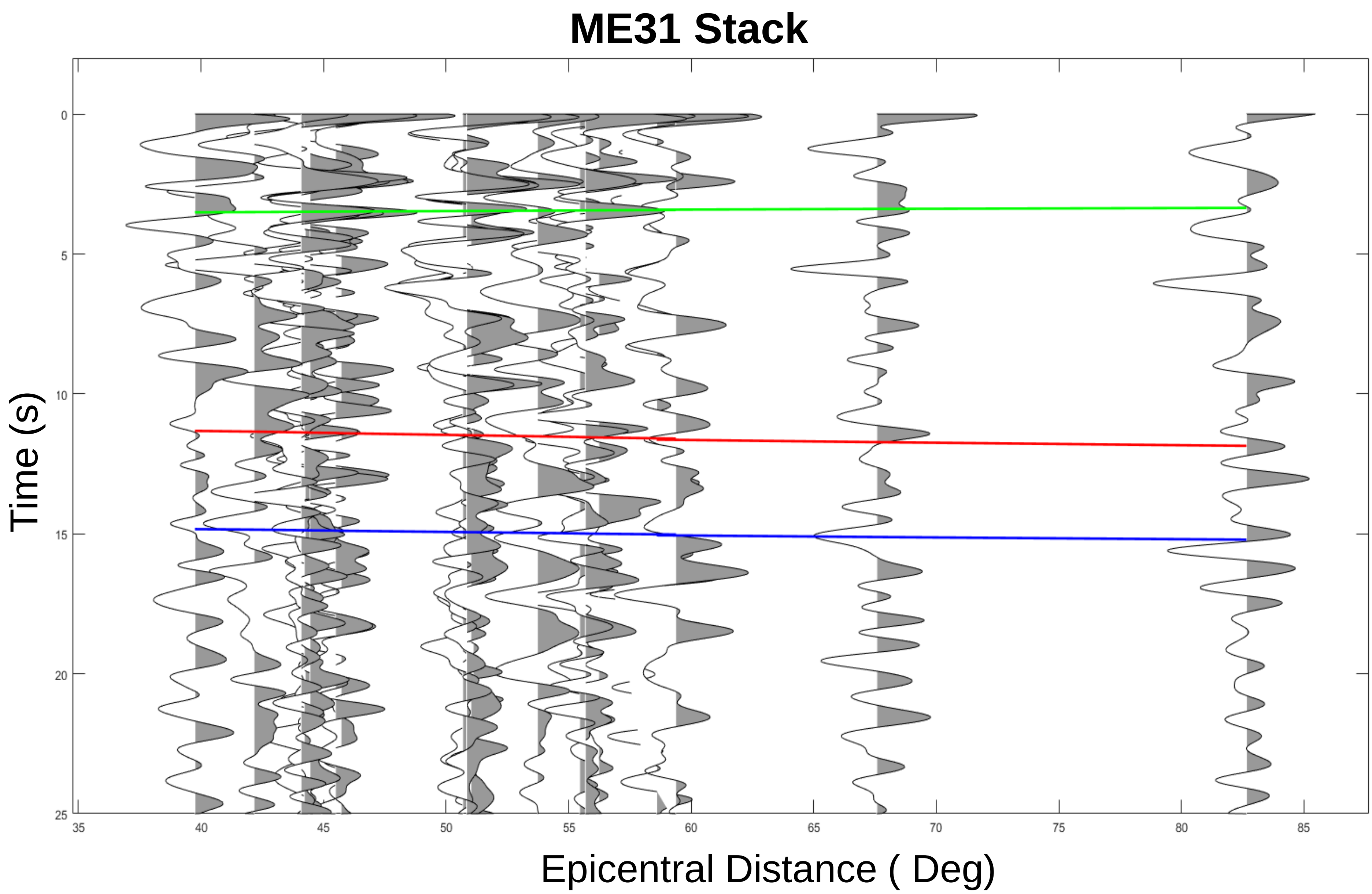

ME31 Stack
Time (s)
0
5
10
15
20
25
35
40
45
50
55
60
65
70
75
80
85
Epicentral Distance (Deg)

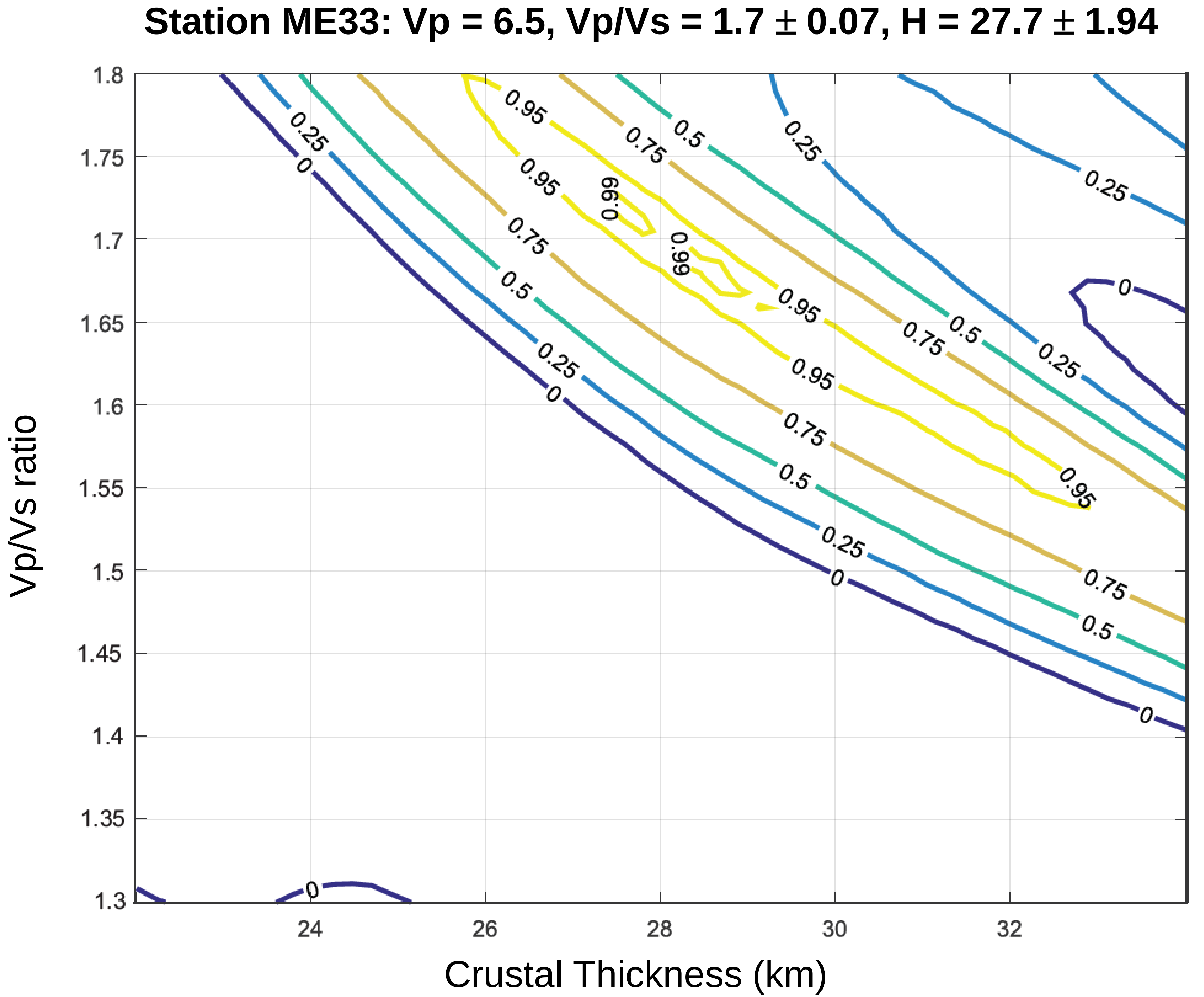

Station ME33: Vp = 6.5, Vp/Vs = 1.7 ± 0.07, H = 27.7 ± 1.94
Vp/Vs ratio
Crustal Thickness (km)
1.8
1.75
1.7
1.65
1.6
1.55
1.5
1.45
1.4
1.35
1.3
24
26
28
30
32
0
0.25
0.5
0.75
0.95
0.99

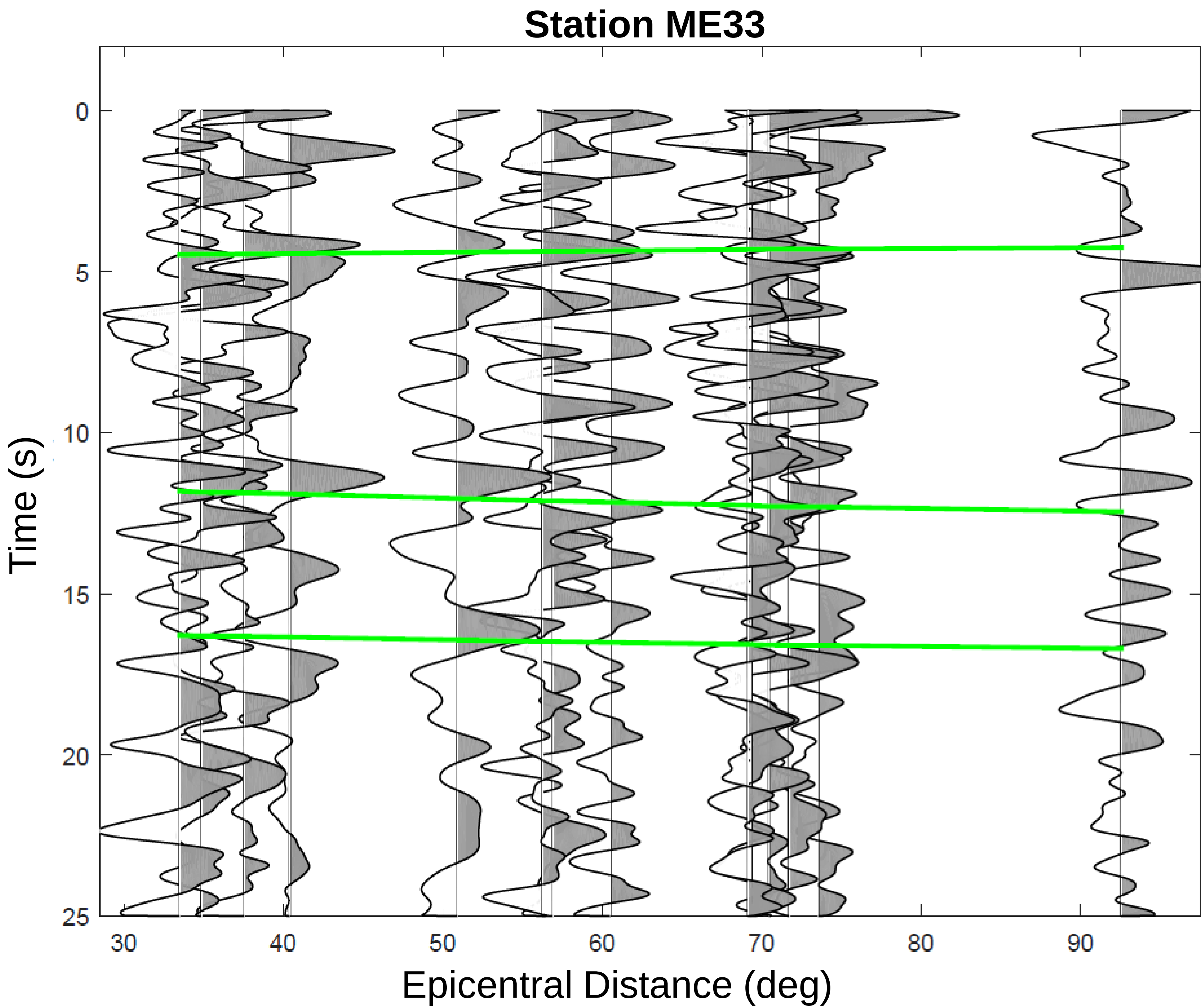
Station ME33
Time (s)
0
5
10
15
20
25
30
40
50
60
70
80
90
Epicentral Distance (deg)

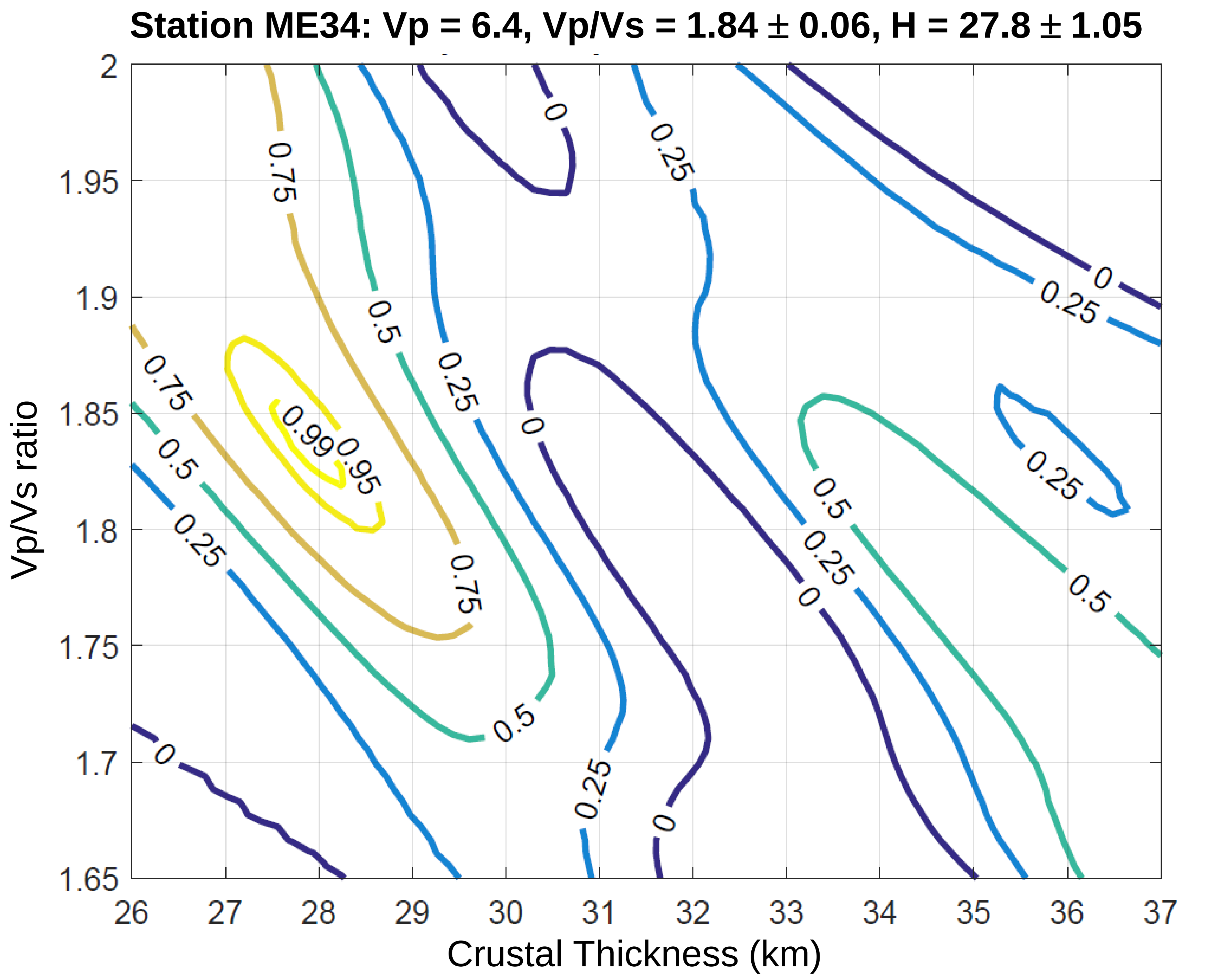
Station ME34: Vp = 6.4, Vp/Vs = 1.84 ± 0.06, H = 27.8 ± 1.05
Vp/Vs ratio
2
1.95
1.9
1.85
1.8
1.75
1.7
1.65
26
27
28
29
30
31
32
33
34
35
36
37
Crustal Thickness (km)
0
0.25
0.5
0.75
0.95
0.99

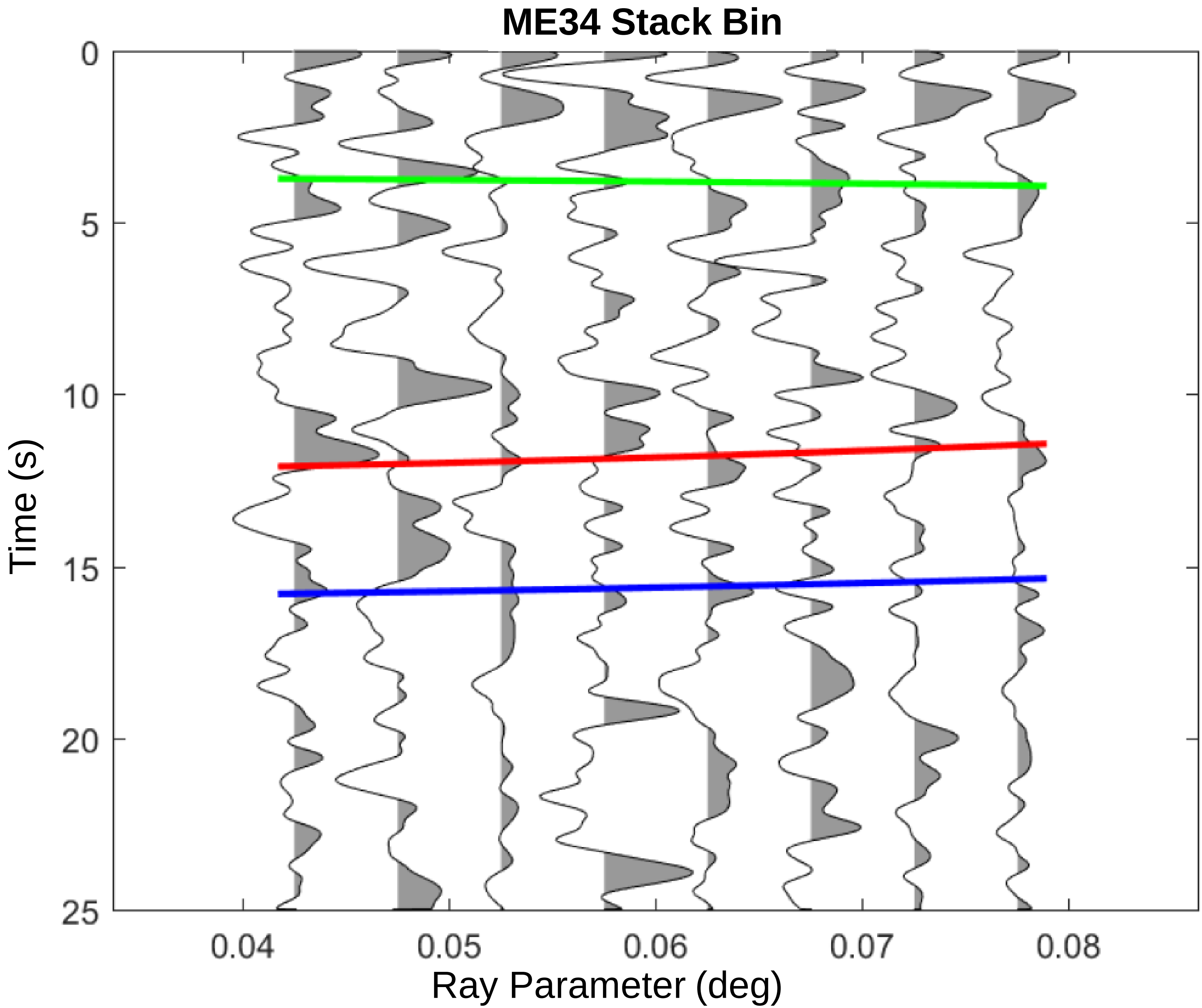
ME34 Stack Bin
Time (s)
0
5
10
15
20
25
0.04
0.05
0.06
0.07
0.08
Ray Parameter (deg)

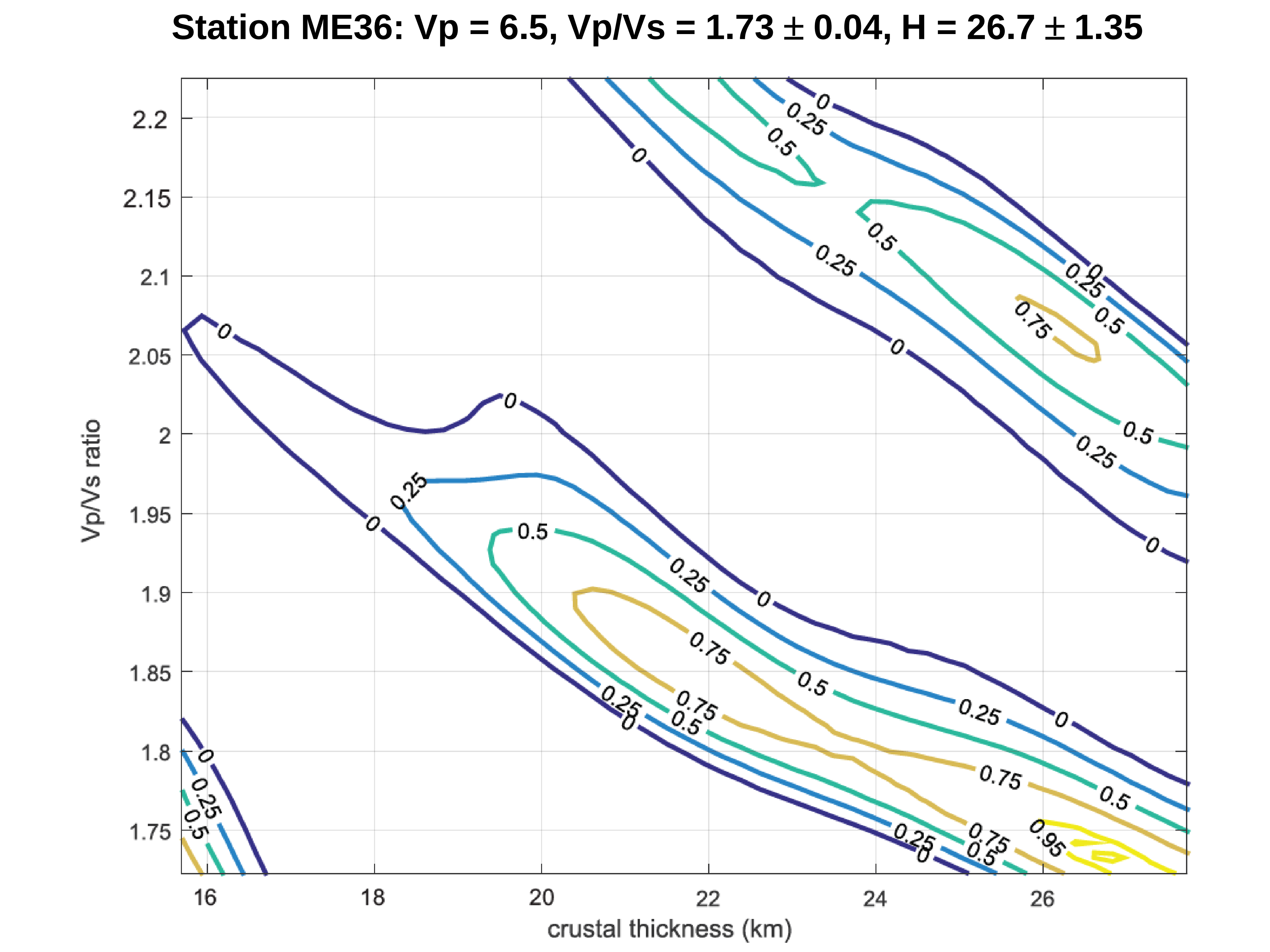
Station ME36: Vp = 6.5, Vp/Vs = 1.73 ± 0.04, H = 26.7 ± 1.35
Vp/Vs ratio
crustal thickness (km)
2.2
2.15
2.1
2.05
2
1.95
1.9
1.85
1.8
1.75
16
18
20
22
24
26
0
0.25
0.5
0.75
0.95

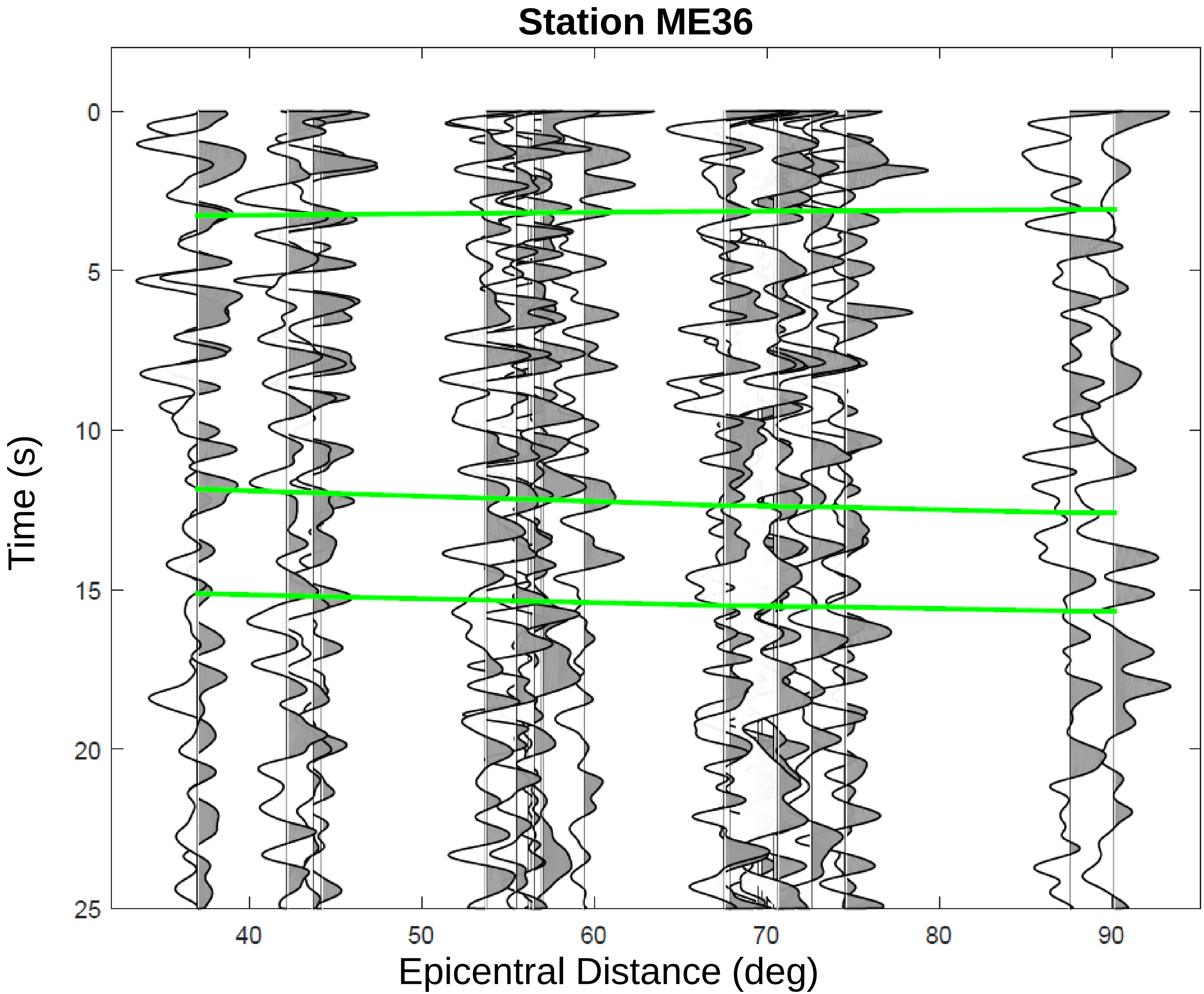

Station ME36
0
5
10
15
20
25
Time (s)
40
50
60
70
80
90
Epicentral Distance (deg)

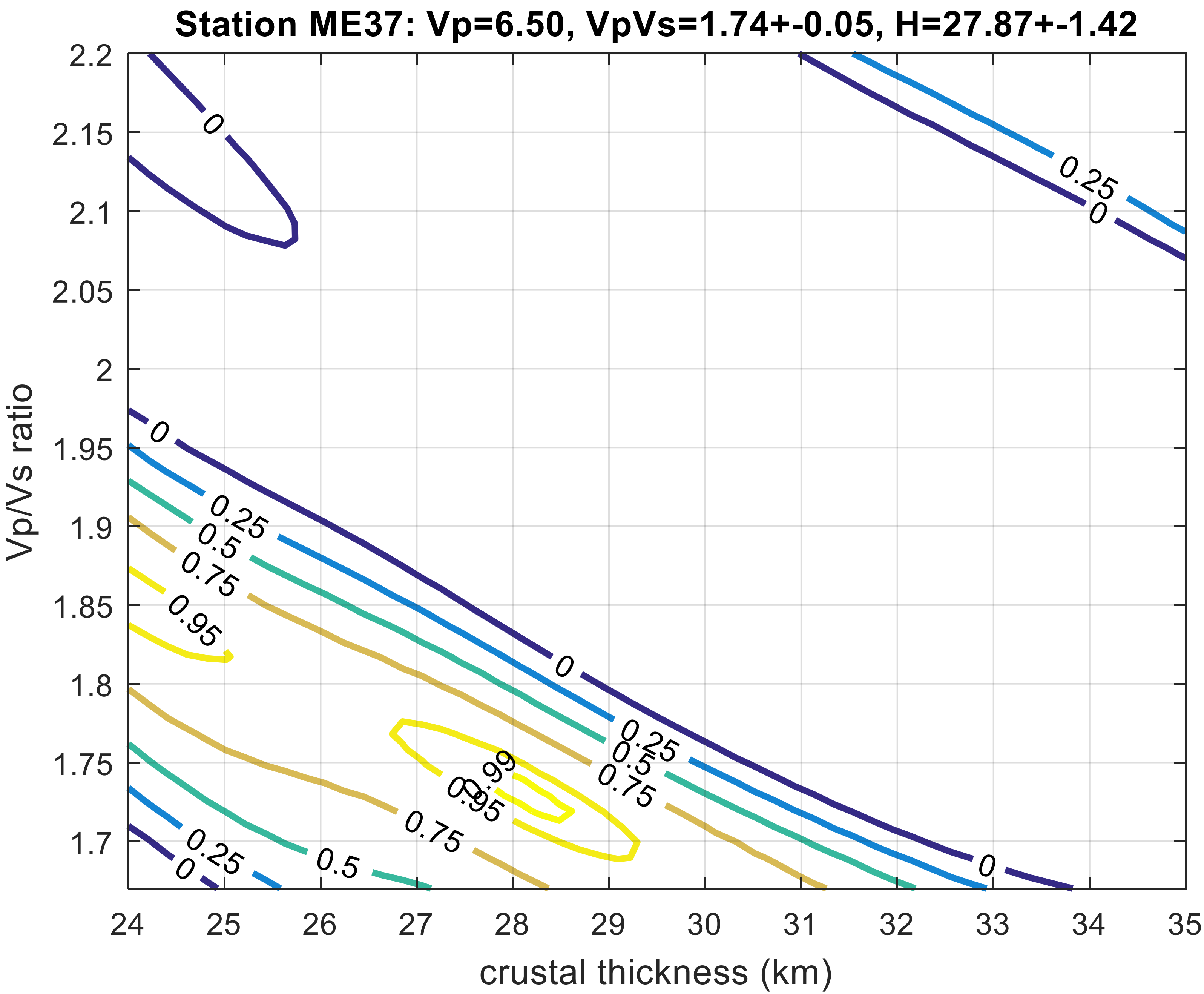

Station ME37: Vp=6.50, VpVs=1.74+-0.05, H=27.87+-1.42
Vp/Vs ratio
crustal thickness (km)
2.2
2.15
2.1
2.05
2
1.95
1.9
1.85
1.8
1.75
1.7
24
25
26
27
28
29
30
31
32
33
34
35
0
0.25
0.5
0.75
0.95
0.99

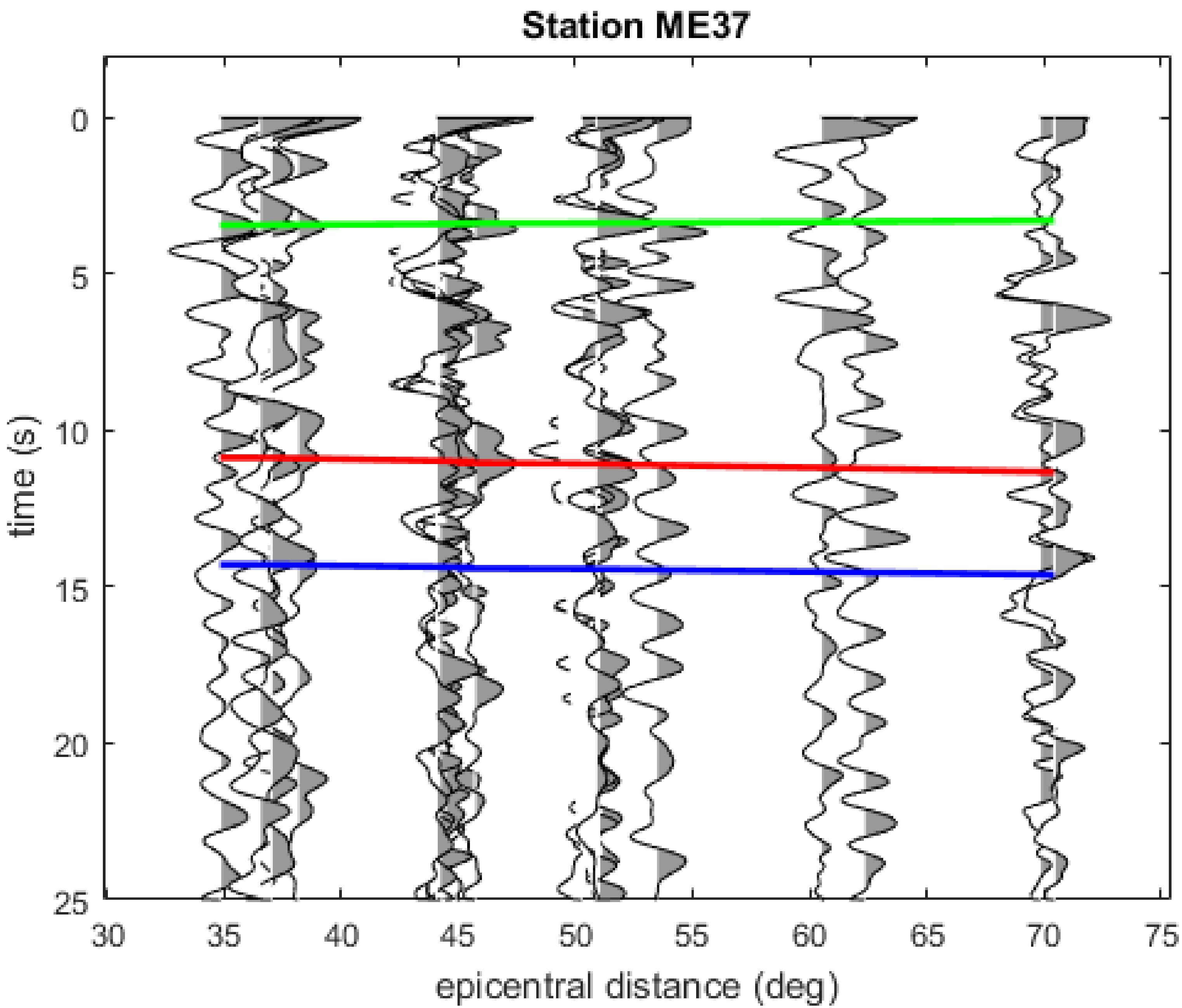
Station ME37
time (s)
epicentral distance (deg)
0
5
10
15
20
25
30
35
40
45
50
55
60
65
70
75

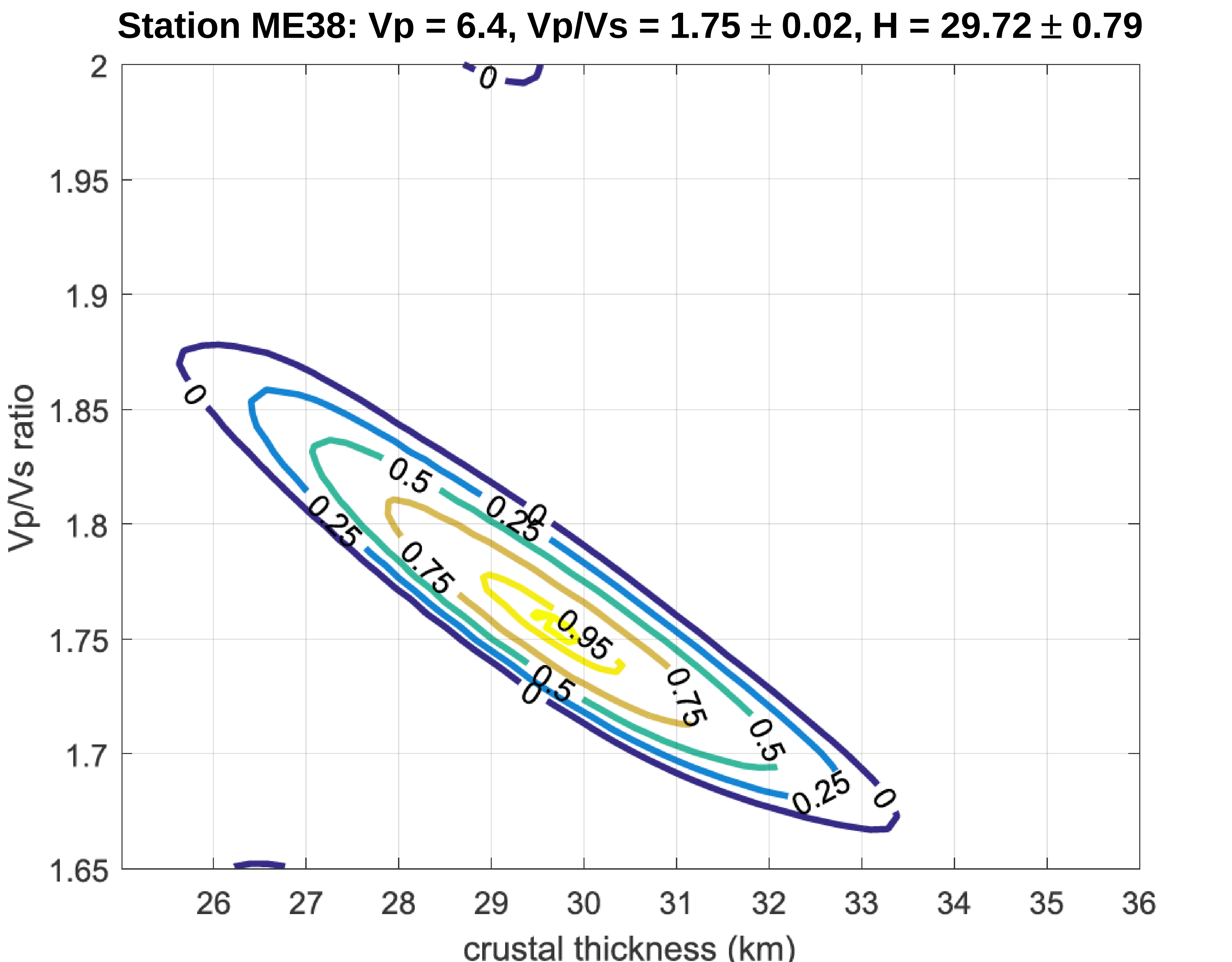

Station ME38: Vp = 6.4, Vp/Vs = 1.75 ± 0.02, H = 29.72 ± 0.79
Vp/Vs ratio
crustal thickness (km)
2
1.95
1.9
1.85
1.8
1.75
1.7
1.65
26
27
28
29
30
31
32
33
34
35
36
0
0.25
0.5
0.75
0.95

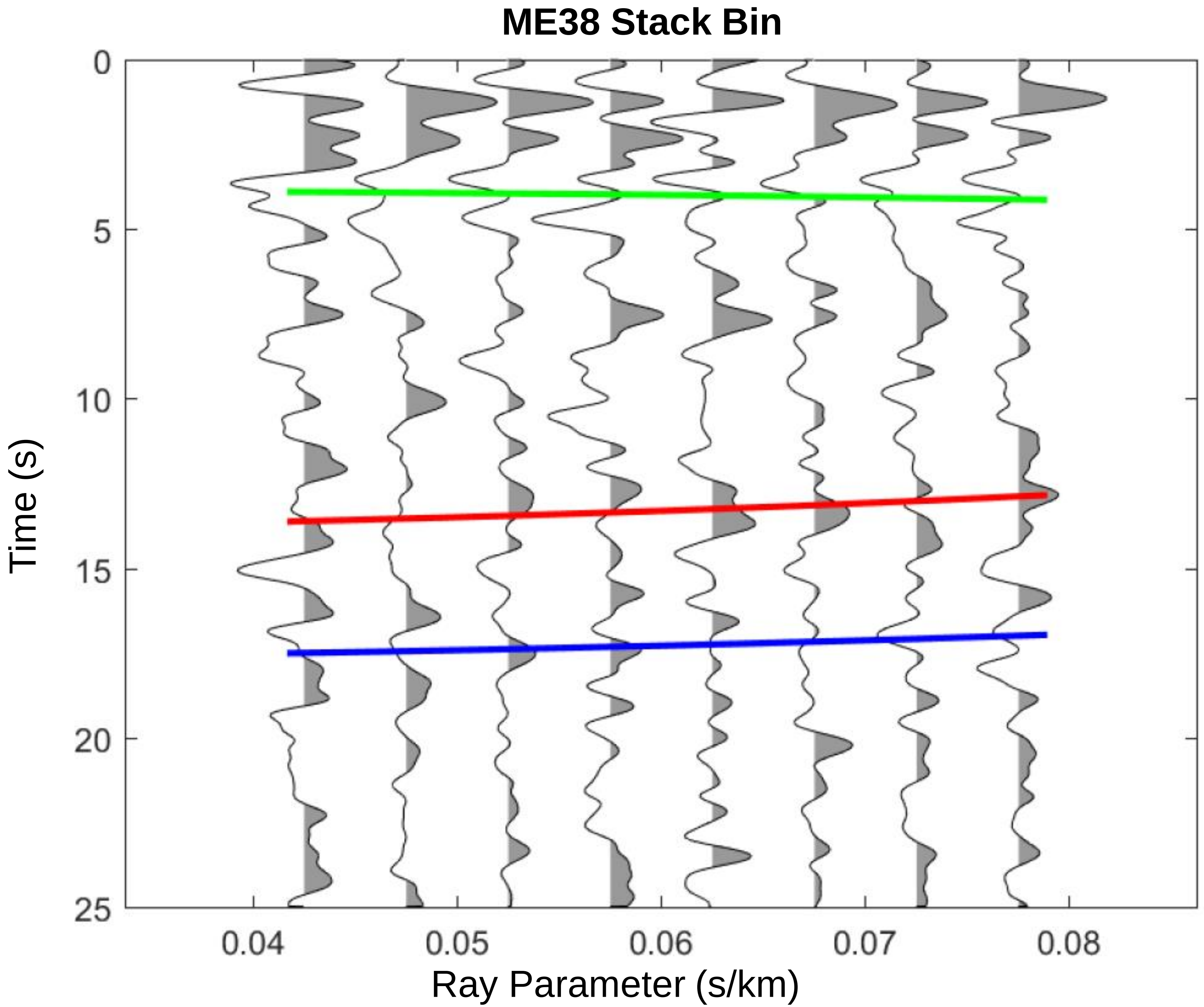
ME38 Stack Bin
Time (s)
0
5
10
15
20
25
0.04
0.05
0.06
0.07
0.08
Ray Parameter (s/km)

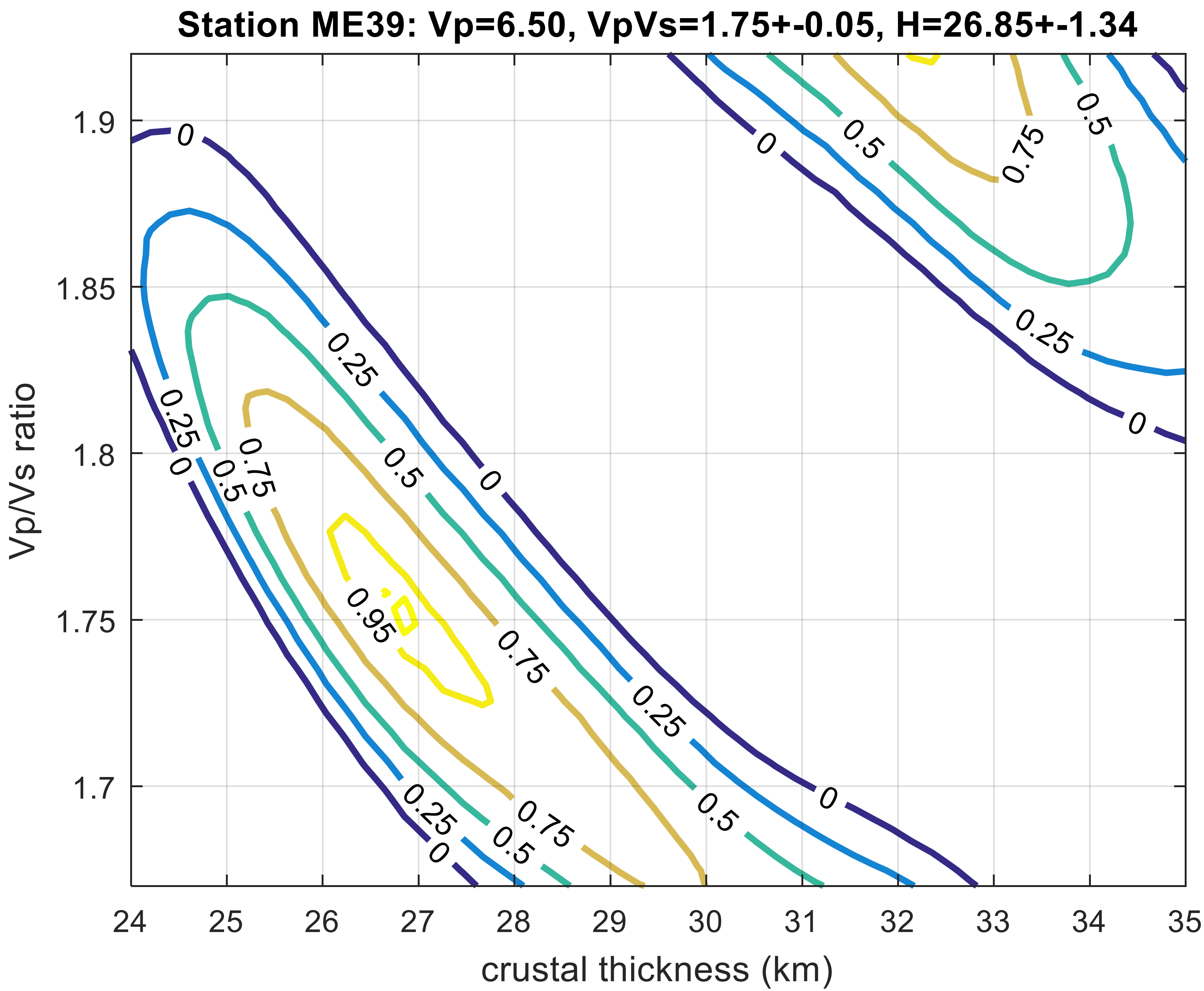
Station ME39: Vp=6.50, VpVs=1.75+-0.05, H=26.85+-1.34
Vp/Vs ratio
crustal thickness (km)
1.9
1.85
1.8
1.75
1.7
24
25
26
27
28
29
30
31
32
33
34
35
0
0.25
0.5
0.75
0.95

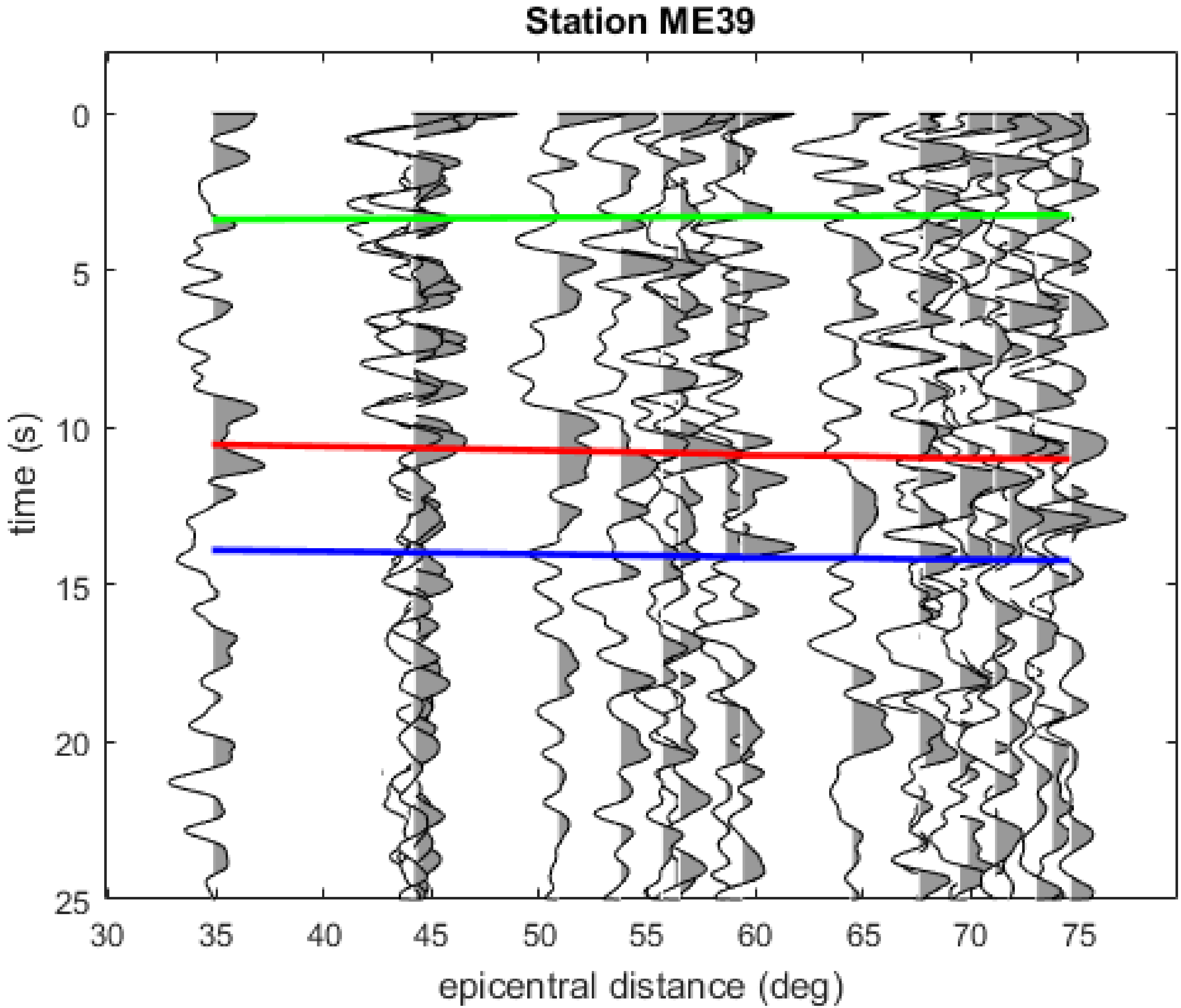

Station ME39
time (s)
0
5
10
15
20
25
30
35
40
45
50
55
60
65
70
75
epicentral distance (deg)

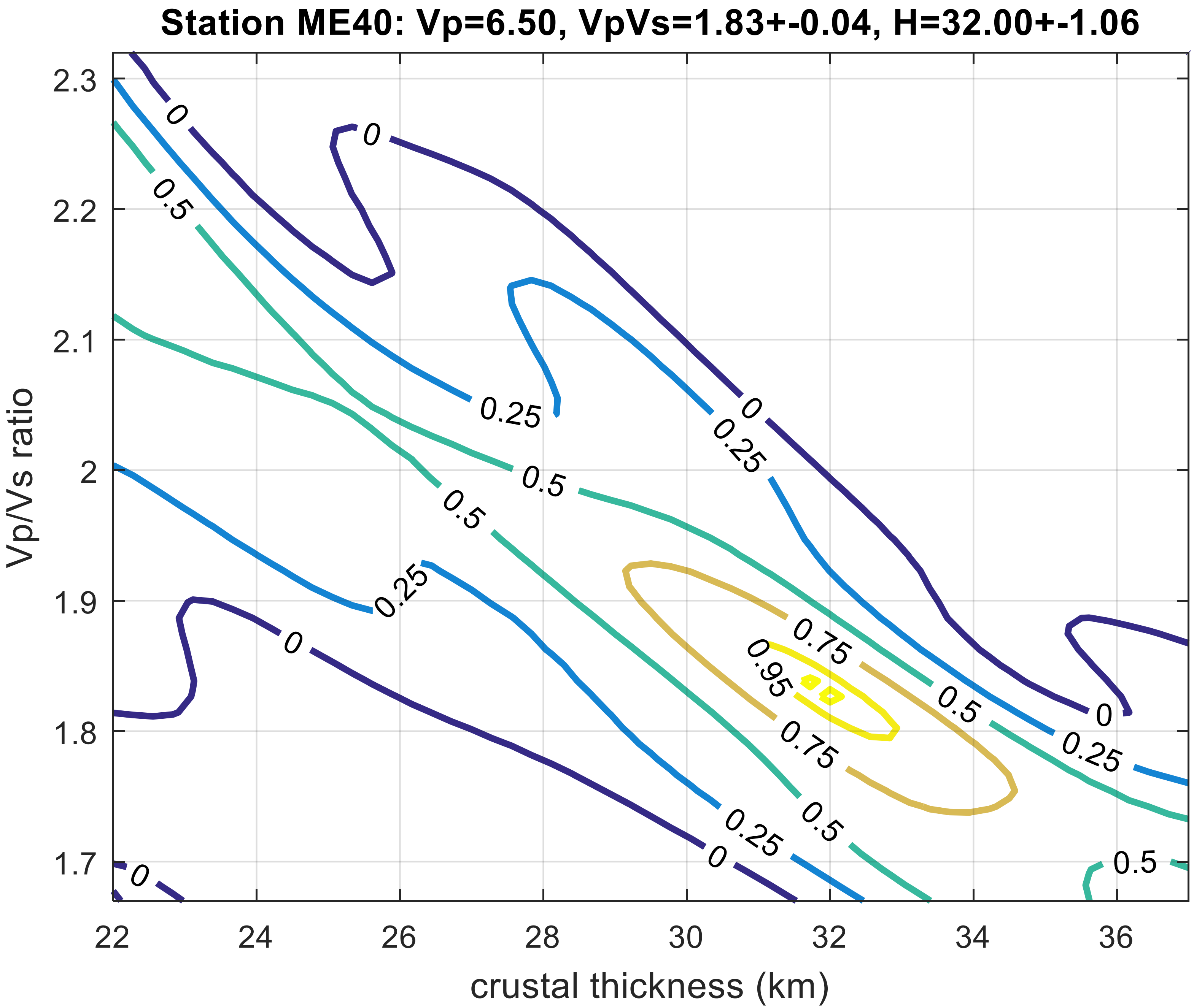
Station ME40: Vp=6.50, VpVs=1.83+-0.04, H=32.00+-1.06
Vp/Vs ratio
crustal thickness (km)
2.3
2.2
2.1
2
1.9
1.8
1.7
22
24
26
28
30
32
34
36
0
0.25
0.5
0.75
0.95

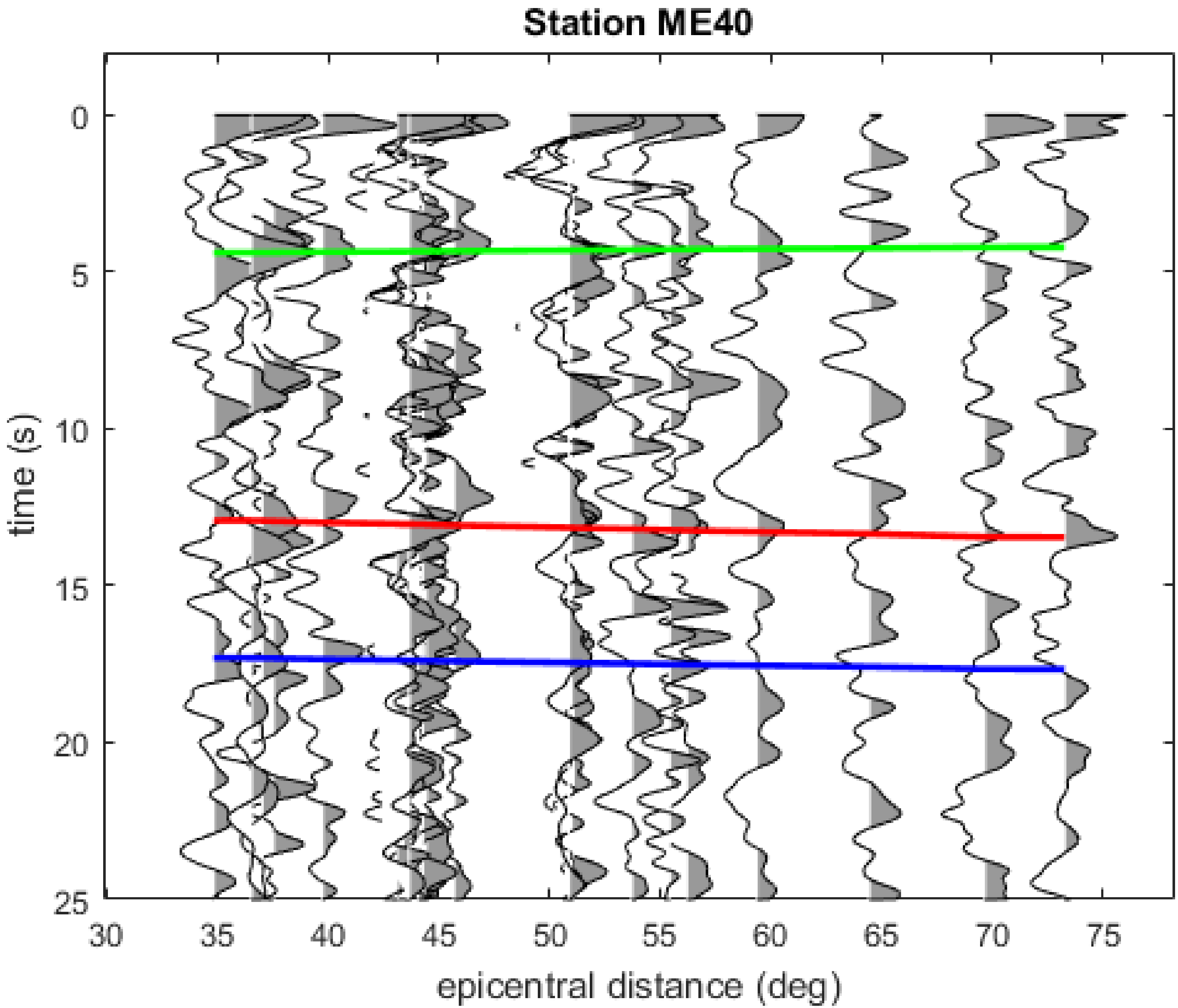

Station ME40
time (s)
0
5
10
15
20
25
30
35
40
45
50
55
60
65
70
75
epicentral distance (deg)

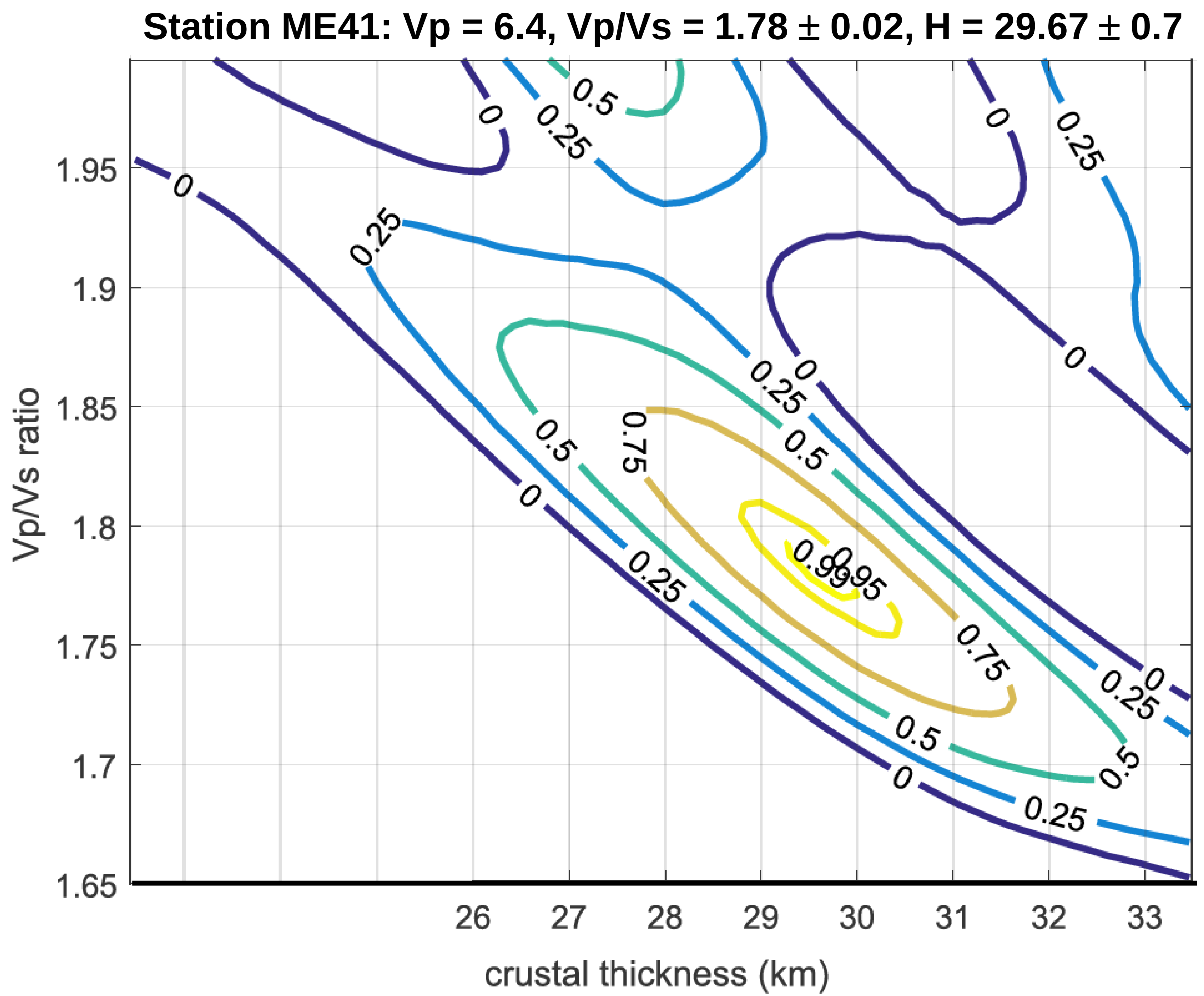
Station ME41: Vp = 6.4, Vp/Vs = 1.78 ± 0.02, H = 29.67 ± 0.7
Vp/Vs ratio
1.95
1.9
1.85
1.8
1.75
1.7
1.65
26
27
28
29
30
31
32
33
crustal thickness (km)
0
0.25
0.5
0.75
0.95
0.99

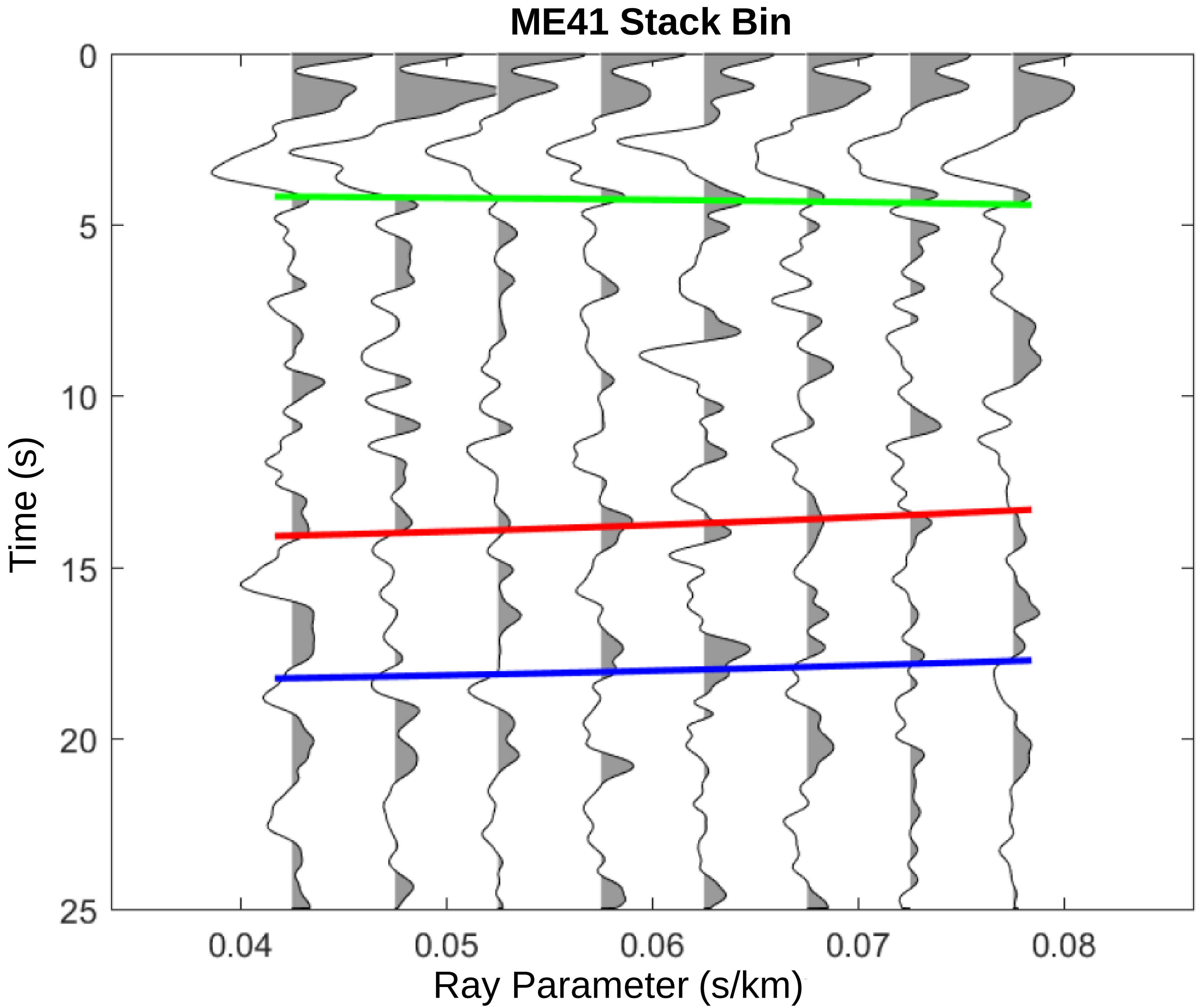
ME41 Stack Bin
Time (s)
0
5
10
15
20
25
0.04
0.05
0.06
0.07
0.08
Ray Parameter (s/km)

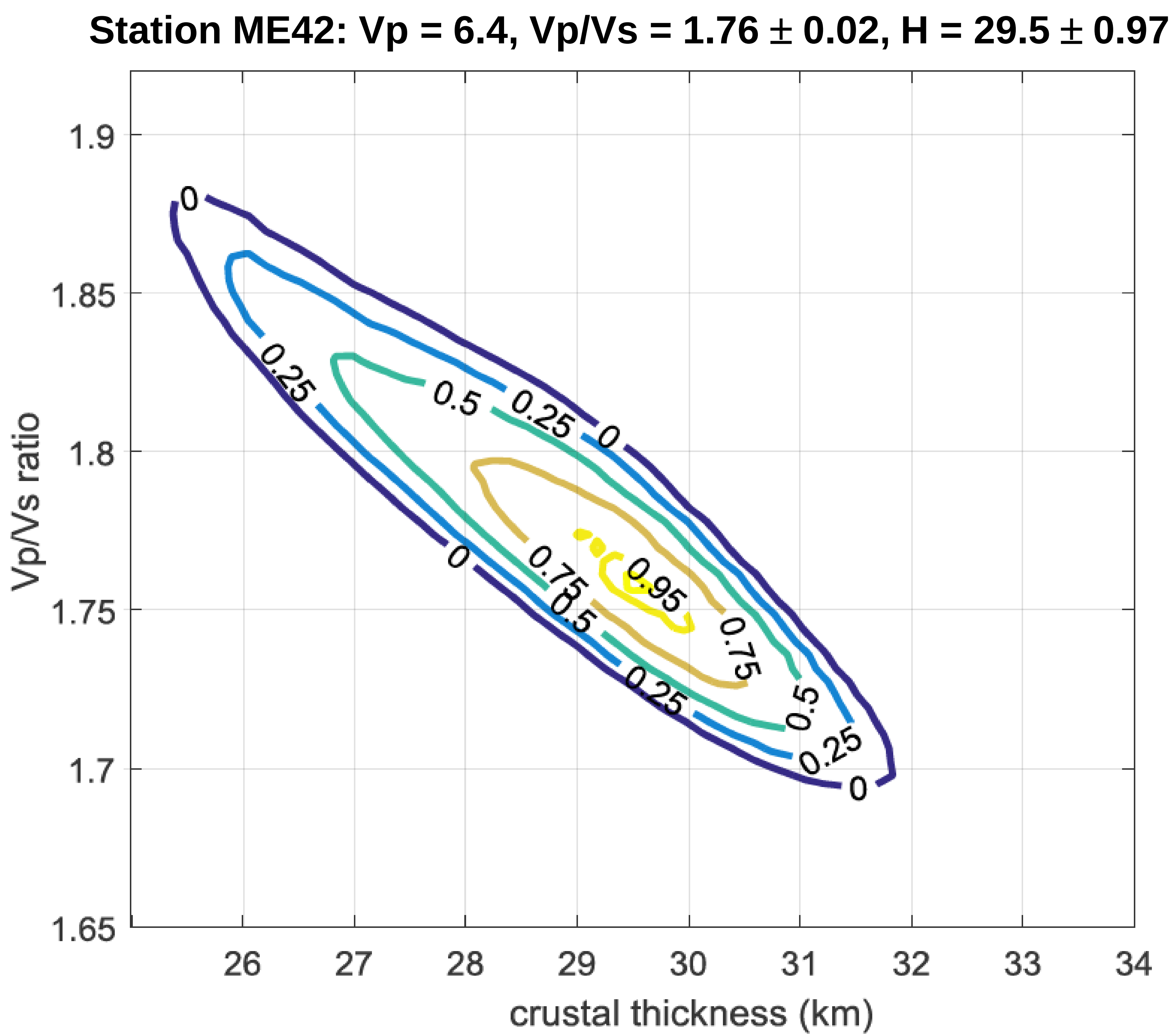
Station ME42: Vp = 6.4, Vp/Vs = 1.76 ± 0.02, H = 29.5 ± 0.97
Vp/Vs ratio
1.9
1.85
1.8
1.75
1.7
1.65
26
27
28
29
30
31
32
33
34
crustal thickness (km)
0
0.25
0.5
0.75
0.95

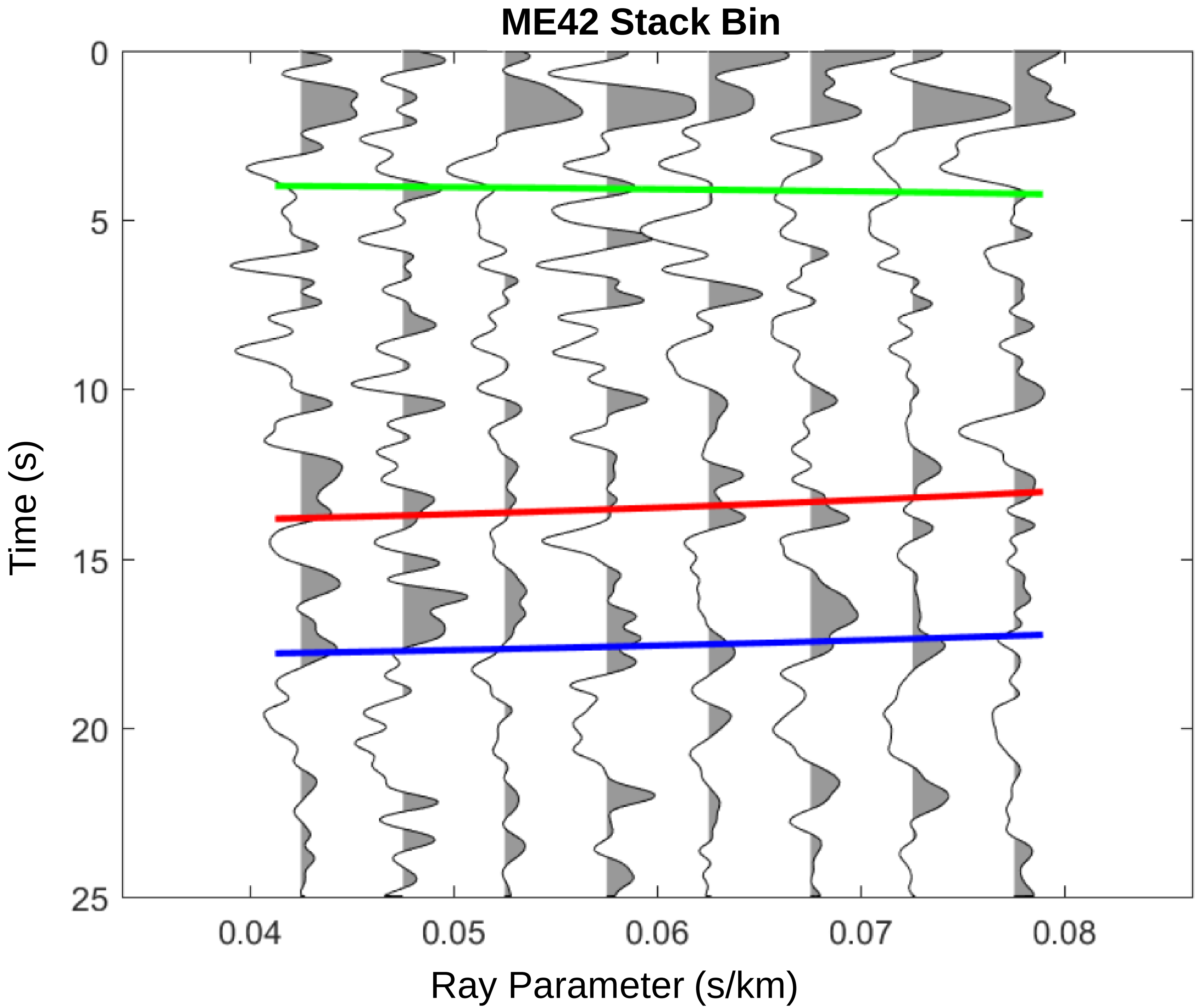

ME42 Stack Bin
Time (s)
0
5
10
15
20
25
0.04
0.05
0.06
0.07
0.08
Ray Parameter (s/km)

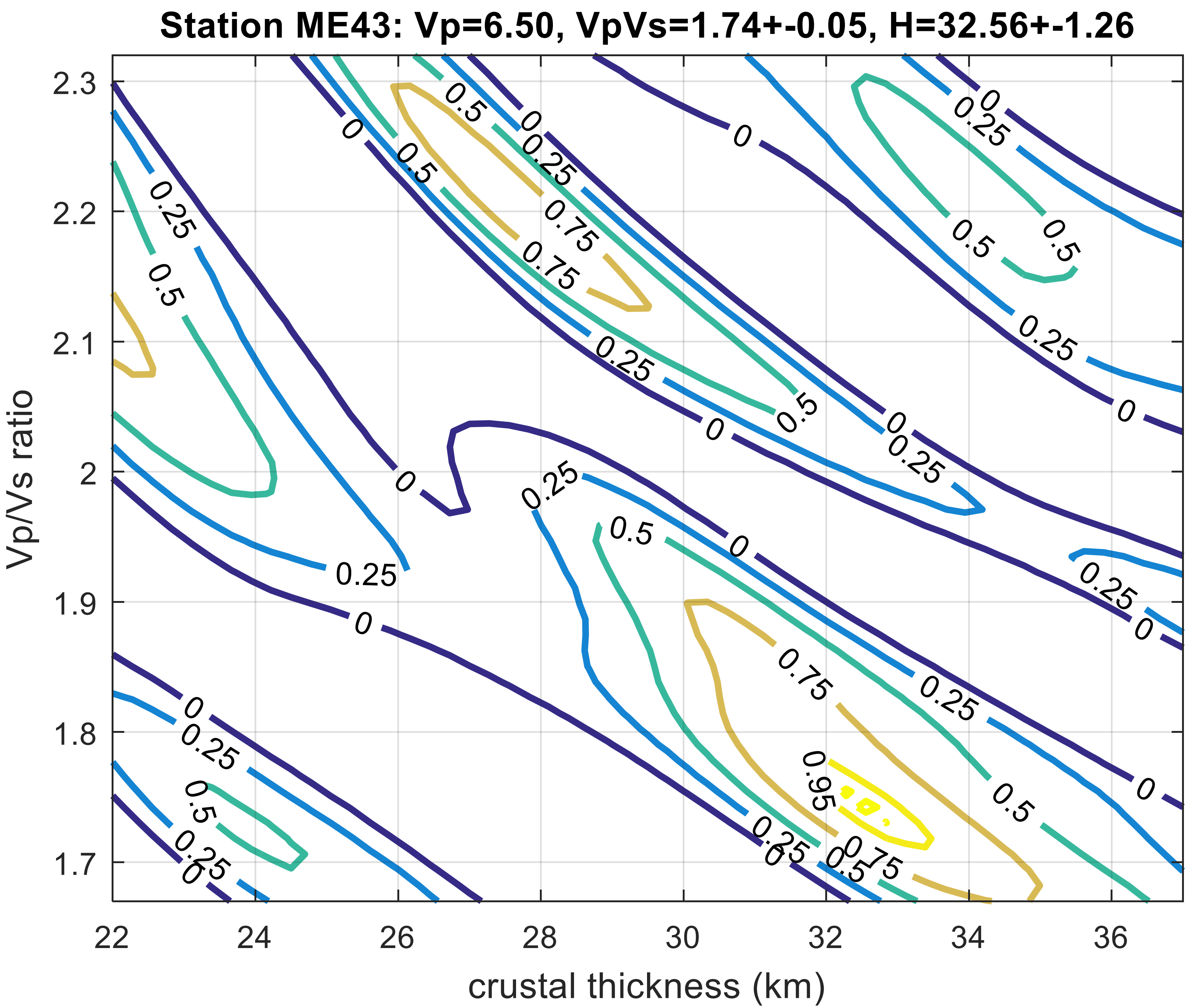

Station ME43: Vp=6.50, VpVs=1.74+-0.05, H=32.56+-1.26
Vp/Vs ratio
crustal thickness (km)
2.3
2.2
2.1
2
1.9
1.8
1.7
22
24
26
28
30
32
34
36
0
0.25
0.5
0.75
0.95

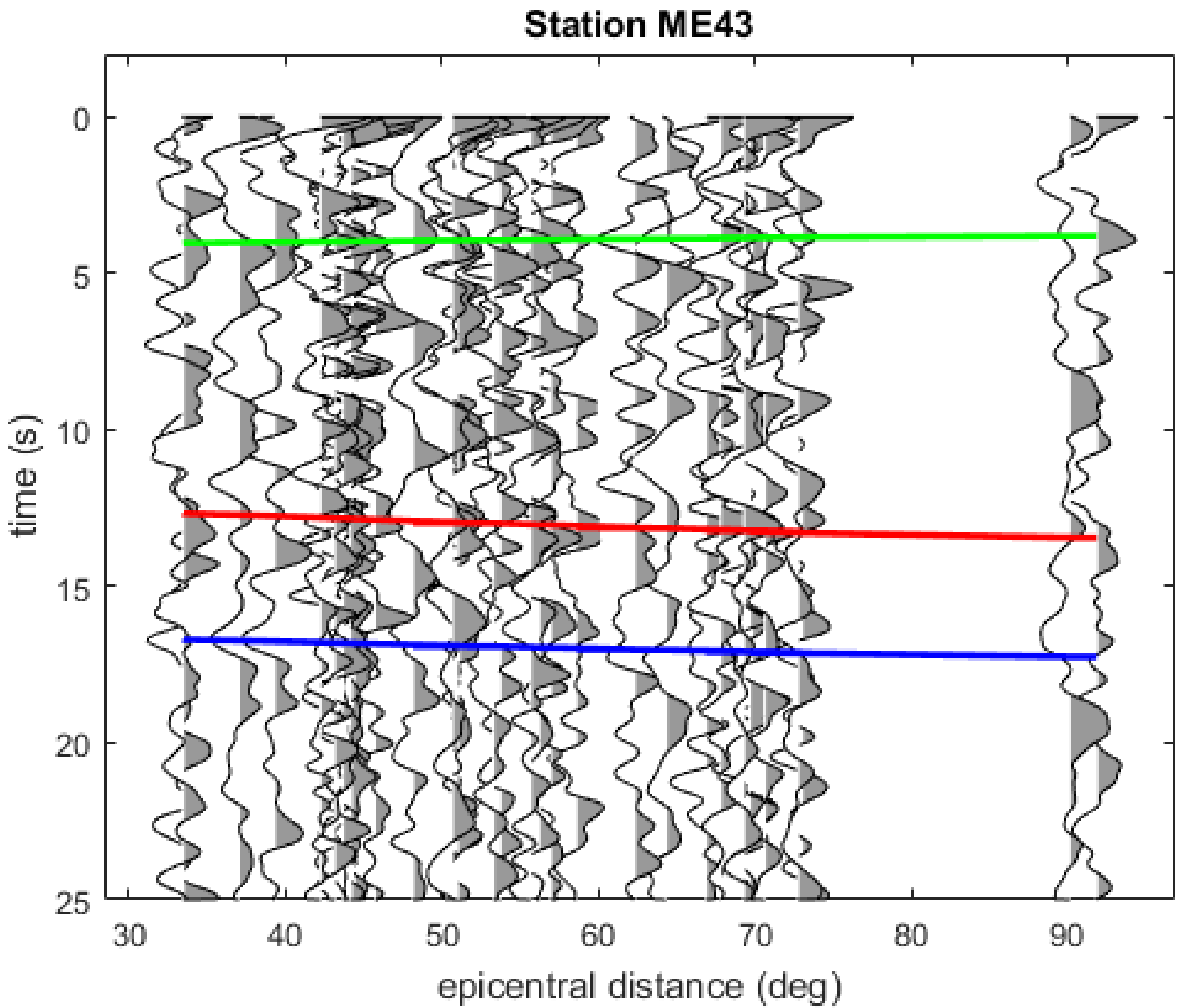
Station ME43
time (s)
0
5
10
15
20
25
30
40
50
60
70
80
90
epicentral distance (deg)

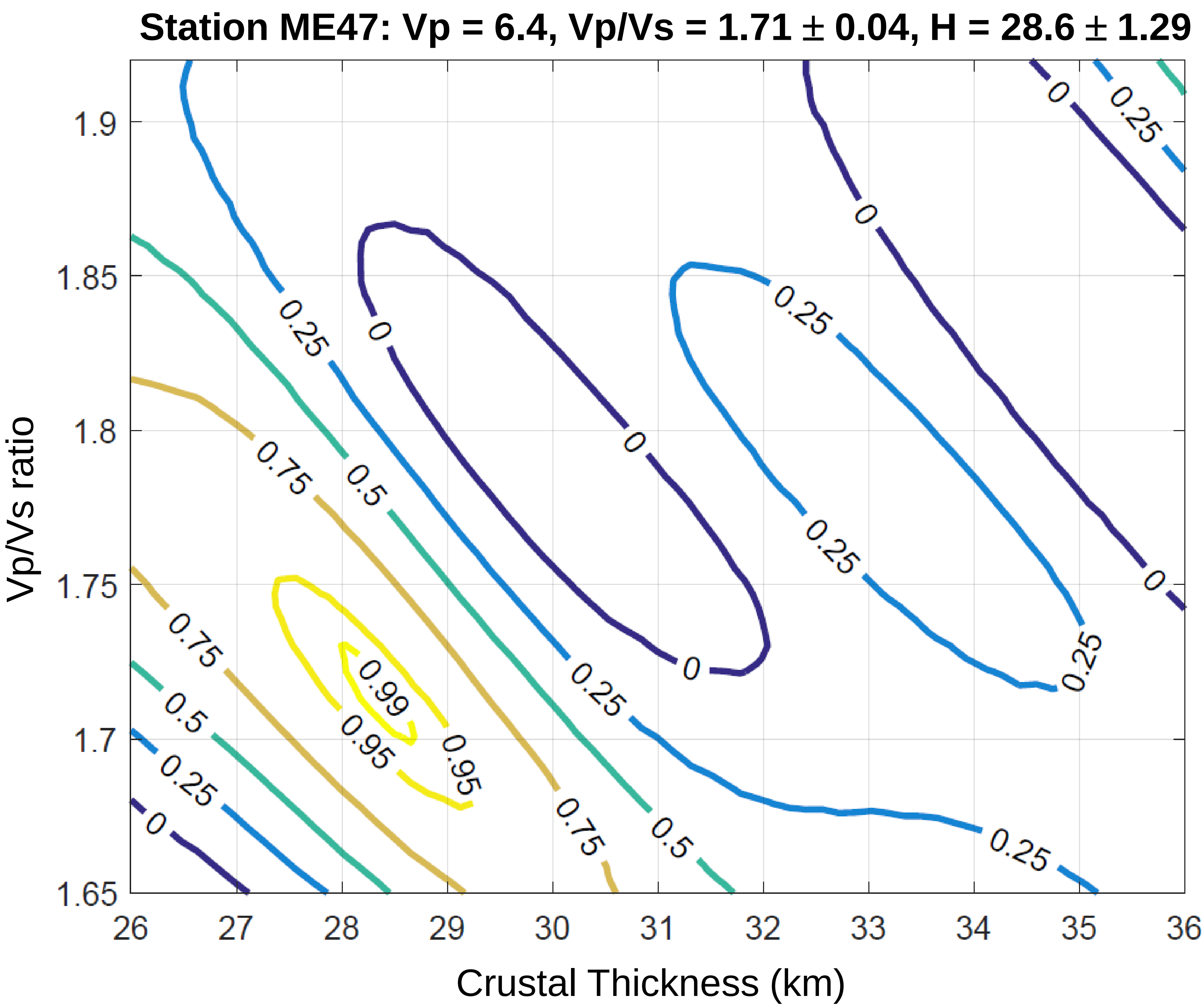
Station ME47: Vp = 6.4, Vp/Vs = 1.71 ± 0.04, H = 28.6 ± 1.29
Vp/Vs ratio
Crustal Thickness (km)
1.9
1.85
1.8
1.75
1.7
1.65
26
27
28
29
30
31
32
33
34
35
36
0
0.25
0.5
0.75
0.95
0.99

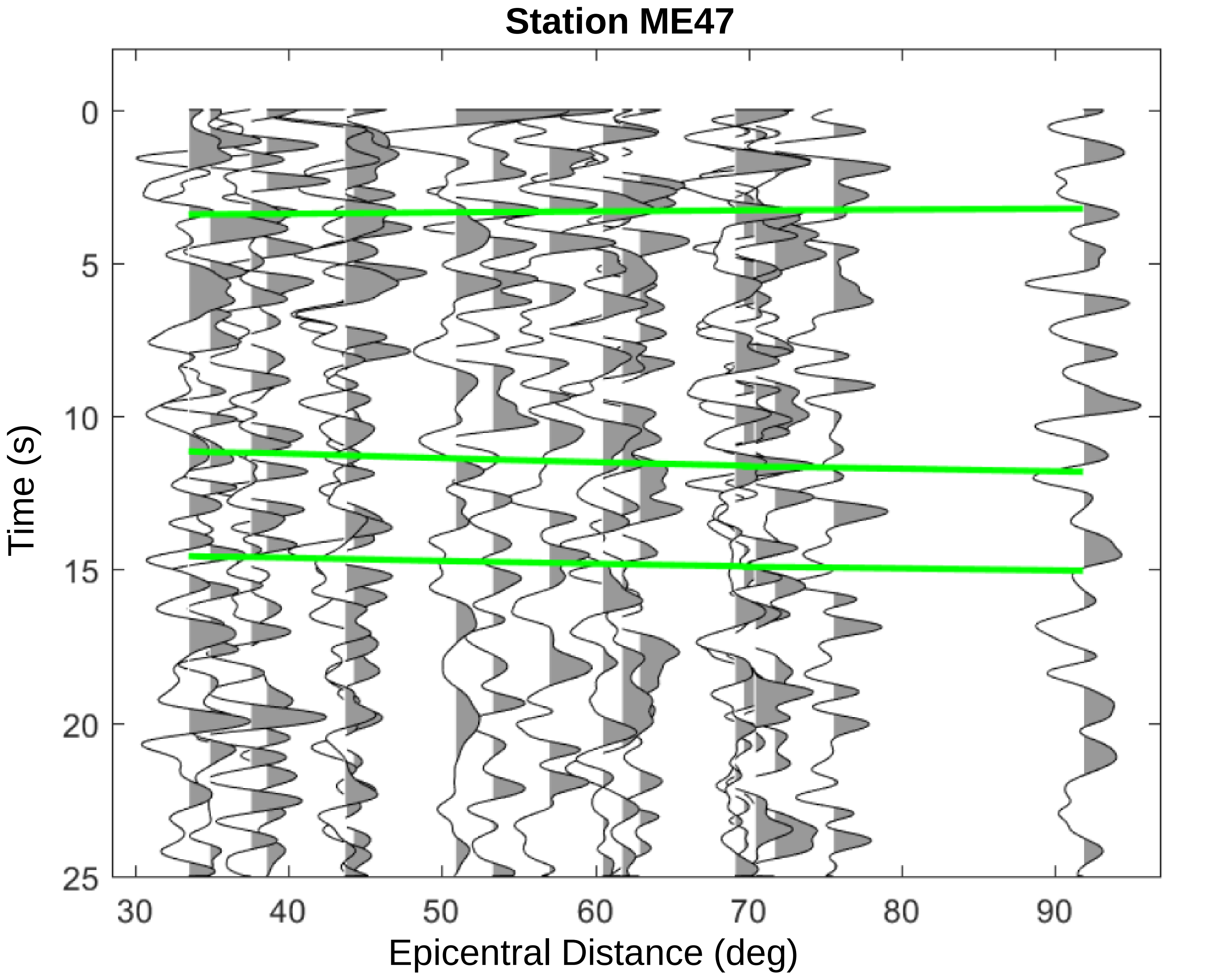
Station ME47
Time (s)
0
5
10
15
20
25
30
40
50
60
70
80
90
Epicentral Distance (deg)

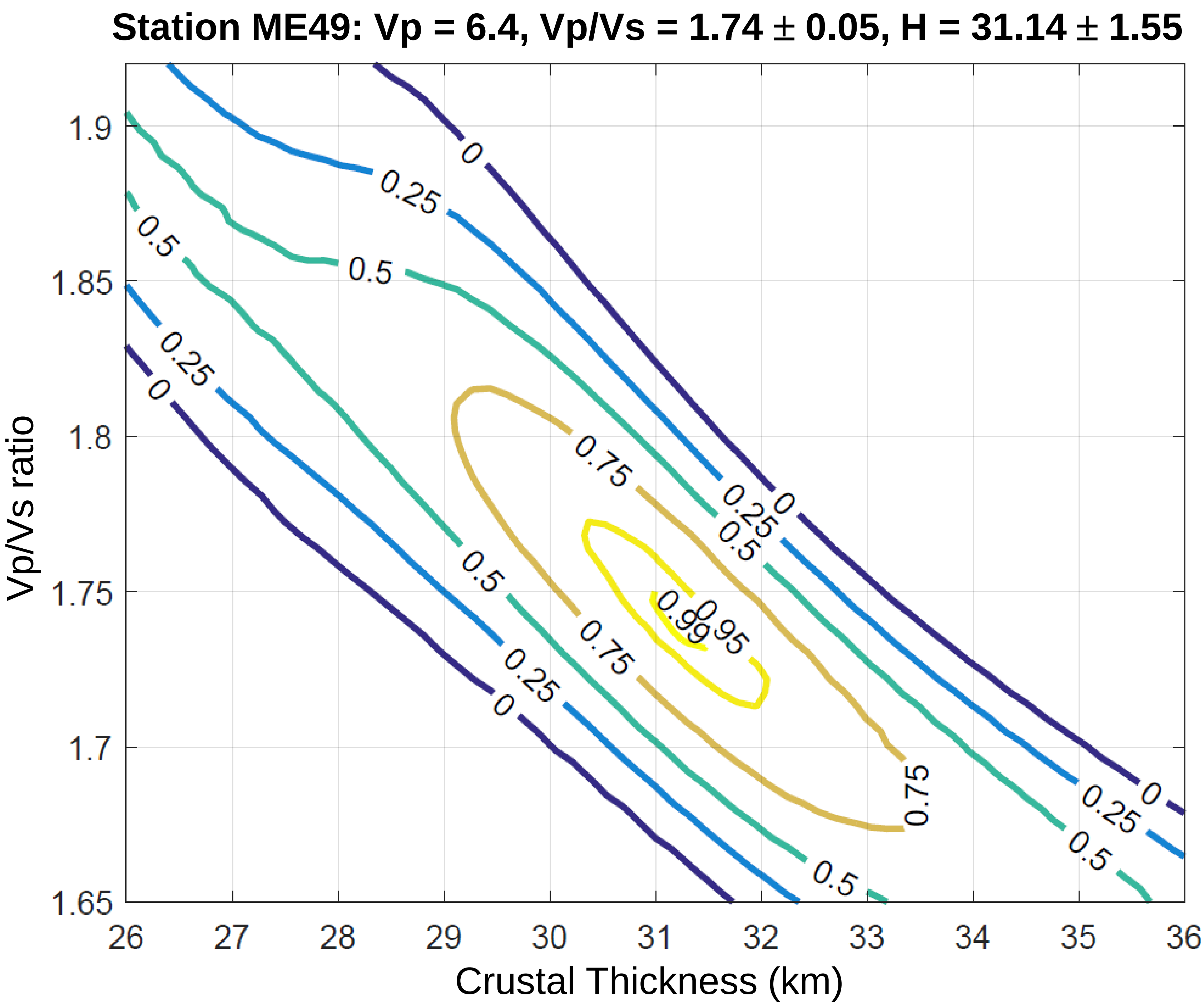
Station ME49: Vp = 6.4, Vp/Vs = 1.74 ± 0.05, H = 31.14 ± 1.55
Vp/Vs ratio
1.9
1.85
1.8
1.75
1.7
1.65
26
27
28
29
30
31
32
33
34
35
36
Crustal Thickness (km)
0
0.25
0.5
0.75
0.95
0.99

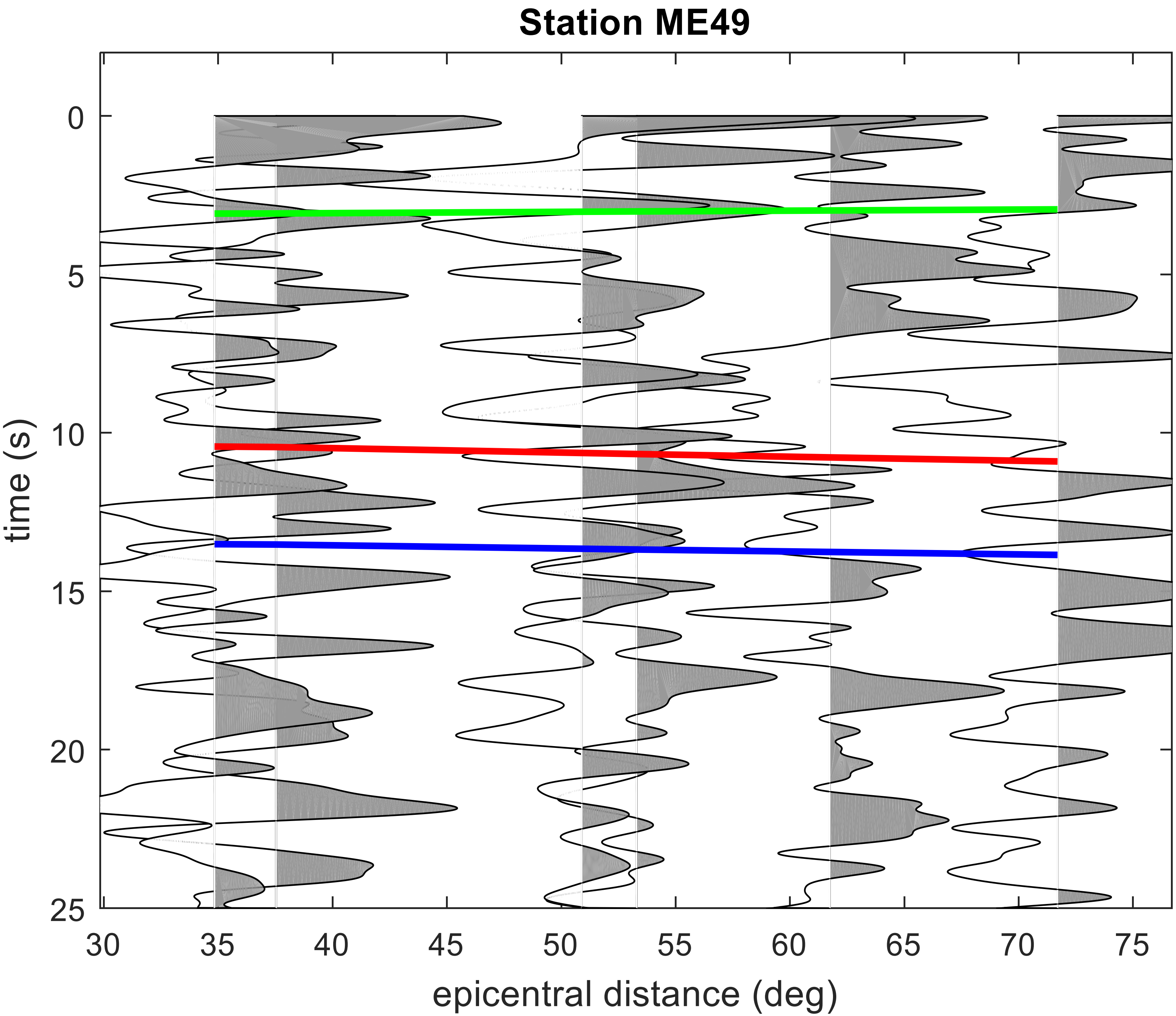

Station ME49
time (s)
0
5
10
15
20
25
epicentral distance (deg)
30
35
40
45
50
55
60
65
70
75

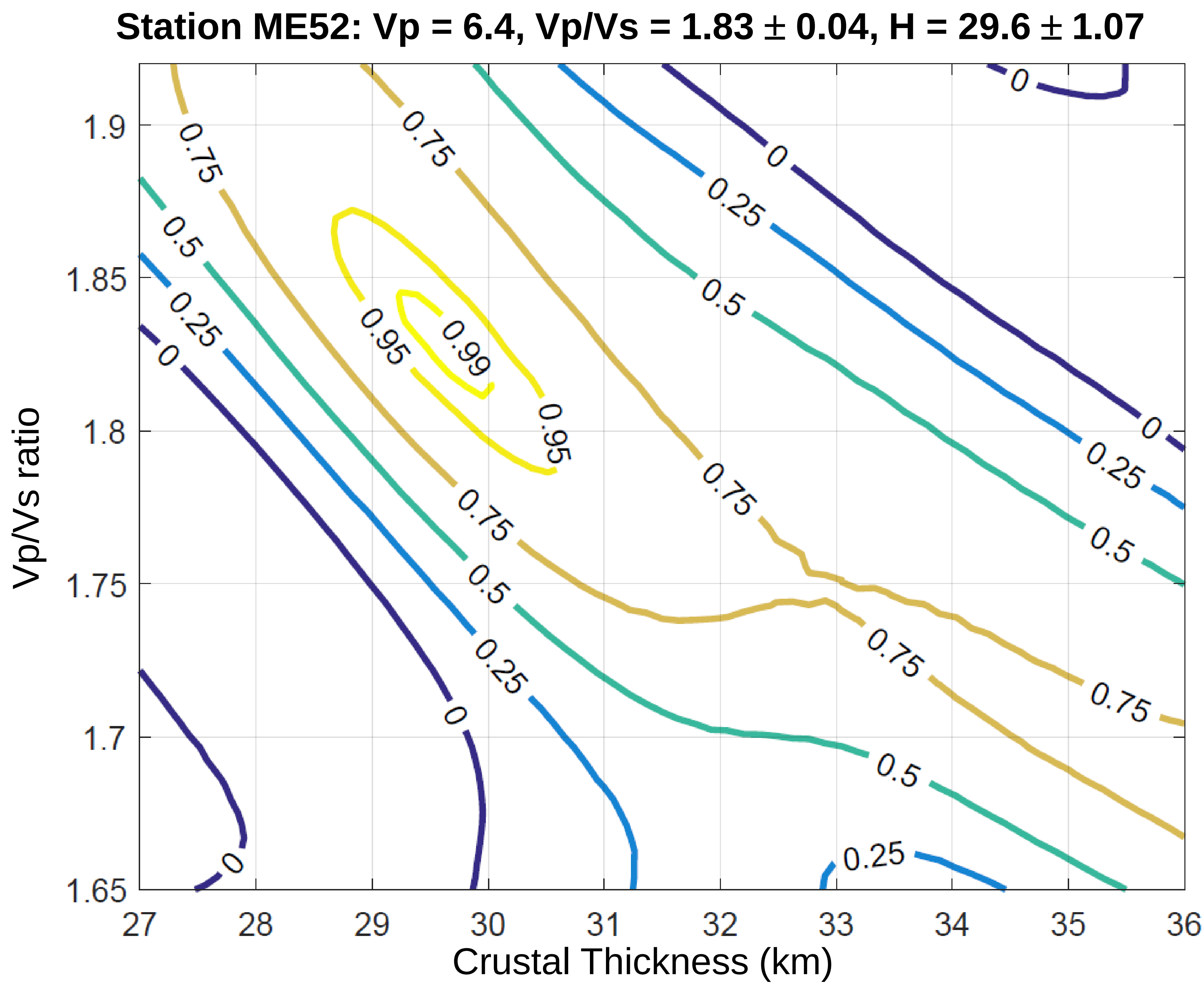
Station ME52: Vp = 6.4, Vp/Vs = 1.83 ± 0.04, H = 29.6 ± 1.07
Vp/Vs ratio
Crustal Thickness (km)
1.65
1.7
1.75
1.8
1.85
1.9
27
28
29
30
31
32
33
34
35
36
0
0.25
0.5
0.75
0.95
0.99

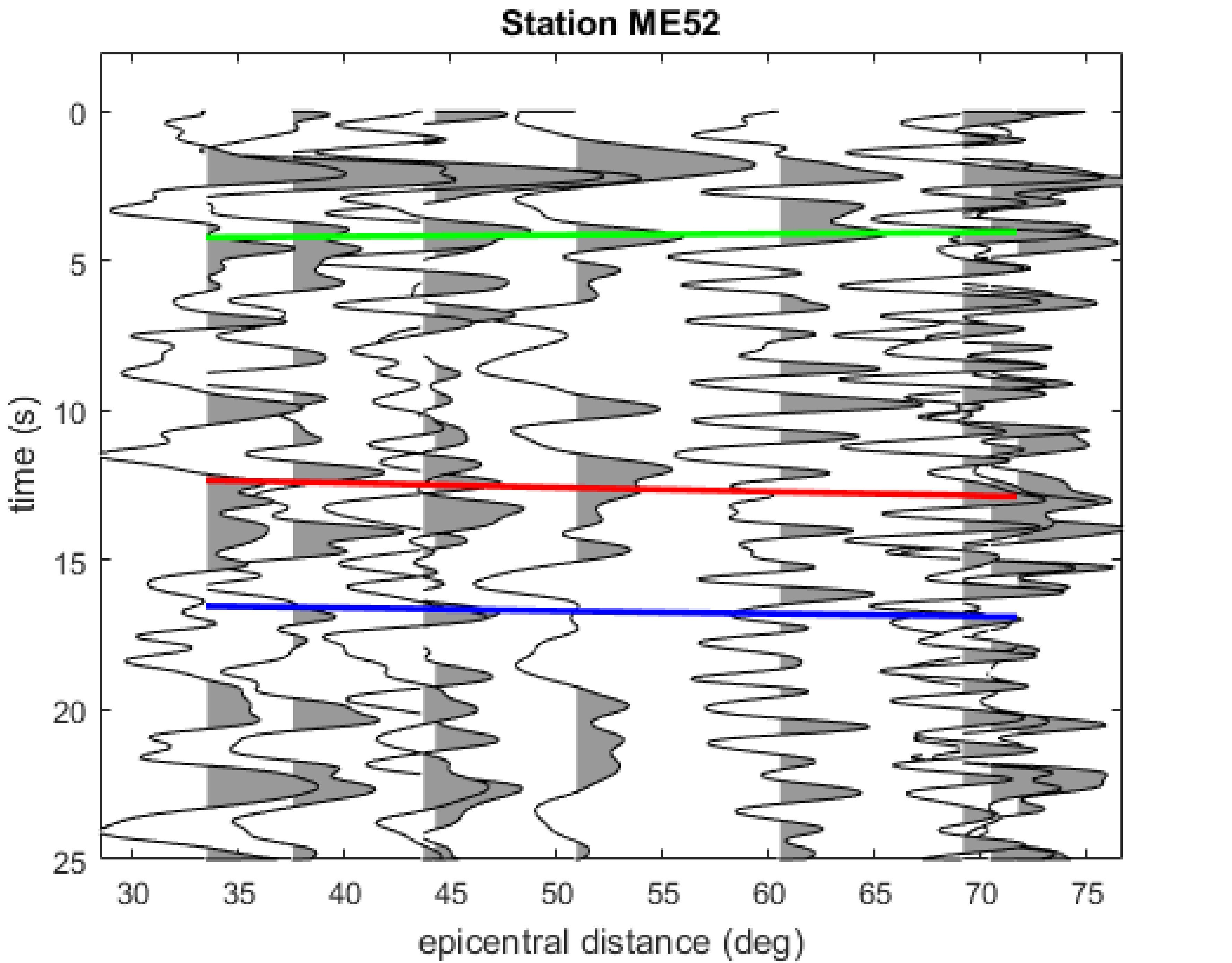

Station ME52
time (s)
0
5
10
15
20
25
30
35
40
45
50
55
60
65
70
75
epicentral distance (deg)

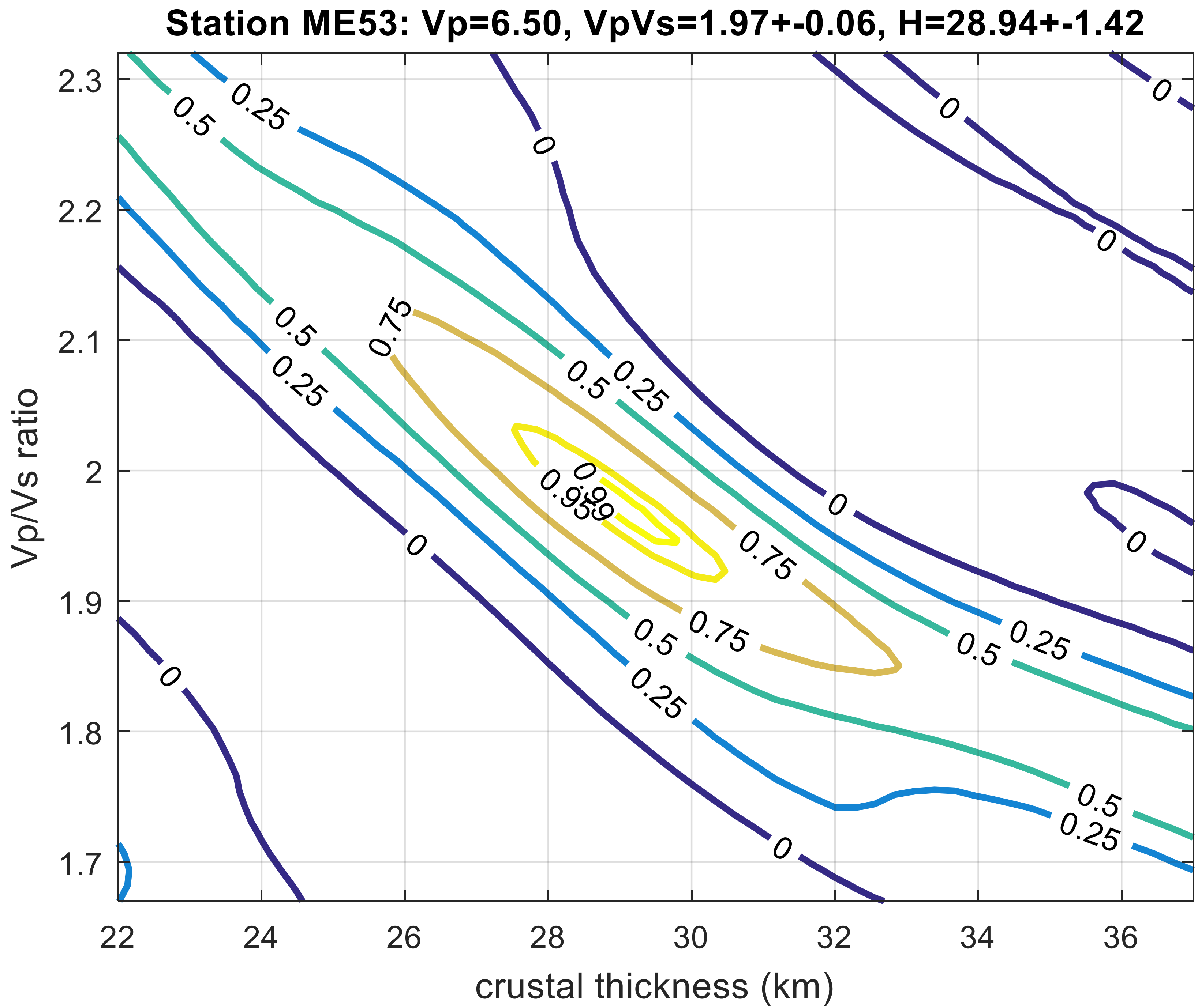

Station ME53: Vp=6.50, VpVs=1.97+-0.06, H=28.94+-1.42
Vp/Vs ratio
crustal thickness (km)
2.3
2.2
2.1
2
1.9
1.8
1.7
22
24
26
28
30
32
34
36
0
0.25
0.5
0.75
0.95
0.99

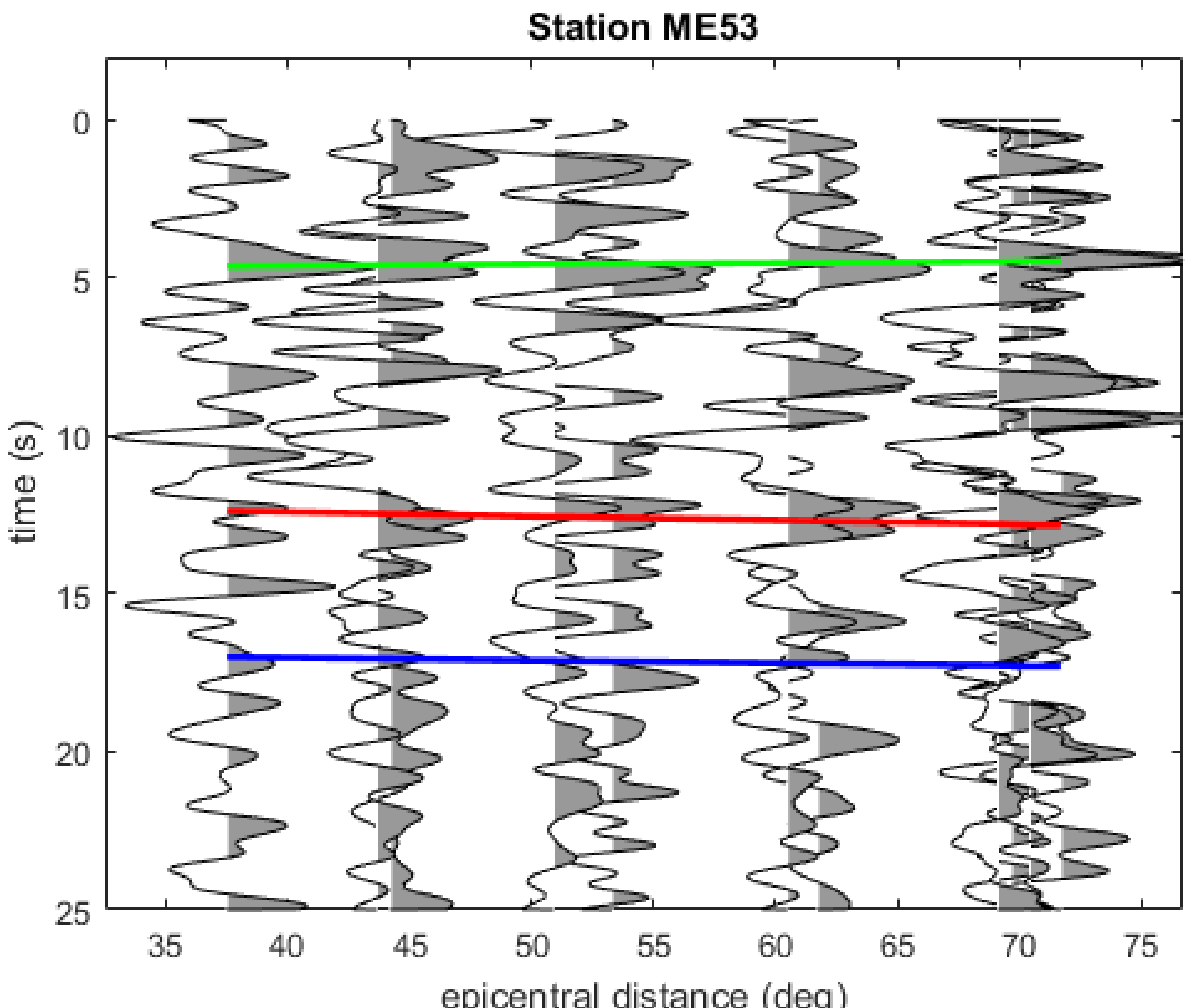

Station ME53
time (s)
0
5
10
15
20
25
35
40
45
50
55
60
65
70
75
epicentral distance (deg)

List of Stations that do not show good H-K method results. Crustal depth is measured by simple stack all RFs in depth domain using velocity input from tomography model (Ramdhan, 2019)

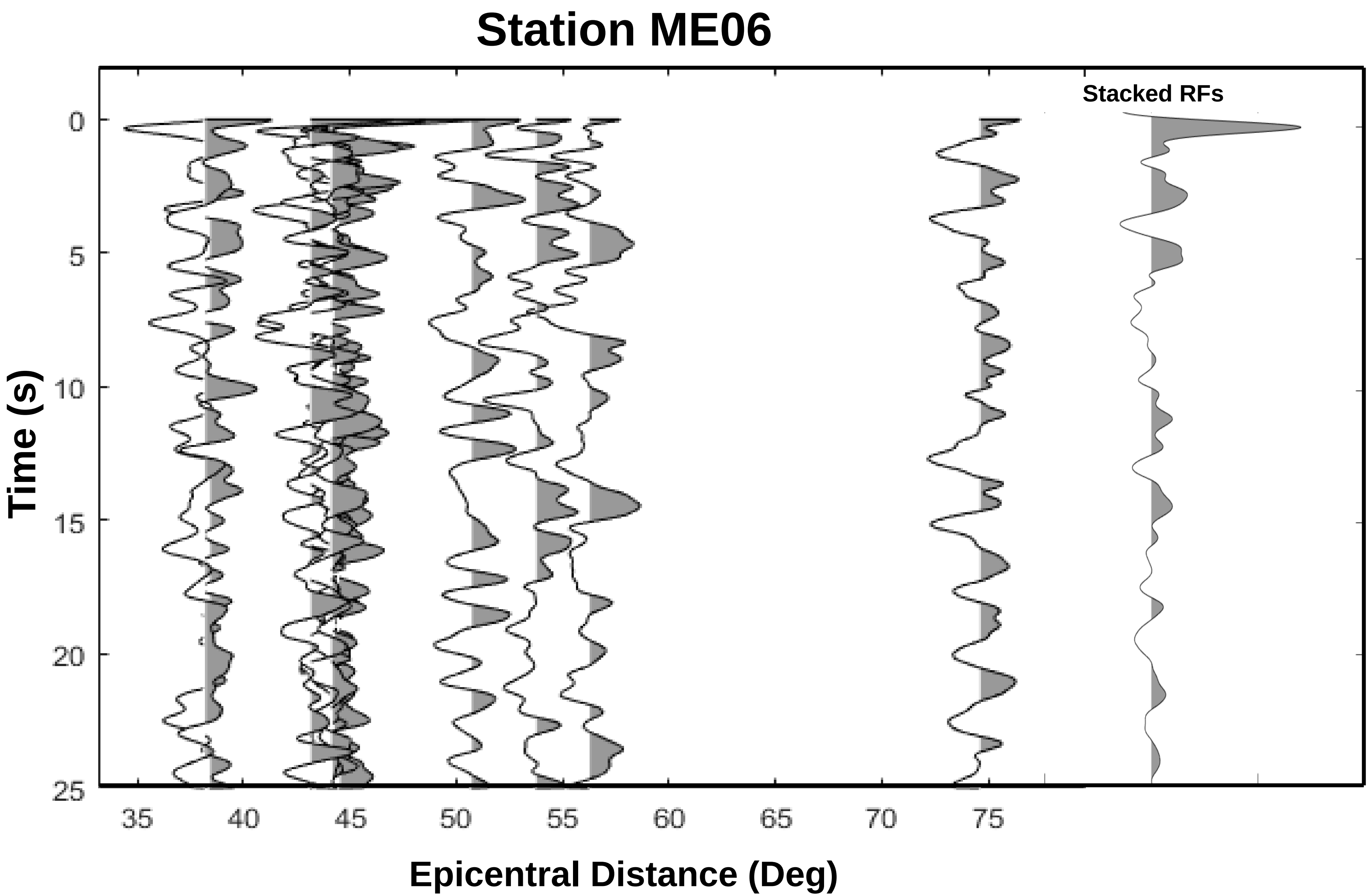
Station ME06
Stacked RFs
Time (s)
0
5
10
15
20
25
35
40
45
50
55
60
65
70
75
Epicentral Distance (Deg)

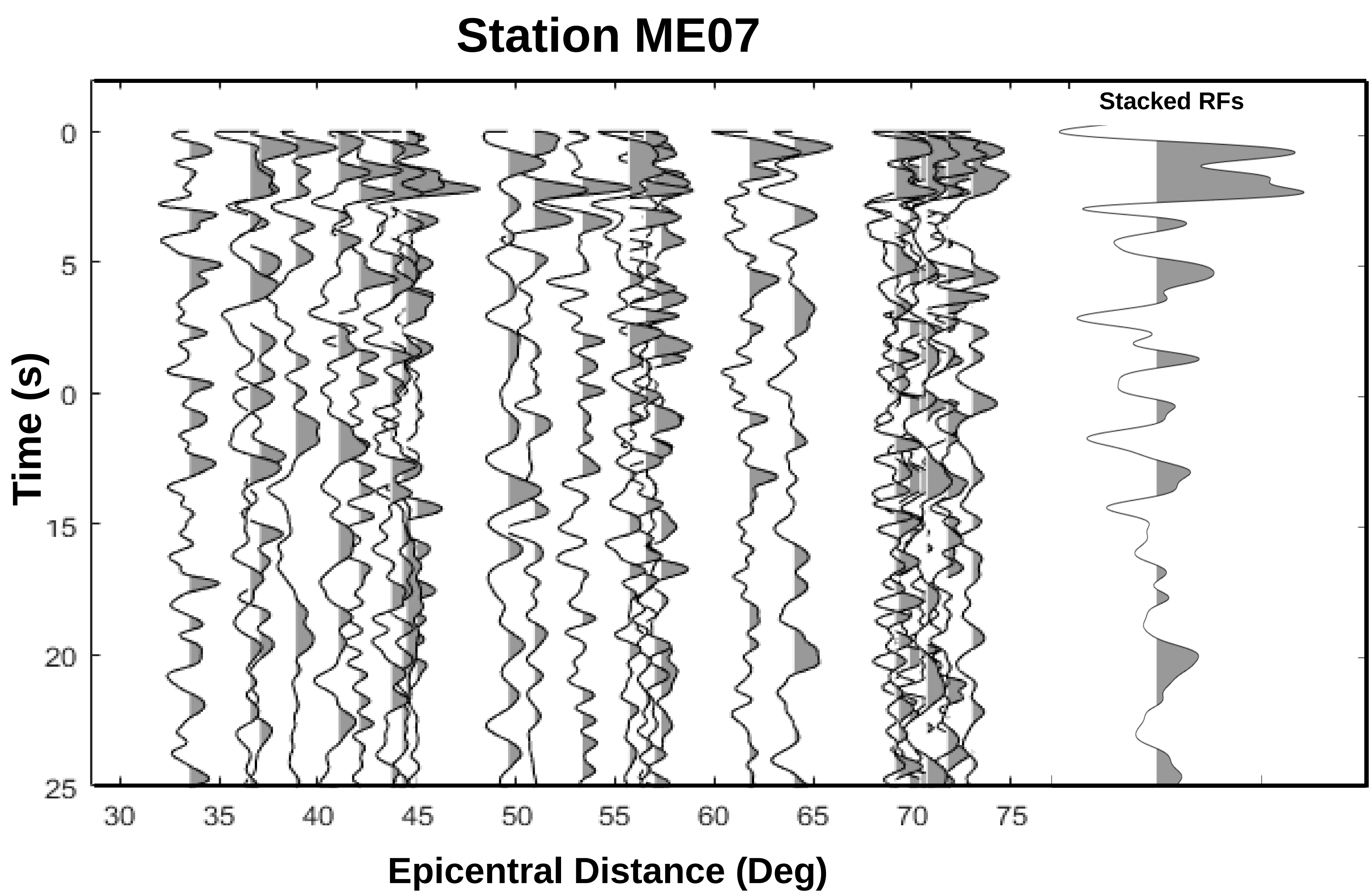
Station ME07
Stacked RFs
Time (s)
0
5
0
15
20
25
30
35
40
45
50
55
60
65
70
75
Epicentral Distance (Deg)

Station ME18

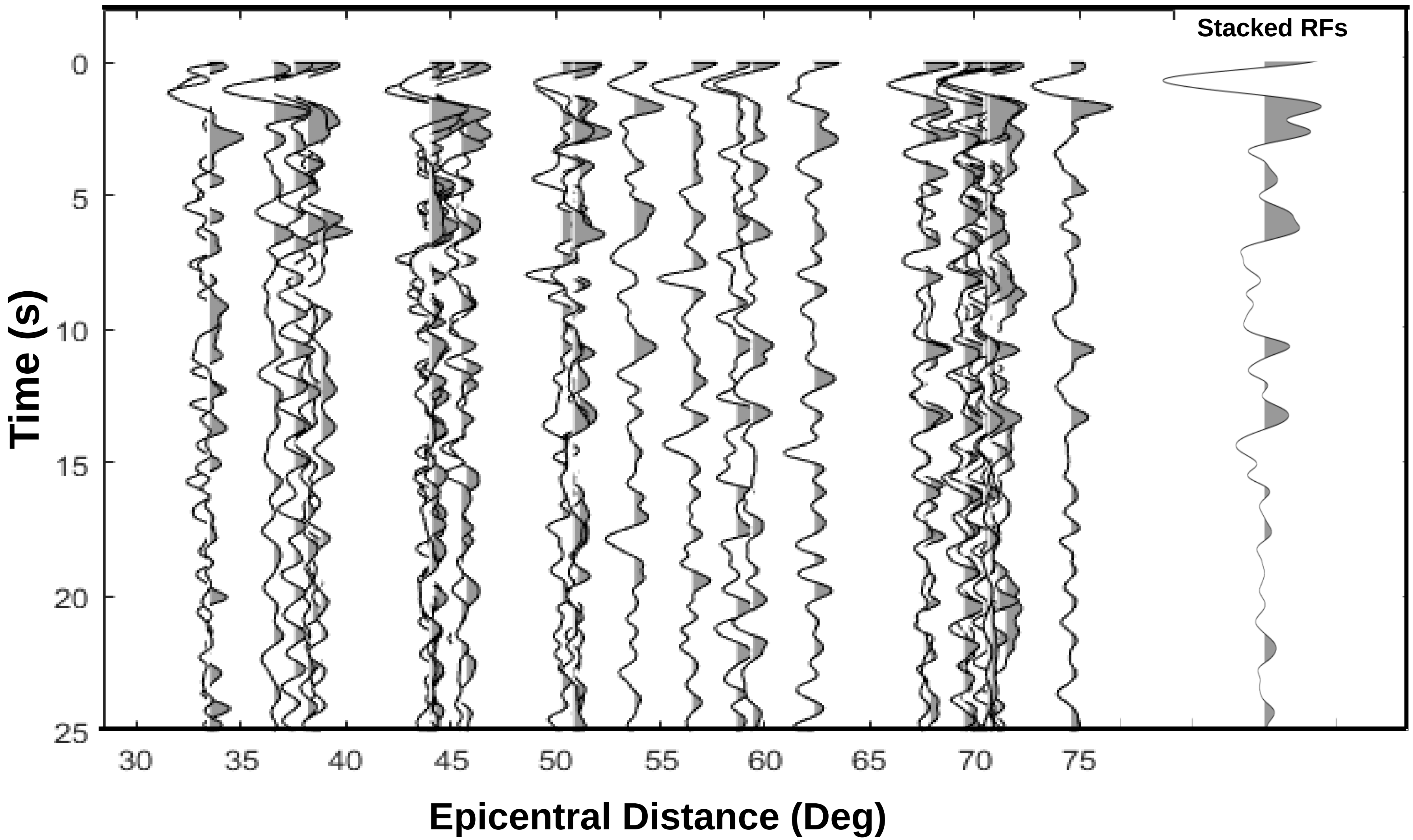

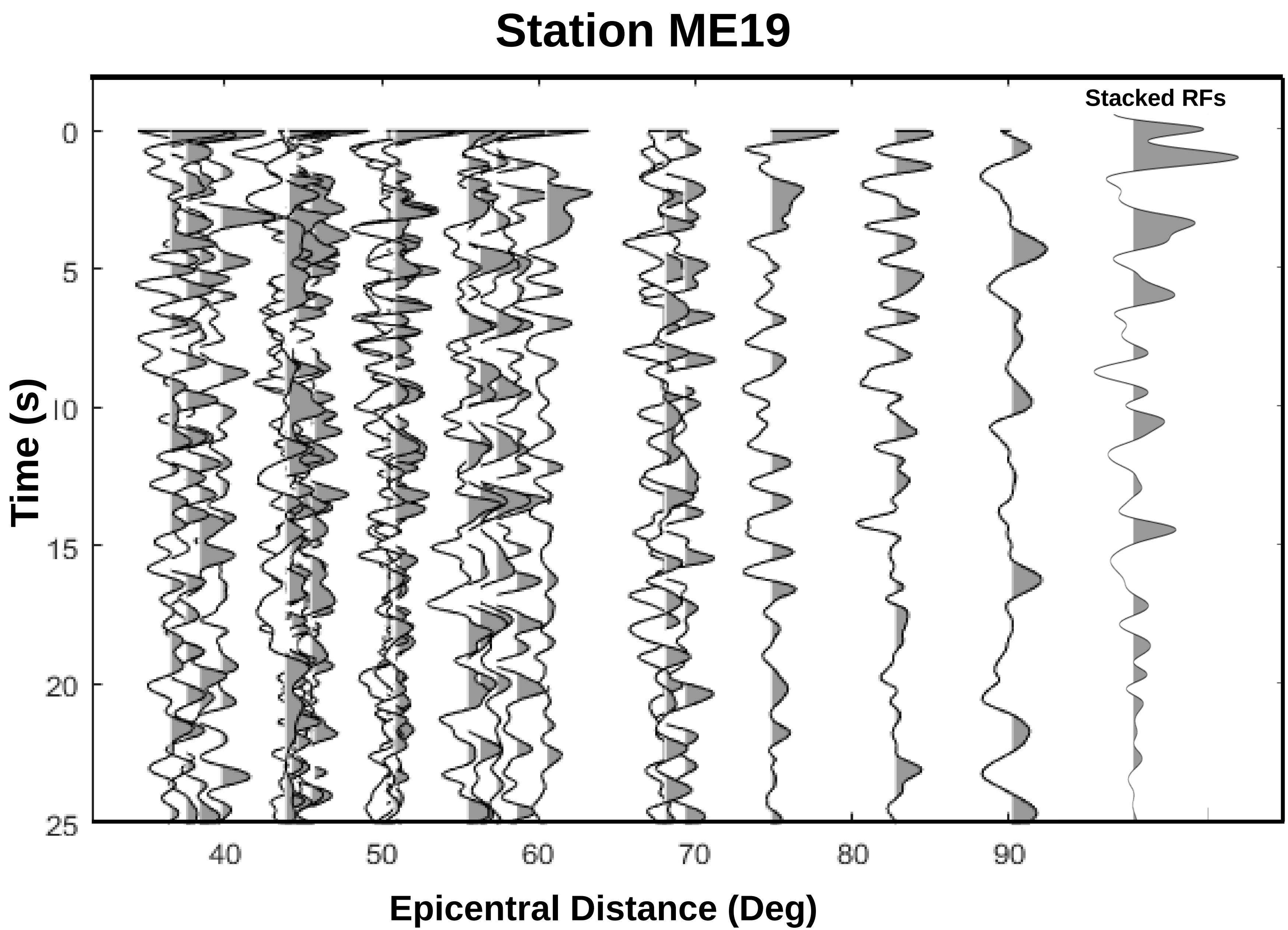
Station ME19
Stacked RFs
Time (s)
0
5
10
15
20
25
40
50
60
70
80
90
Epicentral Distance (Deg)

Station ME30

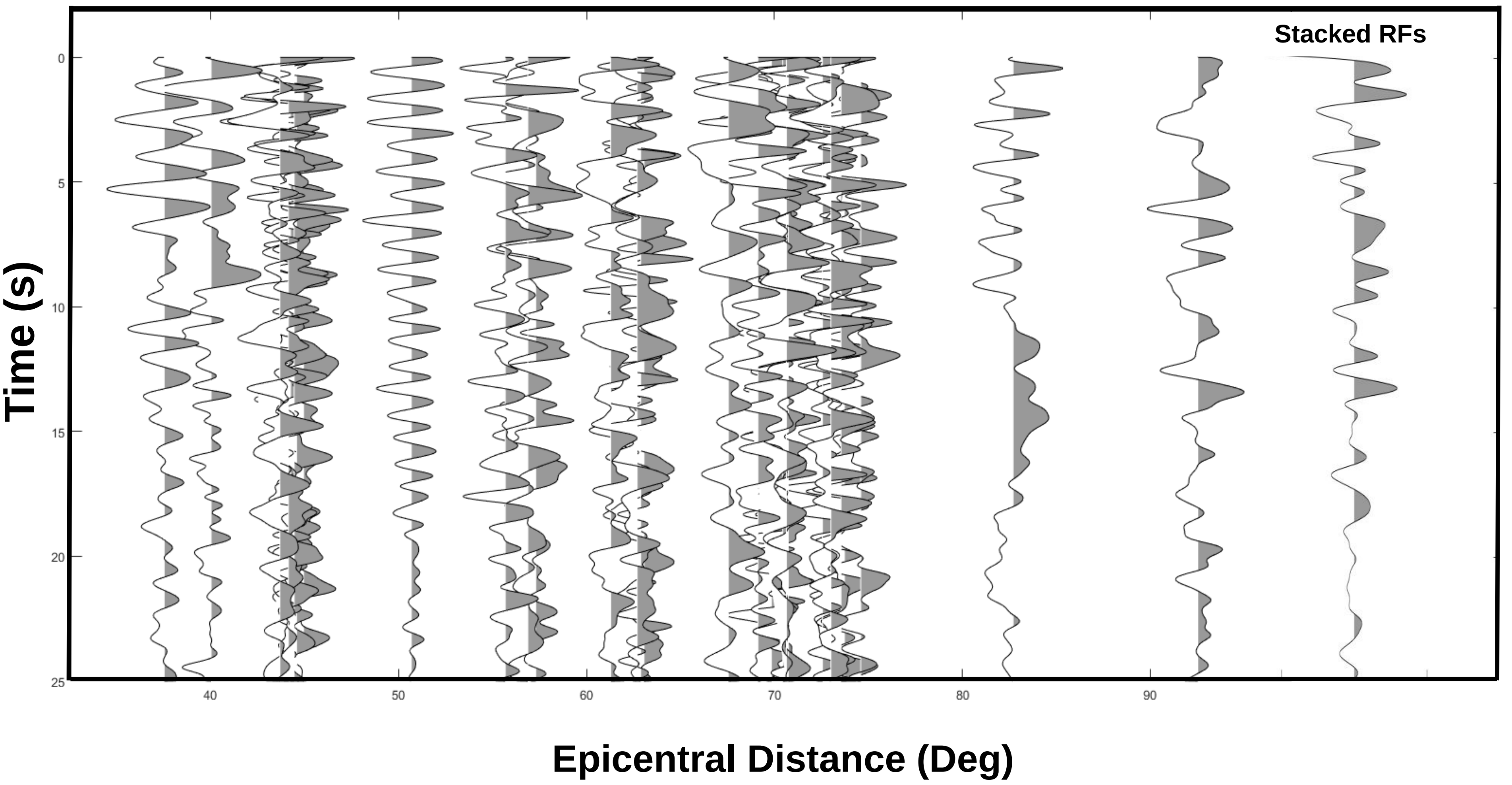

Station ME32

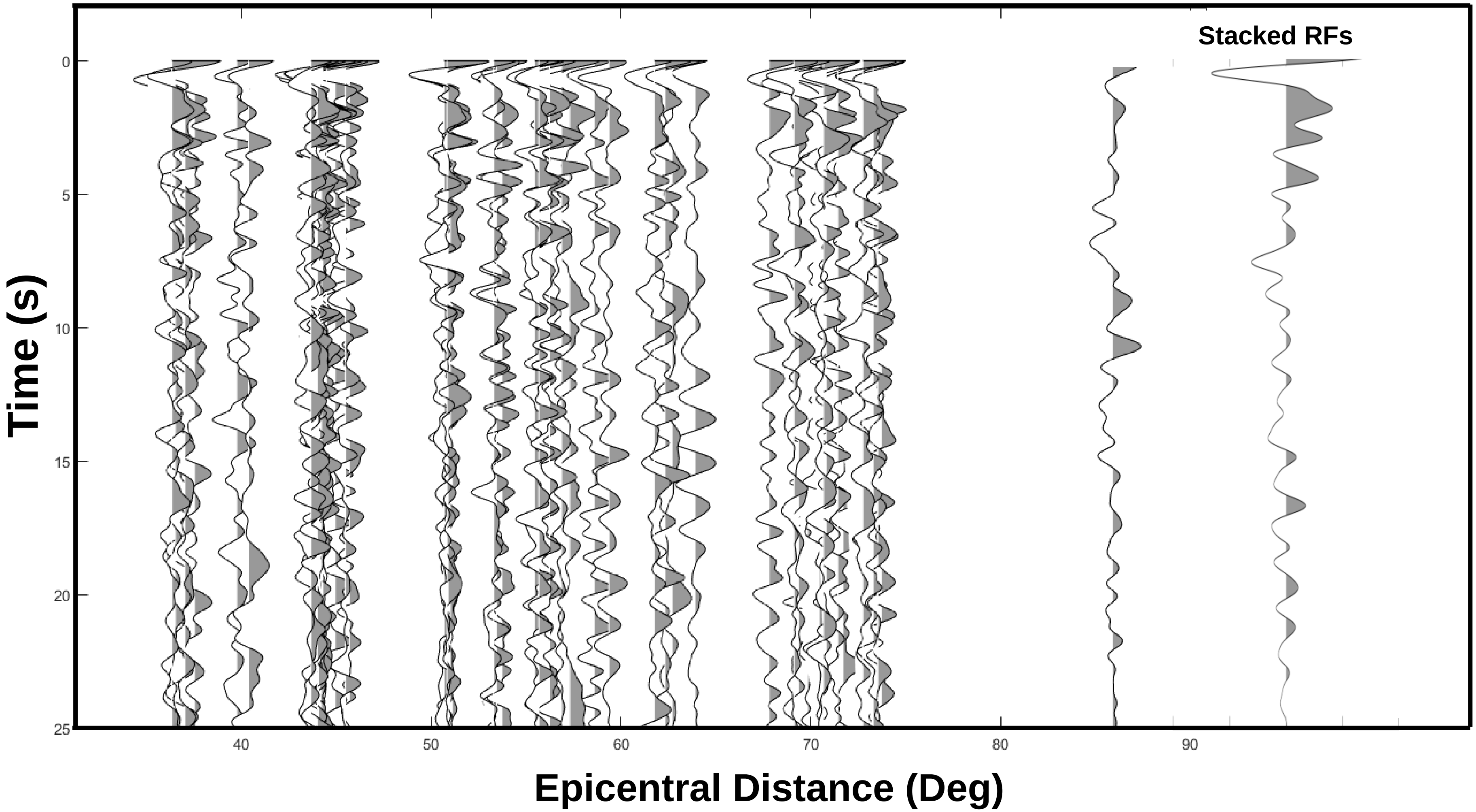

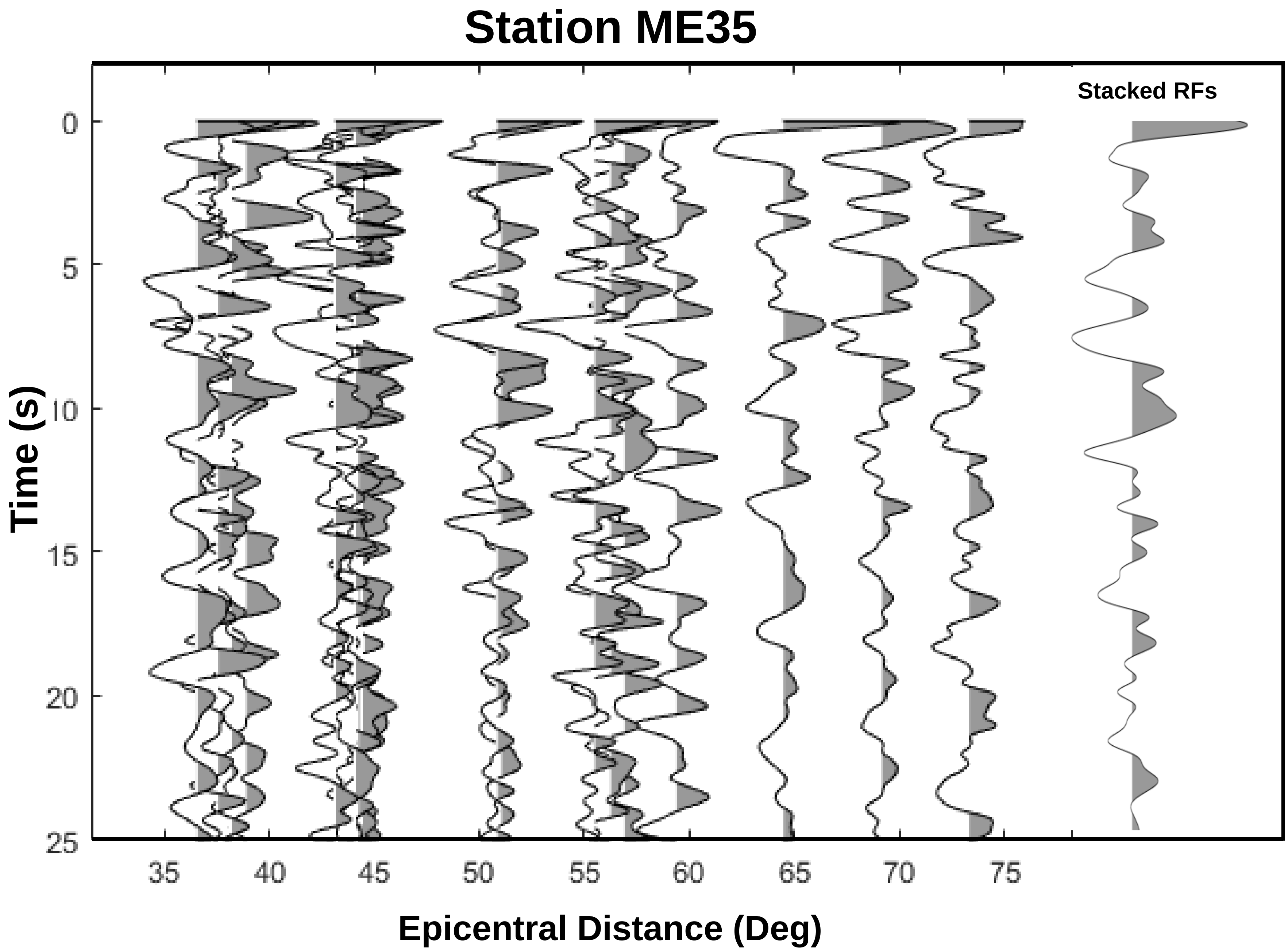
Station ME35
Stacked RFs
Time (s)
0
5
10
15
20
25
35
40
45
50
55
60
65
70
75
Epicentral Distance (Deg)

Station ME45

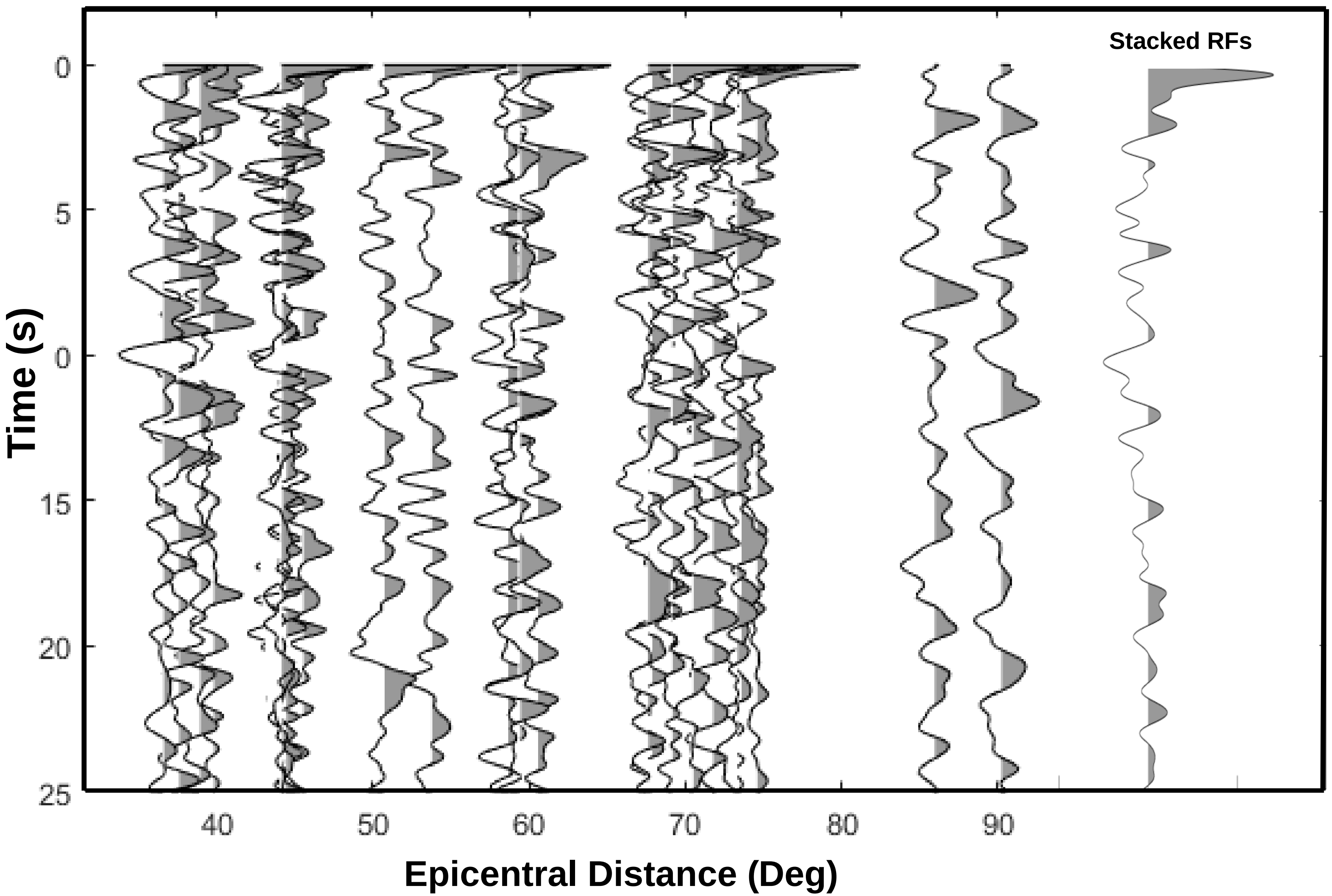

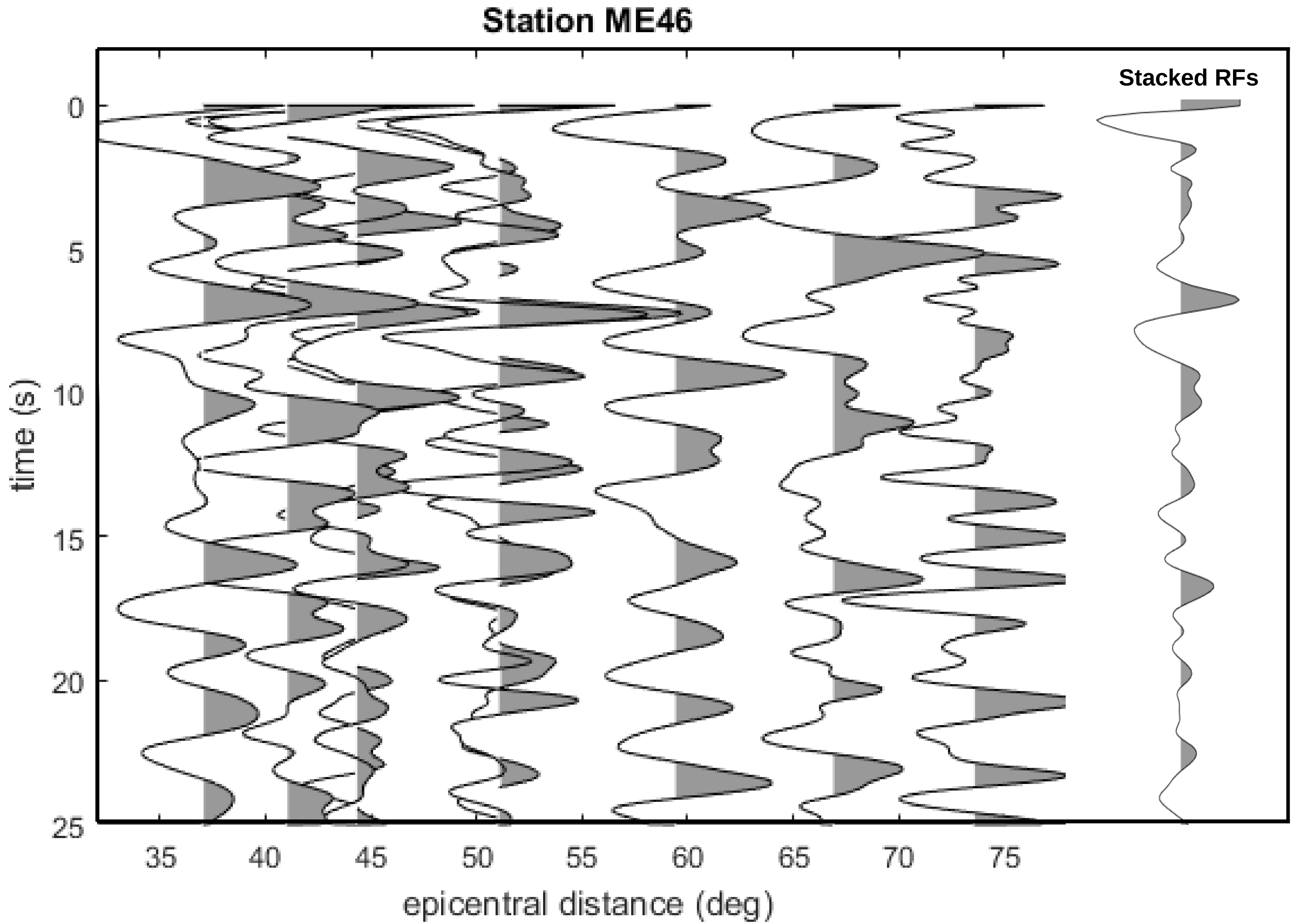

Station ME46
Stacked RFs
time (s)
0
5
10
15
20
25
35
40
45
50
55
60
65
70
75
epicentral distance (deg)